2002

Microstructure-property relationships in laser welded microalloyed steel sheet

Goodwin Phillip Anderson
Lehigh University

Anderson,
Goodwin Phillip

Microstructure-Property Relationships in Laser Welded Microalloyed Steel Sheet

January 2003

Microstructure-Property Relationships in Laser Welded Microalloyed Steel Sheet

by

Goodwin Phillip Anderson

A Thesis

Presented to the Graduate and Research Committee

of Lehigh University

in Candidacy for the Degree of Master of Science

in

Materials Science and Engineering

Lehigh University

July 15, 2002

This thesis is accepted and approved in partial fulfillment of the requirements for the Master of Science.

7-17-02

Date

Thesis Advisor

Chairperson of Department

Acknowledgements

Thanks are certainly in order for my advisor, Dr. Arnold Marder. Our discussions, both technical and personal, have been a valuable component of my learning experience here. I have appreciated the latitude you have allowed me in conducting research over the past two years. Thank you also to the sponsors of this project: U.S. Steel Corporation, Stratcor/U.S Vanadium, and the Pennsylvania Infrastructure Technology Alliance (PITA). Without their support, none of this work would have been possible.

I owe a debt of gratitude to many at Lehigh University. In particular, I would like to thank Arlan Benscoter, whose experience and knowledge in metallography is matched only by his willingness to teach hapless graduate students, and Mike Rex, who at times put in extra hours after a long day at work to machine formability samples for me. Thank you also to Dave Ackland for your patience and teachings in electron microscopy. The support of many of the current graduate students is also greatly appreciated, particularly Aaron Mengel, whose patience, time, and SYSWELD knowledge enabled us to jointly construct the laser welding model. To the materials science graduate students, I will remember with fondness the many late night conversations at Whitaker Lab and afternoons playing hoops, and I will also recall [to a lesser degree] the good times spent at the Ho and the Happy Tap. Special appreciation also goes to three recent graduates of the group—Kevin Luer and Jesse Nawrocki, who showed me the ropes when I first started my Masters program, and especially Steve Banovic, now at NIST, who patiently answered my questions regarding formability and who selflessly took several weeks of

his time to help me conduct formability tests, and his wife Christine, for her hospitality while I stayed at the Banovic household.

From outside the Lehigh community, Steve Jansen of Noble Metals Processing volunteered his time and expertise in making the laser welds for me. His services were invaluable. Also Dr. Tim Foecke of NIST, who helped in transferring the recordings of the formability tests.

I would like to thank all my family and close friends that have provided morale support over the past two years. Mom and Dad, you sometimes seem to be concerned that you cannot help me enough with my work. Trust me when I say that you have already helped me more than you realize through your unending encouragement and guidance. And to my girlfriend Cathi, who has stayed with me through the turns life has taken over the past four and a half years, thank you for the love and kindness you bring to my heart.

Table of Contents

List of Tables

List of Figures

Abstract

In an effort to reduce vehicle weight and improve fuel economy, the automotive industry now manufactures body panels from tailor welded blanks, in which laser welded sheet is subjected to sheet deformation processes. Decreases in the overall formability of the blank have been attributed to poor weld ductility in some instances.

In this study, the base metal and laser weld microstructures of high strength low alloy (HSLA) steels are characterized, and the mechanical properties are assessed. Weld thermal cycles were also calculated by developing a simple computer model. In this manner, general process-microstructure-property relationships were established.

Improved strength levels and decreasing strain hardening capability of the precipitation-strengthened base metals are correlated with increasing microalloy precipitate content, whereas increases in fusion zone strength levels and decreases strain hardening behavior are associated with increasing carbon content. The trends in fusion zone mechanical properties are due to the large (greater than 50 vol%) amounts of martensite that form, even in grades with carbon contents as low as 0.042wt%. High strain hardening values, such as those attained in dual phase (ferrite-martensite) steels, were not achieved in this study. The fusion zones of all grades were stronger and less ductile than their respective base metals.

The possibility of martensite autotempering during the weld thermal cycle was investigated by comparing cooling rates and microhardness data of fusion zone and austenitized and brine-quenched martensite to published results on martensite that was not autotempered. The extent of martensite autotempering depends upon the calculated martensite start temperature. Autotempering did not measurably affect the fusion zone mechanical properties in grades with martensite start temperatures less than approximately 450°C, but grades with slightly higher martensite start temperatures (greater than 465°C) exhibited significant autotempering. The autotempering response was insensitive to the range of cooling conditions explored in this study.

It is suggested that high strength steels with reasonable formability in the laser welded condition may be developed by increasing the microalloy content and reducing the carbon content. In this manner, the fusion zone strength levels and strain hardening values may be tailored to more closely match the properties of the base metal.

1. Introduction

The relationship between microstructure and mechanical properties of welds in microalloyed steels has been a topic of great interest in the welding community. Most of the research to date has been motivated by applications in the pipeline, pressure vessel, shipbuilding, and construction industries, which require arc welds having excellent strength and toughness.

In contrast, relatively little research has been dedicated to microstructure-property relationships in laser welds on thin microalloyed sheets. One major application of these welds lies within the automotive industry, which now routinely forms welded sheet in the manufacture of tailor welded blanks. Numerous studies have been published on the formability of welded blanks[1-4], and it has been concluded that, in some instances, the formability of laser welded blanks is limited by ductility of the weld[1].

Despite this assertion, very little research has been performed that isolates weld properties (such as strain hardening index and ductility) or correlates properties to microstructure in laser welds microalloyed grades. This deficiency in the literature persists because of complications that arise when determining the mechanical properties of small volumes of material, such as laser welds. Many researchers have relied exclusively upon microhardness measurements to describe the mechanical properties of laser welds. The purpose of this study is to isolate weld mechanical properties and

elucidate microstructure-property relationships that exist in laser welds in grades of potential interest to the automotive industry.

2. Background

2.1 Material Selection and Usage

When choosing a material for any application, selection criteria must be identified. Japanese automakers have used the following criteria in the material selection for auto body parts: 1) cost of material and processing; 2) supply stability of the material; 3) functional performance, such as strength, weight saving capability, and corrosion resistance; 4) productivity in mass production, including processes such as forming, welding, and painting; and 5) disposal and recycling after use [5,6]. From these criteria, high strength steels, both hot and cold rolled, have emerged as a leading class of auto body materials.

The current usage of hot rolled and cold rolled steel is summarized in Table 2-1 and Table 2-2, respectively. Hot rolled grades are used for applications with thick geometries, such as structural components, underbody parts, suspensions, and wheel disks. Inner and outer panels, which may be tailor welded, have traditionally been made from cold rolled grades. Until recently, sheet thin enough for body panels could be achieved only through cold rolling. Figure 2-1 and Figure 2-2 show that gages currently used for outer and inner panels is 1.0 mm and 1.4 mm, respectively.

Figure 2-1 and Figure 2-2 also show current and projected strength levels for outer and inner body panels. In the future, Japanese manufacturers anticipate using stronger grades with tensile strengths between 360 MPa and 500 MPa for both outer and inner panels[7].

Increasing strength levels will allow manufacturers to use thinner gage steels, which can result in vehicle weight reduction and concomitant improvement in fuel efficiency.

Material selection in the future will continue to be based upon established criteria, with increasing emphasis on stronger, lighter gage materials. For outer panels, where surface condition is an important functional consideration, cold rolled steels seem likely to remain the material of choice. Inner panels, however, do not have the same surface finish requirement, and might potentially be made from hot rolled steel if there were cost, functional, or processing benefits, according to the selection criteria discussed. The case for hot rolled steels follows.

2.2 Hot Rolled Steels

Thermomechanical treatments, including hot rolling, involve combining controlled amounts of plastic deformation with a heat treatment cycle to improve the mechanical properties of the material while deforming it to the desired shape. The gage of material is reduced to the appropriate thickness, and mechanical properties can be engineered by controlling several strengthening mechanisms, notably grain refinement, precipitation strengthening, and multiphase strengthening.

The continuous hot-rolling process has become the most widely used technique for shaping steel. Molten steel, having been refined by basic oxygen processing (BOP) and perhaps a secondary steel refining process, is cast continuously into slabs 2 to 9 inches

thick and 24 to 60 inches wide. These slabs gradually cool as they are reduced through a series of roughing passes before being finished at a high temperature (greater than the austenite-to-ferrite transformation temperature). After the final pass, the sheet or strip is passed onto a runout table where it is water quenched and coiled. Ferrite transformation occurs on the runout table during the continuous hot rolling process. Although mills have varying geometric limitations on the finished product, typical continuous hot-strip mills cannot produce finished products with a width to thickness ratio exceeding 1000:1 [8].

Hot rolled sheet is not manufactured to as thin a gage as cold rolled products, as seen in Table 2-3 and Table 2-4. The minimum gage limitation of hot rolled sheet is a result of heat flow during the rolling process. The temperature of the material decreases due to convective heat dissipation and conductive heat loss to the rolls. As the gage is reduced with each rolling pass, the effective cooling rate of the sheet increases, making it difficult to keep the roll temperature above the transformation temperature. If the material temperature falls below the critical temperature, the austenite to ferrite transformation begins prematurely, and subsequent rolling passes cause the ferrite to deform and recrystallize. This prematurely recrystallized ferrite has been found to coarsen during coiling, which generally occurs between 650°C and 730°C (1200°F to 1350°F) [8].

Despite the difficulties associated with hot rolling sheet and strip to thin gages, improvements in rolling technology have made it possible to hot roll sheet to thicknesses

suitable for automotive inner panels (i.e., less than about 1.4 mm). Table 2-5 shows the capabilities of some hot rolling facilities that are capable of rolling steel to thin gages.

Technological advances known as thin slab casting and rolling is making thin gage hot rolled steels more common. The term "thin slab casting and rolling" encompasses a number of competing technologies, notably Compact Strip Production Technology (CSP), CONROLL®, Danieli, and Sumitomo. These technologies are all based on processes in which very thin slabs are continuously cast and hot rolled into thin gage finished product. The difference from technology to technology lies in the thickness of the cast slab and the details of the rolling schedule. For example, in CSP, 50 mm thick slabs are continuously cast and direct rolled by a six stand finishing mill, whereas CONROLL®, Danieli, and Sumitomo technologies involve casting a slab between 70 mm and 90 mm thick, roughing that slab over 1 or 2 stands, and finishing with a 5 stand mill[9].

In addition to the processing advantages over traditional rolling operations, thin slab casting and rolling also poses economic advantages. Estimates suggest that hot rolled product manufactured by the thin slab route is $100/ton cheaper than cold rolled coil of the same gage produced by a low cost integrated steel plant [10]; refer to Figure 2-3. It is this financial advantage that may ultimately make hot rolled product (manufactured using a thin slab processing route) preferable to the cold rolled materials in currently in use.

Hot rolled microalloyed grades are of particular interest in this study because of their current use for body panels in the cold-rolled condition.

2.3 Processing, Properties, and Microstructures of HR MA Steels

It has been shown that formability depends upon mechanical properties, both in the base metal and in the weld. Processing routes and microstructures allow for strengthening mechanisms (e.g., grain boundary strengthening, precipitation hardening, and multiphase strengthening) that are responsible for the mechanical properties of microalloyed steels. Relevant mechanisms are discussed here.

2.3.1 Grain Boundary Strengthening

Grain boundaries are thought to strengthen materials via two mechanisms: 1) by providing barriers for dislocation motion, which leads to dislocation pileup near grain boundaries, and 2) acting as sources for dislocations that interact with each other to strengthen the material. It follows that the strength of a material should increase with decreasing grain size. Quantitatively, the grain size-strength relationship observed by Hall and Petch in polycrystalline materials [11,12] has the form

$$\sigma_{ys} = \sigma_i + k_y d^{-\frac{1}{2}} \tag{2-1}$$

where the yield strength, σ_{ys}, is expressed as a function of the lattice strength (Peierls Stress), σ_i, locking parameter, k_y, and grain size, d. This well established equation,

known as the Hall-Petch relationship, was initially observed empirically but has been substantiated on a theoretical basis as well [13,14].

The locking factor, k_y, is of particular importance in understanding the contribution of grain refinement to the overall strength of a material. The locking factor is sensitive to the dominant interstitial alloying element (e.g., carbon or nitrogen), Figure 2-4 [15]. Consequently, k_y is sensitive to small changes in composition and thermomechanical processing, both which affect the amount of carbon and nitrogen in solution[16-19].

2.3.1.1 Grain Refinement

The amount of grain refinement caused by the hot rolling process depends upon the initial grain size of the continuously cast (or soaked) austenite. The finer the initial austenite size is, the finer the final ferrite grain size is. This has been well established by many researchers and can be seen in Figure 2-5. At the elevated soak temperatures (typically ~1300°C for low carbon steels), the steel is almost completely solutionized, with the exception of extremely stable TiN precipitates, which serve to prevent grain coarsening at elevated temperatures by pinning grain boundaries [20]. Regardless, at 1300°C, even the TiN precipitates have coarsened enough to allow grain growth in the austenite to occur, as shown in Figure 2-6.

From the initial austenite grain size, the primary way in which hot rolled precipitation strengthened grades undergo grain refinement is through repeated recrystallization, either

static recrystallization (SRX) or dynamic recrystallization followed by metadynamic recrystallization (DRX+MDRX)). Which mechanism is observed depends upon the temperature, amount of strain accumulation, and composition of the material. Traditional hot rolling practice calls for initial passes to be made at approximately 1250°C, with an initial deformation of 15% or less. New processing routes used in making thin gage hot-rolled sheet and strip call for far larger initial strains, however[10,21]. Both recrystallization paths are possible in the manufacture of these materials, even within a single processing route. Repeated recrystallization is known to refine grains to 5 μm and smaller.

2.3.1.2 Static Recrystallization

SRX refers to the nucleation and growth process of recrystallization that occurs between deformation passes. The driving force for SRX is the elimination of thermodynamically unfavorable dislocations. Therefore, the greater the dislocation density (i.e., the greater the accumulated strain introduced during rolling), the more rapidly SRX occurs. Typical nucleation sites include prior grain boundaries, so it follows that fine grained structures offer a greater nucleus density and therefore faster reaction kinetics. Also, temperature plays a crucial role in SRX, as it does in all nucleation and growth processes. Many researchers have used the controlling variables strain (ε), pre-deformation austenite grain size (D_0), and temperature (T) to describe the kinetics of the SRX process in the form

$$t_x = K\varepsilon^n D_0^2 \exp\left(\frac{-Q}{RT}\right) \qquad (2\text{-}2)$$

which expresses the time required for x percent SRX, where K is a composition-dependent constant, n varies from –2.5 to –4, depending on the grade, and Q is the activation energy for SRX, determined by different researchers to have a value between 230,000, and 330,000 [22-25]. From this equation, the Avrami equation expressing recrystallized austenite fraction, X, as a function of time has been determined[22]:

$$X = 1 - \exp\left[-0.0513\left(\frac{t}{t_{0.05}}\right)\right] \tag{2-3}$$

The Avrami function gives rise to characteristically sigmoidal curves such as the ones shown in Figure 2-7, which graphically show the effect of temperature upon recrystallization kinetics. From the Avrami equation and graph, it follows that there is a temperature, T_{nr}, below which no SRX will occur for a material of given composition, initial austenitic grain size, and processing schedule where the interpass time for SRX is limited.

Microalloying elements in solution, particularly Nb, have a retarding effect on SRX, as seen by their effect on the recrystallization stop temperature, Figure 2-8. The extent to which these solutes delays recrystallization has been linked to differences in diffusion coefficients of Ti, Nb, and V solutes in austenite[26]. Of course, if precipitation occurs during finishing, i.e., of Nb(C,N), then SRX is arrested, leading to the pancaking of austenite grains and subsequently to a grain structure generally associated with Nb-bearing hot rolled steels[27]. Processing differences between vanadium and niobium microalloyed steels are detailed in section 2.3.2.2.

2.3.1.3 Dynamic and Metadynamic Recrystallization

The dynamic recrystallization/metadynamic recrystallization sequence (DRX+MDRX) is another possible mechanism that refines grain size. DRX refers to the recrystallization process that occurs instantaneously during deformation. According to some researchers, DRX is followed by MDRX, which is defined as the post DRX growth (*not* nucleation) that can still be described with Avrami-type kinetics[28]. Just as in SRX, the DRX and MDRX occur to eliminate thermodynamically unfavorable strained grains with a strain-free microstructure. Factors controlling the onset of DRX are strain, strain rate, prior austenite grain size, temperature, and composition. Researchers have attempted to model the critical strain, ε_c, required for DRX, and though their models have differed slightly, the general form of the ε_c equation is

$$\varepsilon_c = A d_0^n \left[\dot{\varepsilon} \exp\left(\frac{Q}{RT} \right) \right]^p \tag{2-4}$$

where the critical strain (accumulated strain plus strain of deformation) required for DRX is expressed in terms of A, a constant; d_0, prior austenite grain size; n, a constant between 0.5 and 0.9; $\dot{\varepsilon}$, strain rate, Q, the composition-dependent activation energy for dynamic recrystallization, T, absolute temperature, and p, a constant [29,30]. At high temperatures, SRX tends to occur completely, resulting in little strain accumulation in the steel, thereby making it unlikely that the strain from the deformation pass will exceed the critical strain required for DRX. However, as heat is lost during the rolling process, SRX may not go to completion (or occur at all) within the interpass time, thereby allowing strain to

accumulate. If the sum of the accumulated strain from previous passes and the applied strain of the current pass exceeds the critical strain, the DRX+MDRX sequence begins. Also, although DRX is hindered by the onset of microalloy precipitation in the austenite regime (i.e., Nb(C,N)), DRX is not completely arrested as SRX is[31]. Therefore, DRX and MDRX are most likely to occur fairly late in the rolling process.

2.3.2 Precipitation Hardening

Precipitation hardening (or precipitation strengthening) occurs because precipitates present a barrier to dislocation motion. Depending upon the nature of the precipitate-matrix interface and the precipitation separation distance, dislocations may either propagate or loop around precipitates[32]. Regardless of which occurs, precipitates serve to impede dislocation motion.

The Orowan-Ashby model is one well-known model of precipitation hardening. According to the model, the contribution from the precipitation mechanism depends primarily upon precipitate size and volume fraction, and not the precipitate composition or precipitate-matrix interface, provided they do not deform significantly[33,34]. Several researchers have modified the model to better fit experimental data[35], but the relationship still fits the form

$$\sigma_{ppt} = \frac{0.3Gbf^{\frac{1}{2}}}{\bar{x}} \ln\left(\frac{\bar{x}}{2b}\right) \tag{2-5}$$

where the precipitation strengthening contribution, σ_{ppt}, is expressed as a function of the modulus of rigidity, G, the magnitude of the Burger's vector, b, the volume fraction of the precipitated phase, f, and the average precipitate size, $\bar{x}$. For ferritic steels, it has been shown [36] that this expression is equivalent to

$$\sigma_{ppt} = \left(\frac{8.9 f^{\frac{1}{2}}}{\bar{x}} \right) \ln\left(1630 \bar{x} \right) \qquad (2\text{-}6)$$

The Orowan-Ashby model (and related models) shows that the precipitation strengthening component increases as volume fraction of the precipitated phase increases and precipitate radius decreases. Graphically, this concept can be seen Figure 2-9. Experimental verification of this model has been performed for various titanium, niobium, and vanadium grades [36] with rough agreement, as shown in Figure 2-10.

2.3.2.1 Precipitation Thermodynamics

The most commonly used and most effective microalloying elements (titanium, niobium, and vanadium) form nitrides and carbides as governed by the thermodynamics shown in Figure 2-11. From this graph, several comments are made:

1. For each alloying element shown, the nitride is less soluble (i.e., more likely to form a stable nitride) then its carbide counterpart. In the extreme, TiN is stable in austenite even at high temperatures, approximately four orders of magnitude less soluble than TiC. Similarly, VN is approximately two orders of magnitude less

soluble than VC in austenite. The solubilities of NbN and NbC in austenite are more similar.

2. At the austenite to ferrite transformation temperature, the solubility of all microalloy precipitates decrease. However, the decrease in VC and NbN solubility are the most pronounced.
3. Although not shown in Figure 2-11, Al also forms a stable nitride, which is more stable than NbN but less stable than TiN. AlC are not thermodynamically favorable and have not been observed in microalloyed steels[37].

Additional background information regarding the common microalloy additions are explained by element:

Titanium: Titanium has such a low solubility in austenite that extremely stable TiN particles form even with low nitrogen and titanium contents. These particles play an important role in the refinement of austenite grain size, as is discussed later. TiC may also form, but thermodynamics dictate that TiN precipitation is far preferable; therefore, very little carbon is contained in Ti(C,N) precipitates unless there is an excess of Ti beyond the 4:1 stoichiometric ration of titanium to nitrogen.

Aluminum: As mentioned, Al forms a distinct nitride with a stoichiometry of approximately 2:1 (Al:N), which is relatively stable in the austenite regime. Al is unique among microalloying elements because it does *not* form carbides under normal

processing conditions. However, AlN precipitates are not always observed because the hexagonal structure of AlN gives rise to sluggish precipitation kinetics.

Niobium: Because of the comparable solubilities of NbC and NbN, separate nitrides and carbides rarely form. Rather, niobium forms complex carbonitrides, Nb(C,N), which tend towards a stoichiometry of 8:1 (Nb:(C,N))[25]. The thermodynamics of Nb(C,N) formation are such that strain-induced precipitation is commonly observed at temperatures below 1000°C[37], which serves to retard recrystallization. It is also well established that niobium in solution also retards recrystallization. The effects of niobium content on recrystallization are mentioned later.

Vanadium: As the most soluble of the microalloying elements, vanadium tends to form carbonitrides of 4:1 V:(C,N) stoichiometry at low temperatures, within the lower austenite or ferrite regime. This potentially causes grain refinement through the nucleation of ferrite grains on V(C,N) and gives rise to a fine dispersion of precipitates[25].

2.3.2.2 Processing of Precipitation Strengthened Grades

The metallurgical response of microalloyed steels depends on the processing parameters such as reheating temperature, rolling schedule (e.g., rolling temperature, strain per rolling pass, strain rate, and interpass time) and cooling rate.

Traditionally, cast ingots of microalloyed steel were reheated to a soak temperature, either from room temperature (termed cold charging) or from some elevated temperature (called hot charging) before hot rolling thermomechanical treatment. With the advent of continuous casting and compact strip production (CSP), though, there is not a "reheating temperature" per se. Here reheating temperature can be thought of as the temperature of the material immediately prior to thermomechanical processing.

Typical reheating temperatures for microalloyed steels range from 1150°C to 1350°C; lower preheat temperatures may not solutionize the microalloy precipitates such as Al, Nb, and V [carbo]nitrides, thereby adversely altering the precipitation and recrystallization behavior of the alloy. At the reheating temperature, the austenite grains have ample time and thermodynamic driving force to coarsen, sometimes to grain sizes as large as 0.3mm to 1.0 mm[37], depending upon the geometry of the stock and whether it was cold or hot charged. The initial condition of the alloy before hot rolling is coarse-grained austenite. Many researchers have shown a correlation between coarse initial austenite grain sizes and coarse as-rolled ferrite grain sizes, Figure 2-5. For maximum ferrite grain size refinement, the initial austenite size should be as small as possible.

Researchers have long recognized that stable particles retard grain growth through the Zener drag effect, in which precipitates effectively pin grain boundaries. The grain boundary motion is inhibited because the precipitate has limited mobility, and movement of the grain boundary away from the precipitate leads to increased surface area, which is

energetically unfavorable. In microalloyed steels, the highly stable TiN precipitates serve to pin austenite grain boundaries and slow grain growth, Figure 2-6 illustrates the coarsening behavior of a microalloyed steel with TiN precipitates. At temperatures below 1100°C, the TiN precipitates allowed for negligible coarsening; at temperatures between 1100°C and 1300°C, coarsening of the austenite grains was apparent. At the higher reheating temperatures, more of the TiN went into solution, decreasing the volume fraction of the inhibiting precipitate. Also, the remaining TiN precipitates began to coarsen, limiting their effectiveness retarding grain growth. Still, TiN is largely effective in decreasing the initial austenite grain size.

The controlled rolling (CR) process is shown schematically in Figure 2-12. Microalloyed grades with high recrystallization stop temperatures (i.e., Nb bearing grades) may be processed this way, although other grades may be CR as well. In CR, the initially coarse austenite grains may be refined by recrystallization (as in recrystallization controlled rolling, detailed below). However, the material is finished below the recrystallization stop temperature, which gives rise to the pancaked structure shown in the schematic. Clearly, the microstructure is no longer refined by recrystallization. Instead, the grains are refined during the austenite to ferrite transformation. The pancaked grains have a greater surface area per volume than equiaxed grains, thereby providing more nucleation sites and enhanced refinement during transformation. This effect is illustrated in Figure 2-13. The result of the CR process is a fine-grained equiaxed ferritic microstructure.

Recrystallization controlled rolling, RCR, is another common thermomechanical process in hot rolling microalloyed grades. Alloys with a low recrystallization stop temperature (e.g., Ti, V, and Ti-V grades) are frequently RCR. Schematically, the RCR process appears in Figure 2-14. The initial austenite grain size is coarse; refinement occurs through repeated static and dynamic recrystallization processes. Because there is no Nb(C,N) precipitation, and V and Ti have minor effects on the recrystallization stop temperature (RST), recrystallization occurs even after finishing. The accelerated cooling (ACC) further refines the microstructure upon transformation to ferrite, and V(C,N) precipitation follows, which yields finely dispersed carbonitrides at the appropriate cooling rate.

Regardless of rolling schedule (RCR or CR), the sheet is finished within the austenite temperature range and cooled to a coiling temperature (within the ferrite temperature range). The rate at which the steel is cooled, as well as the temperature to which it is cooled, affects the microstructure. Often rolled product is cooled rapidly via water sprays, which allows for additional refinement of the ferrite grain size (Figure 2-15) as well as a finer dispersion of precipitates—mostly V(C,N). Because the austenite to ferrite transformation occurs upon cooling, care must be taken not to quench the rolled product too quickly, lest the austenite transform to bainite or martensite. Generally, cooling rates should not exceed 12°C/s, and the final coiling temperature (FCT) should not be below 500°C[37].

2.3.3 Multiphase Strengthening

Multiphase steels have been studied to a great extent over the past 25 years because of their remarkable combination of high strength and ductility. Other noteworthy mechanical properties of multiphase steels include low yield ratio (yield strength/tensile strength), high initial strain-hardening exponent, and continuous yielding characteristic. The mechanisms described here occur in laser welds of most microalloyed steels, as well as in multiphase grades.

Microstructurally, multiphase steels ideally consist of islands of martensite in a ferrite matrix. Other microconstituents such as retained austenite and bainite are also common. Attention has been given to transformation induced plasticity (TRIP) grades, a category of multiphase steels that are identified by the transformation of retained austenite to martensite upon deformation. This phenomenon lends TRIP grades enhanced elongation and additional toughness in addition to the other qualities associated with multiphase steels[38].

Many attempts have been made to understand the deformation behavior and structure-property relationships of steels strengthened through multiphase strengthening. The classic law of mixture with the assumption of either isostrain or isostress was considered [39,40], and other investigators used variations of this model to study the role of retained austenite [41,42] and the deformed state of martensite [43].

2.3.3.1 Mechanical Properties of Martensite

Before discussing the contributions multiphase strengthening makes to mechanical properties, the mechanisms that control the mechanical properties of martensite itself should be mentioned. Martensite is far stronger than the surrounding ferrite matrix, being strengthened by a host of strengthening mechanisms, including solid solution strengthening, boundary hardening (analogous to martensite grain size), and strain hardening. Bearing these dominant mechanisms in mind, Norstrom proposed an equation describing the yield strength of lath martensite in terms of its frictional (Peierls) Stress, solid solution strengthening, boundary hardening, and strain hardening components[44]:

$$\sigma_{ys} = \sigma_i + \sigma_{sss} + \sigma_{bh} + \sigma_{sh} \tag{2-7}$$

This expression is equivalent to

$$\sigma_{ys} = \sigma_i + k\sqrt{c} + k_y d^{-\frac{1}{2}} + \alpha G b\sqrt{\rho} \tag{2-8}$$

which quantifies the yield strength as a function of σ_i, Peierls stress; c, solute (carbon) content; d, martensite packet size; G, Modulus of Rigidity; b, Burgers vector; and ρ, dislocation density, (>10^{10} dislocations/cm^2 in martensite). From this expression, it is clear that "multiphase strengthening" is not really a single mechanism, but rather a combination of many mechanisms.

2.3.3.2 Effect of Martensite in Multiphase Grades

As in precipitation hardening, the volume fraction, size, and distribution of the martensite phase affects the role multiphase strengthening plays in determining mechanical properties. Martensite packet size is analogous to grain size, and therefore is discussed in the following section.

The increase in strength level associated with high volume fractions of martensite has been frequently reported[45,45,46] and is conceptually obvious given the law of mixtures. A less intuitive effect is the decrease in yield ratio (yield strength/tensile strength) associated with increases in martensite volume fraction, Figure 2-16. Similarly, the strain-hardening coefficient increases with increases in martensite volume fraction, Figure 2-17. This trend is intimately interrelated with grain size and is explained as follows. Previous discussion concerning grain size effects were directed towards single-phase systems, such as seen in polygonal ferrite microstructures. Research has also been performed on dual phase (ferritic/martensitic) grades to determine the effect of grain size on mechanical properties[47-49]. More recently, Jiang has proposed and verified a modified version of the Hall-Petch relationship viable for dual phase steels[45,50]:

$$\sigma = \sigma_0^1(\varepsilon, f_m, d_m) + K^1(\varepsilon, f_m, d_m) d_f^{-\frac{1}{2}} \qquad (2\text{-}9)$$

This relationship parallels the original work of Hall and Petch, but the friction stress and the locking parameter were shown to be functions of strain, martensite volume fraction, and martensite packet size, as shown. For the Hall-Petch equation applicable for

multiphase steels, there is a difference in the yield strength and the tensile strength dependence on ferrite grain size; yield strength increases more relative to tensile strength with decreasing grain size, Figure 2-16. As ferrite grain size becomes infinitely large, a negligible strength contribution is expected. Therefore the yield ratio, YS/TS, depends only upon the frictional term expressed in the Hall-Petch relationship. The yield strength friction term is insensitive to changes in martensite content, because dual phase materials often yield plastically while the martensite is elongated only elastically. To a point, the tensile strength friction term increases substantially with martensite fraction, because martensite generally undergoes plastic deformation before the bulk material undergoes necking. This explains why coarse-grained dual phase steels have such low yield ratios. In fine-grained steels, grain size effects mask the sensitivity of tensile strength to martensite volume fraction. More detailed discussion of the yield behavior of dual phase steels is discussed elsewhere[51].

The strain-hardening exponent, n, of multiphase steels also varies with ferrite grain size. At low strains, the strain-hardening exponent decreases as grain size increases due to variations in dislocation densities between ferrite-ferrite grain boundaries and ferrite-martensite grain boundaries. This mechanism is diminished at high strains, causing the strain-hardening exponent to become independent of grain size. The details of this mechanism have been explained by Jiang et al[50]. Graphically, the effects of grain size on strain-hardening exponent are illustrated in Figure 2-17.

The morphology of the multiphase grade affects mechanical properties as well. Reported microstructures for include equiaxed martensite-ferrite, fibrous, fine needlelike martensite phases distributed in ferrite, and ferrite grains surround by coarse martensite grains. By ranking the strength and ductility yielded by each microstructure, beneficial microstructural characteristics can be determined. Strength levels decreased in the following order: equiaxed martensite-ferrite, fibrous martensite distributed in ferrite, and coarse martensite. Ductility decreased in order of fibrous martensite distributed in ferrite, equiaxed martensite-ferrite, and coarse martensite. The best combination of mechanical properties was yielded by the fibrous martensite distributed in ferrite[52].

2.4 Welding of Tailor Welded Blanks

In assessing the formability of welded blanks, the effects of the weld thermal cycle on the microstructures and mechanical properties must be considered. Previous researchers have unanimously agreed that welded blanks are less formable than uniform sheets[1-4,53,54], although the exact reasons for the formability decrease are not agreed upon.

Other methods of manufacturing tailor welded blanks such as mash-seam welding have been practiced, but laser welding has found favor for many applications because of its high productivity rate, lack of overlap (as required in the mash-seam welding method), and small heat-affected zone, which allows for minimal distortion and cathodic corrosion resistance[3,55]. Therefore CO_2 laser butt-welding is the joining method discussed here.

2.4.1 Laser Welding Thermal Cycles

The laser welding process causes considerable metallurgical changes within steel sheet. Welding imposes a thermal cycle on the sheet, yielding heat flow conditions that have been modeled by Rosenthal for two-dimensional heat flow conditions (applicable in the welding of thin sheet):

$$\frac{2\pi(T-T_0)k_s g}{Q} = \exp\left(\frac{Ux}{2\alpha_s}\right)K_0\left(\frac{Ur}{2\alpha_s}\right) \qquad (2\text{-}10)$$

where T is temperature, T_0 is preheat temperature, k_s is thermal conductivity, g is sheet thickness, Q is heat input, U is welding speed, α_s is thermal diffusivity, K_0 is the modified zero order Bessel function of the second kind, and r is the radial distance from the origin[56]. The heat flow equation can be manipulated to determine the thermal cycle (temperature as a function of time, indicating the heating and cooling rates) at different distances from the weld source, which could lie within the fusion zone, heat-affected zone, or base metal. Several trends are noticed for low heat input processes such as the laser welding:

1. The heating rates and cooling rates are much greater (more severe) in laser welding than in arc-welding processes. Heating rates in excess of 6000°C/s are possible, and cooling time from 800°C to 500°C may take less than 1 s [57];
2. Because of the extreme thermal cycle, the temperature gradient is correspondingly large, giving rise to a small heat-affected zone;

3. The peak temperature, heating rate, and cooling rate all diminish rapidly as the distance from the weld centerline increases.

These three effects determine the metallurgical response, which determines the mechanical properties and forming behavior of the welded blank.

The size of the fusion zone and heat affected zone are also important considerations. An experimentally verified model developed specifically for laser welding processes has been proposed by Steen et. al.:

$$\frac{d_\alpha}{d} = \left(\frac{4}{\pi}\right)^{\frac{1}{2}} P^{-\frac{1}{2}} - \frac{(\theta_\alpha - 1)}{Q} \tag{2-11}$$

which predicts the penetration and/or transformation hardening depth d_α as a function of d, laser beam width; θ_α, the ratio of penetration temperature to far-field temperature; and P and Q, dimensionless laser-scan speed and absorbed power, respectively[58]. Conceptually, the equation shows that increases in travel speed cause decreases in weld width (both fusion zone and heat affected zone), whereas increases in absorbed power increase the size of the width. These parameters play an important role in determining the formability of the welded sheet.

2.4.2 Fusion Zone Effects

The fusion zone experiences the most rapid cooling rates through the austenitic region. Although no specific continuous cooling transformation (CCT) diagram is cited here, it is likely that the fusion zone will consist of nonequilibrium microconstituents, such as martensite, bainite, and acicular ferrite. Other researchers evaluating laser welded blanks have identified these same microstructures in grades with lean alloy content and correspondingly low hardenabilities (i.e., propensity to form martensite)[1,2]. Even at carbon contents as low as 0.01 wt%, the cooling rate in laser welded fusion zones was rapid enough to allow for the formation of martensite[53], although at this small carbon content an additional phase—polygonal ferrite—actually formed in the fusion zone.

Intuitively, the presence of martensite seems objectionable, considering the observed hardness increases in the fusion zone (and attendant increases in strength and decreases in ductility) may be responsible for the poor formability of welded blanks. This possibility has been acknowledged in the case where the weld is oriented parallel to the major strain axis, in which weld ductility limits the formability of the blank[1].

For the case where the major strain axis is oriented perpendicular to the weld, the decreased ductility brought about by the presence of martensite in the fusion zone does not affect formability. Baysore noted that laser welds made at faster scan speeds (thereby increasing the cooling rate and allowing for more martensite formation) exhibited increased hardness, yet the formability values did not decrease[2]. This suggests that

fusion zone hardness has little direct effect on formability in the case of the perpendicular strain axis-weld orientation.

It should be recognized that none of the papers in the literature have attempted to correlate formability to the type, character, or amount of microconstituents appearing in the fusion zone.

2.4.3 Heat Affected Zone Effects

The role the heat affected zone plays in the formability of laser welded blanks has not been well established, and little literature deals with the issue. Some authors have taken hardness measurements to determine the size of the HAZ, and then correlate increases in HAZ size with decreases in formability; see section 2.5.4. In microstructural terms, Baysore indicated the presence of nitrides and carbides both at grain boundaries and within the matrix, but did not carry his analysis any further[2].

Expanding the discussion of the HAZ to encompass arc-welding processes may provide valuable background information. The effect of nitrogen in the HAZ has been a topic of much debate and concern because of reported deleterious effects to toughness. More recent research has indicated that nitrogen may actually help toughen weldments in steels with nitrogen-binding elements, which allow beneficial precipitation behavior in the HAZ[59]. While the toughening properties of these precipitates are not of immediate interest in this discussion, the precipitation characteristics of TiN and VN and the

associated austenite grain pinning effects during welding (Figure 2-18) may effect the formability of welded blanks if they are indeed present in laser welded HAZ, as reported by Baysore. The strain hardening behavior of a relatively fine-grained HAZ (possibly containing martensite) may be of particular value in understanding formability (Figure 2-17).

Table 2-1: Current automotive applications for high strength hot rolled steel grades[6]

Strengthening mechanism	Main element	TS level (MPa)	Characteristics	Available coating	Practical uses
Solid solution	Si-Mn Nb Nb+V	490-590	Good bendability	EG, GI, GA Zn-Ni	Structural components frames, members Underbody parts
Precipitation	Nb,Ti,Si Nb+Ti Nb+Ti+Cr	490-780	Drawing type High stretch flangeability	GA, GI, EG Zn-Ni	Structural components Underbody parts Wheel rim Brackets
Multi-phase (Martensite)	Si-Mn Si,Cr	540-980	High elongation and low yield stress Low yield ratio	GA	Underbody parts Wheel disk
Multi-phase (Bainite)	Si-Mn Si-Mn-Nb Cr Ti+Cr	440-780	High stretch flangeability High elongation	GA, GI, EG Zn-Ni	Suspensions Engine-support
Multi-phase (M+B)	Si,Ti	590-780	High hole expanding ratio		Underbody parts Door impact beam
Multi-phase (Retained austenite)	Si-Mn Si,(Cr,P)	590-980	TRIP type High elongation Good balance with strength and ductility	GA Zn-Ni	Bumper Underbody parts Wheel disk Door impact beam

Special steels	Main element	TS level (MPa)	Characteristics	Available coating	Practical uses
Anti-corrosion type	Cu-P (Ni,Si,Ti,Cr) (Ni,Mo)	370-780	Good corrosion resitance	GA, GI, EG Zn-Ni	Structural components Underbody parts Suspensions
Thermal hardening type	Cu (Ni)	440-590	Strength increase by suitable heat treatment		Frames, Members Susupensions Engine-support

Table 2-2. Current automotive applications for high strength cold-rolled steel grades[6]

Strengthening mechanism	Main element	TS level (MPa)	Characteristics	Available coating	Practical uses
Solid solution (low carbon)	P-Mn Si-Mn P	340-440	Drawing type Good stretchability BH type	EG, GI, GA Zn-Ni Zn-Fe	Outer panels Inner panels Members Brackets Pillars
Solid solution (Ultra low carbon)	P-Mn P-Si Mn-P-Ti Ti,Nb	340-590	Deep drawability BH type	EG, GA, GI Zn-Ni Zn-Fe	Deep drawing type parts Outer panels Inner panels
Precipitation	Mn Nb Si-Mn-Nb	390-590	Good weldability	EG, GI, GA Zn-Ni Zn-Fe	Inner panels
Solid solution + Precipitation	Mn-Ti Si-Mn-P-Nb Cu-Ti	490-590	Good bendability High r value type	GA Zn-Ni Zn-Fe	Reinforcement Brackets
Multi-phase (Martensite) (M+B)	Mn-Si Mn-Si-P Mn Si-Mn-Nb	490-1470	Low yield ratio BH type	Zn-Ni Zn-Fe EG	Inner panels Structural components Reinforcement Bamper
Multi-phase (Bainite)	Mn-Cr	440-590	High stretch flangeability High elongation	GI, GA	Members Brackets Reinforcemnt
Multi-phase (Retained austenite)	Si-Mn	590-980	TRIP type High elongation	Zn-Ni Zn-Fe EG	Structural components
Precipitation + Multi-phase	Mn-Si-Ti Mn-Si-Ti-Mo	780-1470	Ultra-high strength		Bamber reiforcement Door impact beam

Table 2-3. Dimensional Limitations of Hot Rolled Sheet [8]

Thickness Range		Width Range	
(mm)	(In.)	(mm)	(In.)
5.839 to 4.571	0.2250 to 0.1600	Over 304.8 to 1219.2, incl.	Over 12 to 48, incl.
4.570 to 1.140	0.1799 to 0.0449	Over 304.8 to over 1219.2	Over 12 to over 48

Dimensional Ranges of Strip.

Width		Thickness	
(mm)	(In.)	(mm)	(In.)
Up to 88.9, incl.	Up to 3½, incl.	0.648 to 5.156, incl.	0.0255 to 0.2030, incl.
Over 88.9 to 152.4, incl.	Over 3½ to 6, incl.	0.874 to 5.156, incl.	0.0344 to 0.2030, incl.
Over 152.4 to 304.8, incl.	Over 6 to 12, incl.	1.140 to 5,839, incl.	0.0449 to 0.2299, incl.

Table 2-4. Product Classification by Size of Flat Cold-Rolled Carbon Steel[60]

Width		Thickness		
(mm)	(in.)	6.35 mm (0.2500 in.) and thicker	6.34 mm (0.2499 in.) to 0.361 mm (0.0142 in.)	0.358 mm (0.0141 in.) and thinner
To 304.8, incl.	To 12, incl.	Bar	Strip[1,2]	Strip[1]
50.8 to 304.8, incl.	2 to 12, incl.	Bar	Sheet[3]	Strip
Over 304.8 to 608, incl.	Over 12 to 23 15/16, incl.	Strip[2]	Strip[2]	Strip
Over 304.8 to 608, incl.	Over 12 to 23 15/16, incl.	Sheet[4]	Sheet[4]	Black Plate[4]
Over 608	Over 23 15/16	Sheet	Sheet	Black Plate

[1]When the width is greater than the thickness with a maximum width of 12.7 mm (½ inch) and a cross-sectional area not exceeding 32.28 mm² (0.05 in.²), and the material has rolled or prepared edges, it is classified as **flat wire.**

[2]When a particular temper is defined in ASTM specification A 109, or a special edge, or special finish is specified, or when single-strand rolling is specified in widths under 609.6 mm (24-in.).

[3]Cold-rolled sheet coils and cut lengths, slit from wider coils with No. 3 edge (only) and in thicknesses 0.36 to 2.09 mm (0.0142 to 0.0821 inch) incl., carbon 0.20 per cent maximum.

[4]When no special temper, edge or finish (other than Dull or Luster) is specified, or when single-strand rolling widths under 609.6 mm (24 in.) is not specified or required.

Table 2-5. Capabilities of North American Thin Slab Hot-Rolling Facilities in 1998[9]

Company	Technology	Slab Dimensions Thickness x Width mm x mm	Minimum Gauge mm	Mill Configuration	Tonnage/Year Million Tonnes
Acme Metals Riverdale, Illinois	CSP	50 x 900-1560	1.25	7 Finishing Stands	0.9/1.8
Armco Mansfield, Ohio	CONROLL®	75-125 x 635-1283	1.7	5 Finishing Stands	0.7/1.1
Algoma Sault Ste. Marie, ON	Danieli	70-90 x 800-1600	1.0	1 Roughing Stand 6 Finishing Stands	2.0
Geneva Steel Provo, Utah	Slab/CSP	150-250 x 3200 or 50 x 1220-1560	1.5	Multi-Stand Plate Mill	1.9
Gallatin Warsaw, Kentucky	CSP	55 x 990-1560	1.2	5 Finishing Stands	1.2
HYLSA Monterrey, Mexico	CSP	50 x 790-1350	0.98	6 Finishing Stands	0.75
IPSCO Montpellier, Iowa	MDH	152 x 3000	2.3	Steckel	0.9
North Star BHP Delta, Ohio	Sumitomo	90 x 1524	1.42	2 Roughing 5 Finishing Stands	3.0
Nucor Crawfordsville, Indiana	CSP	50 x 900-1350	1.6	6 Finishing Stands	1.8
Nucor Hickman, Arkansas	CSP	50 x 900-1350	1.8	6 Finishing Stands	2.2
Nucor Berkeley County, SC	CSP	50 x 900-1350		6 Finishing Stands	1.5
Nucor Charleston, SC	CSP	50 x 900-1680	1.8	6 Finishing Stands	1.8
Steel Dynamics Bulter, Indiana	CSP	50 x 990-1625	1.0	6 Finishing Stands	1.4-2.4
Tricor Steel Decatur, AL	Sumitomo	70-90 x 1650	1.0	2 Roughing Stands 5 Finishing Stands	2.2
Tuscaloosa Steel Tuscaloosa, Alabama		127 x 2590	63.5 plate	Steckel Mill	1.0
World Class Steel Pittsburgh, PA	TSP	125 x 800-1600		Twin-Stand Reversing	

Technology Suppliers

CSP - Compact Strip Production
MDH - Mannesmann Demag Huttentechnik
CONROLL® - Voest Alpine Industrieanlagen bm

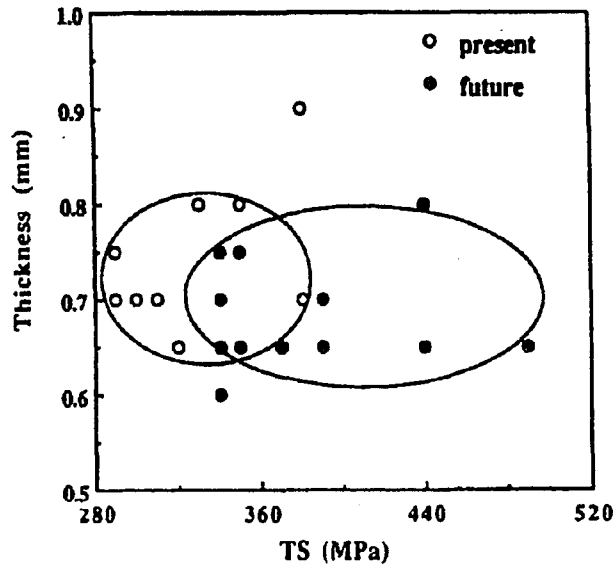

Figure 2-1. Current and projected thickness and tensile strength of steel sheets used for outer panels[7].

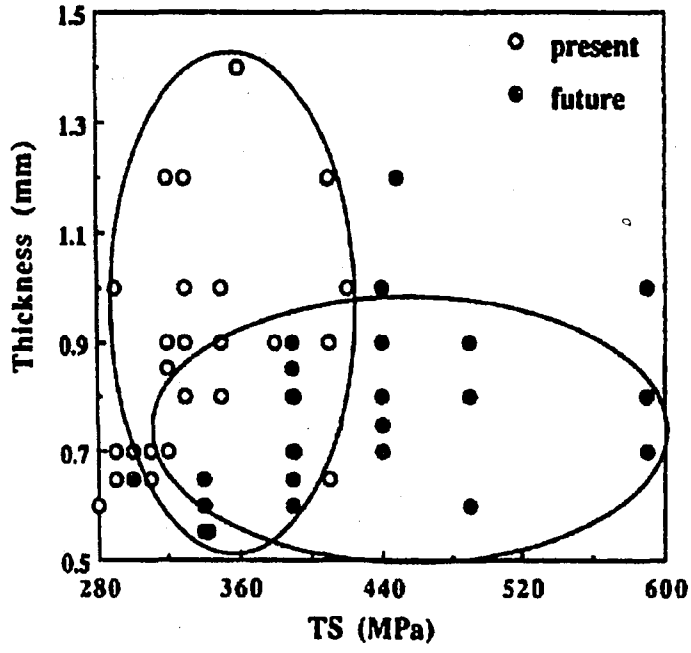

Figure 2-2. Current and projected thickness and tensile strength of steel sheets used for inner panels[7].

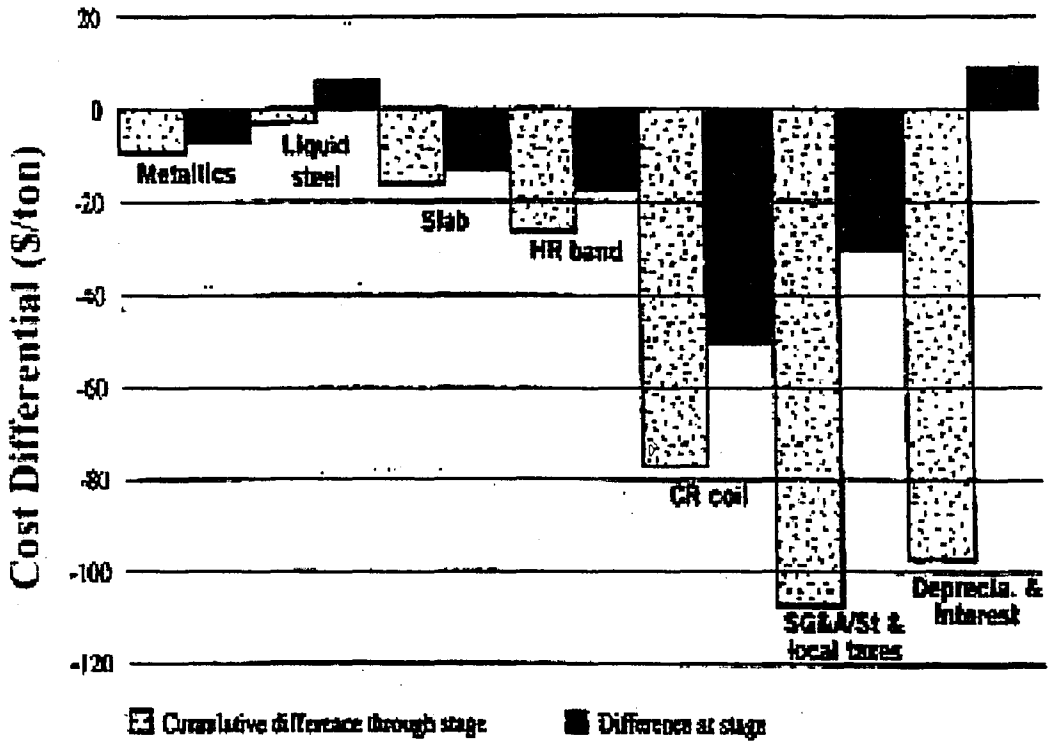

Figure 2-3. Difference in cost between thin-slab mill and low cost integrated mill, at each processing step[10].

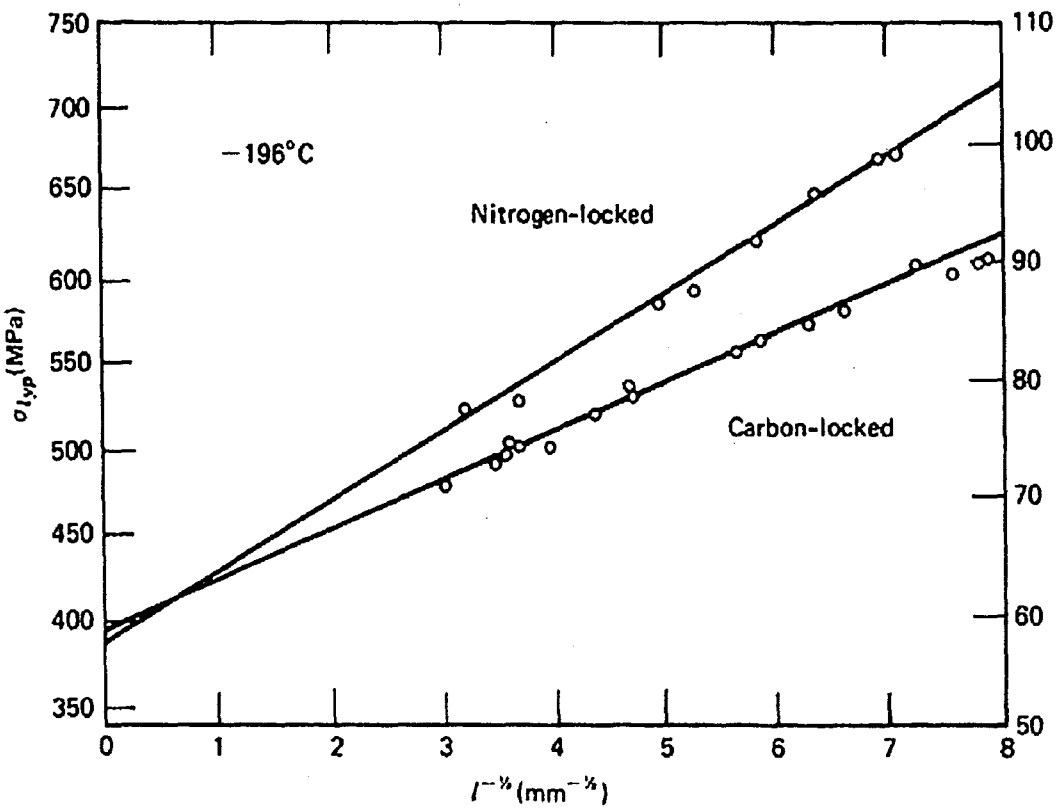

Figure 2-4. Effect of interstitial alloying on grain size strengthening contribution as a result of changes in the dislocation locking parameter, k_y [15].

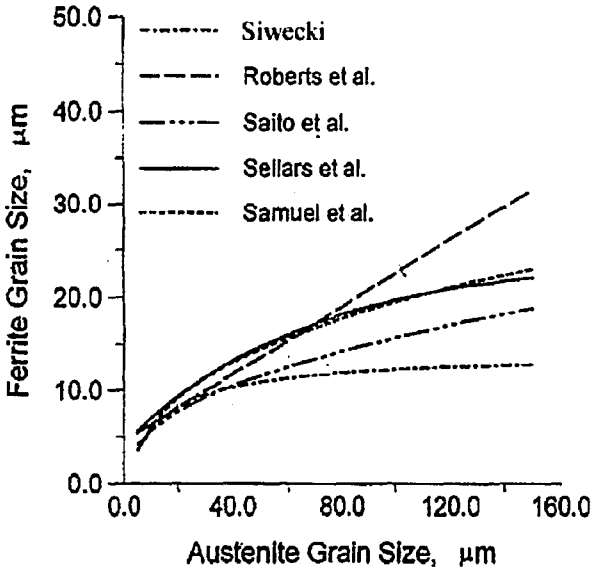

Figure 2-5. The dependence of ferrite grain size on initial austenite grain size as calculated in various studies. (Cooling rate, 4°C/S, Finishing Temperature 975°C, zero accumulated strain)[22].

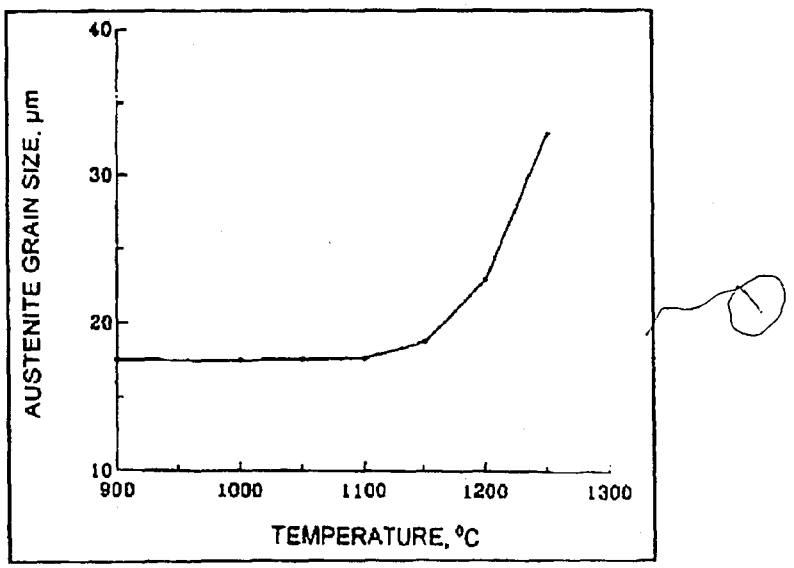

Figure 2-6. Typical grain growth characteristics of continuously cast Ti bearing grades (Ti-V-N steel with 0.17%C, 0.1%V, 0.015% Ti, 0.015%N)[20].

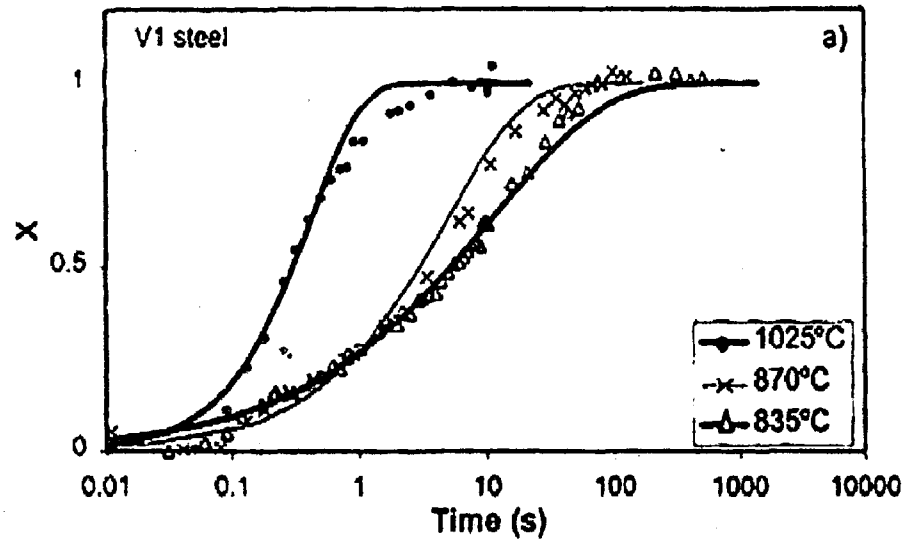

Figure 2-7. Softening curves obeying Avrami kinetics showing statically recrystallized volume percent as a function of time at different temperatures for a V microalloyed steel[61].

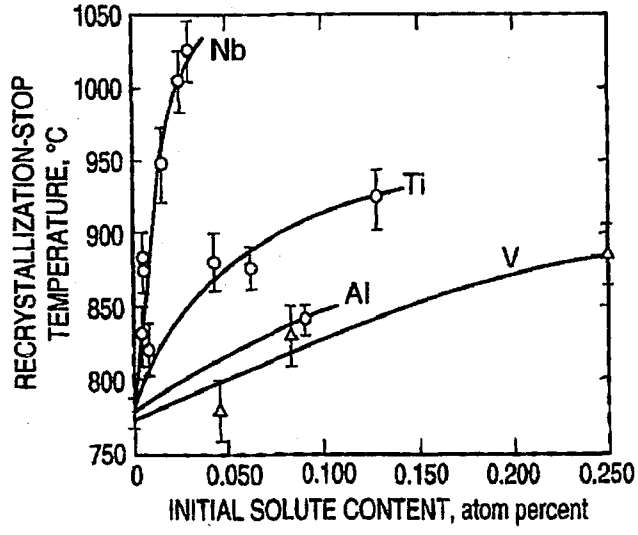

Figure 2-8. The recrystallization stop temperature, T_{nr}, as a function of common microalloy solutes in 0.07C-0.25Si-1.40Mn steel[62].

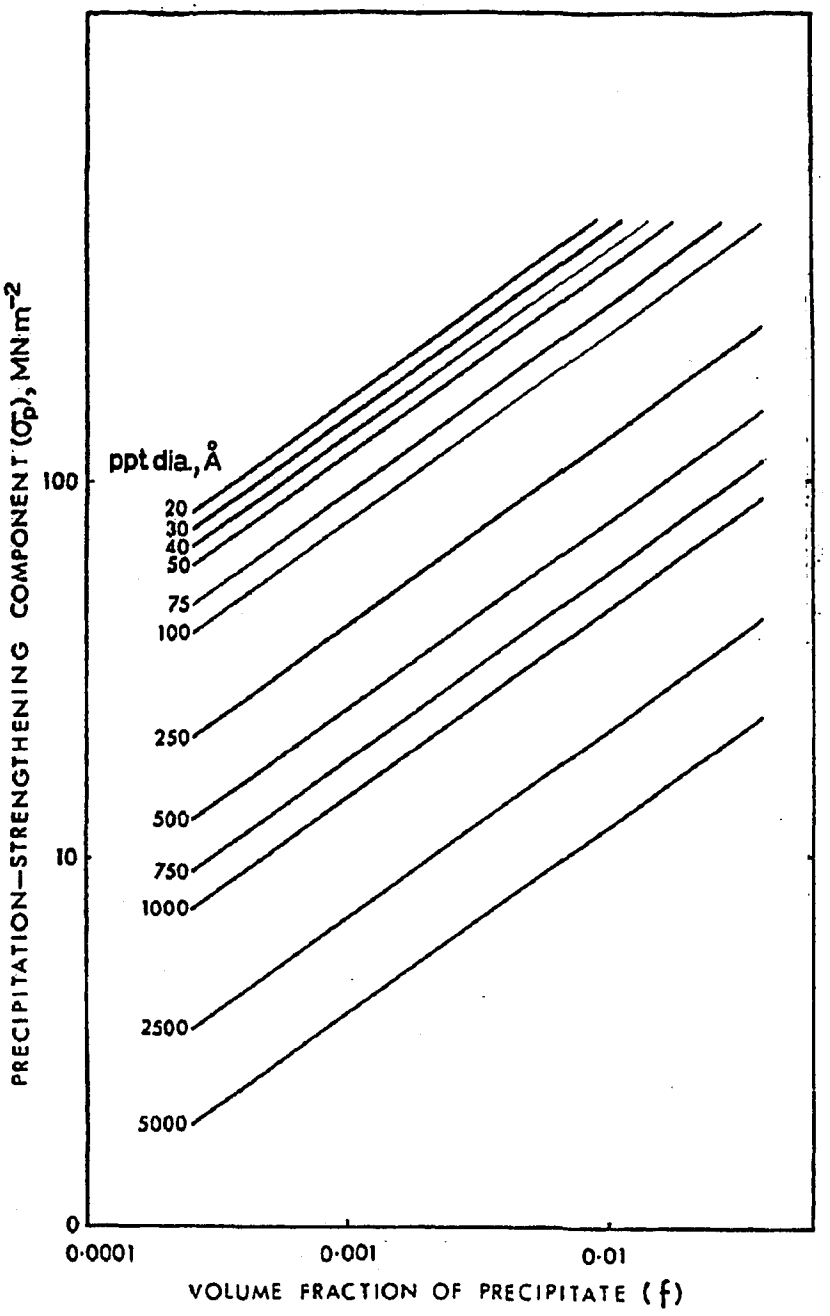

Figure 2-9. Theoretical contribution of precipitation strengthening to yield strength in steels[36]. The Orowan-Ashby model indicates that the amount of precipitation strengthening depends upon precipitate size and volume fraction.

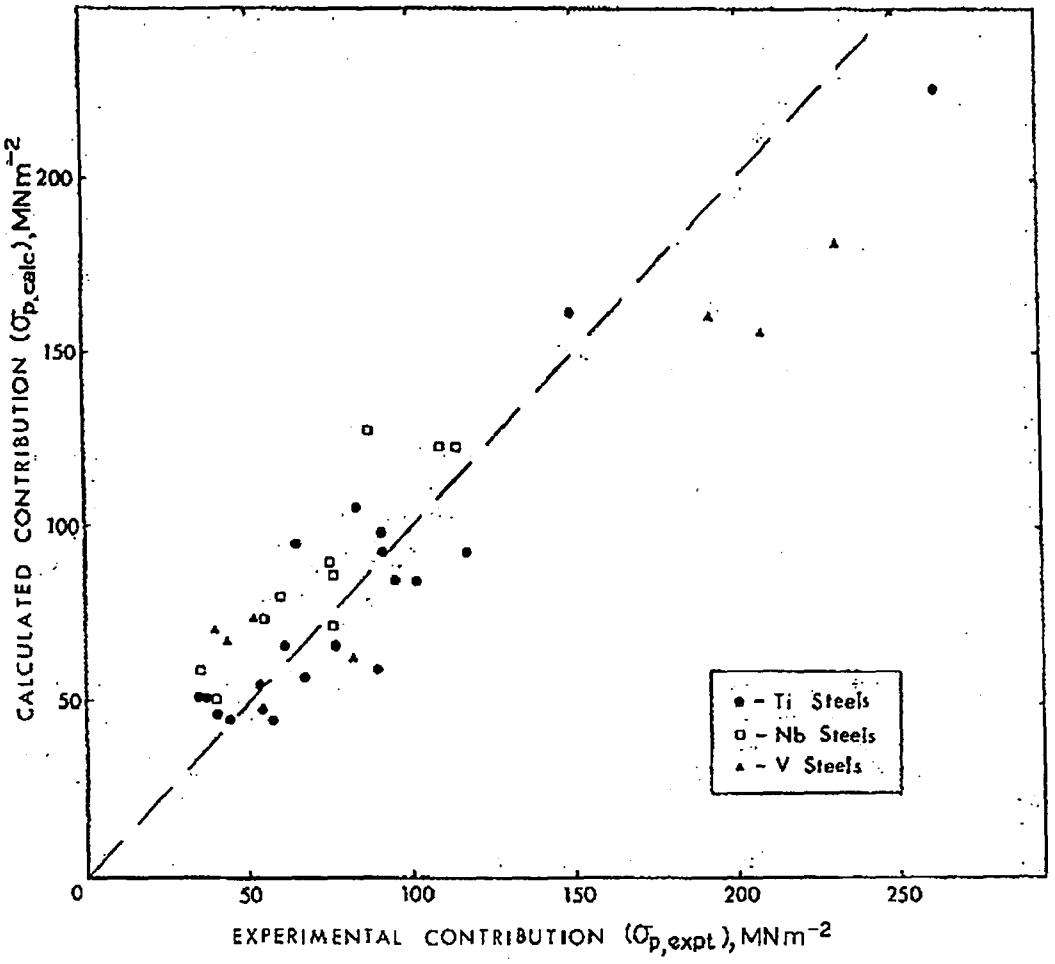

Figure 2-10. Comparison of experimentally measured and theoretically calculated precipitation-strengthening contributions for different microalloyed steels[36].

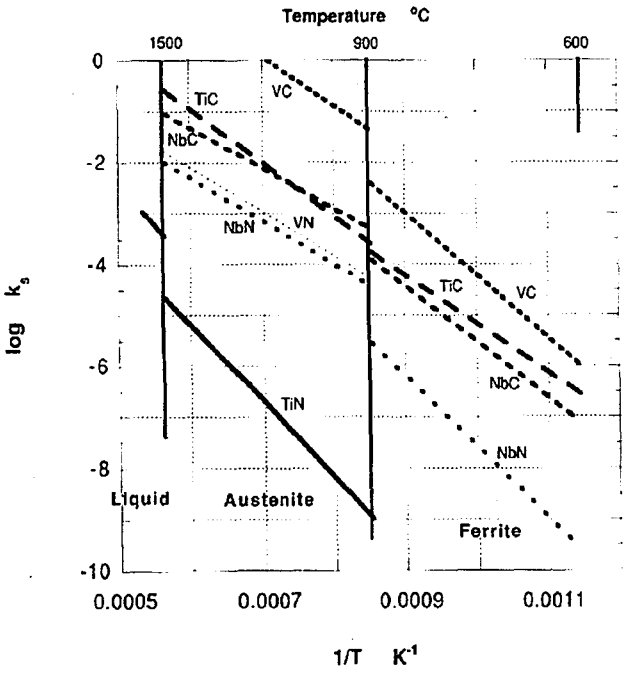

Figure 2-11. Comparison of solubility products of microalloyed carbides and nitrides over a range of temperatures[37].

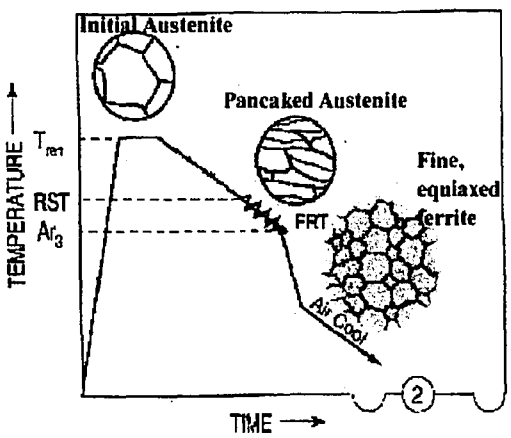

Figure 2-12. Schematic of the controlled rolling (CR) thermomechanical processing route. The microstructure evolves from coarse austenite, recrystallizing before being finished below the recrystallization stop temperature (RST). The pancaked austenite grains transform to fine equiaxed ferrite grains upon cooling below the Ar_3.

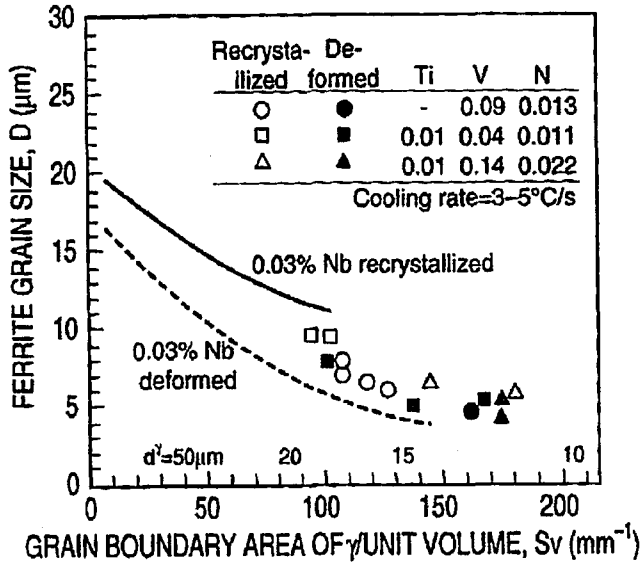

Figure 2-13. Dependence of ferrite grain size on the austenite grain boundary area per unit volume, as determined using Ti-V and V steels. Curves represent Nb-microalloyed steels.

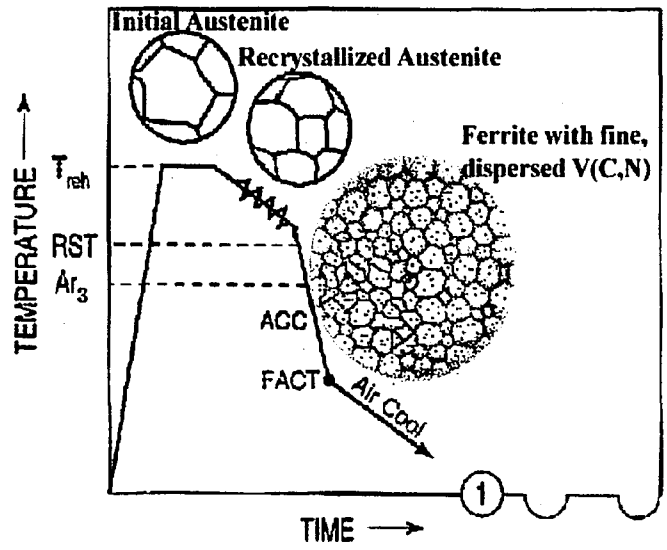

Figure 2-14. Schematic of the recrystallization controlled rolling (RCR) thermomechanical processing route. Coarse austenite grains are refined through repeated static and dynamic recrystallization passes.

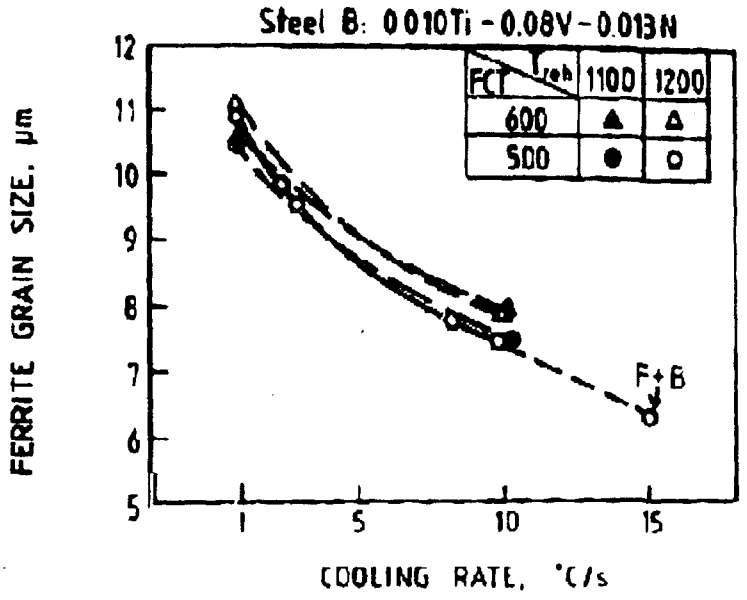

Figure 2-15. Effect of cooling rate from finish rolling temperature of 1030°C to finish-cooling temperature (FCT) on the ferrite grain size of Ti-V-(Nb)-N steels. Final reduction 25%[62].

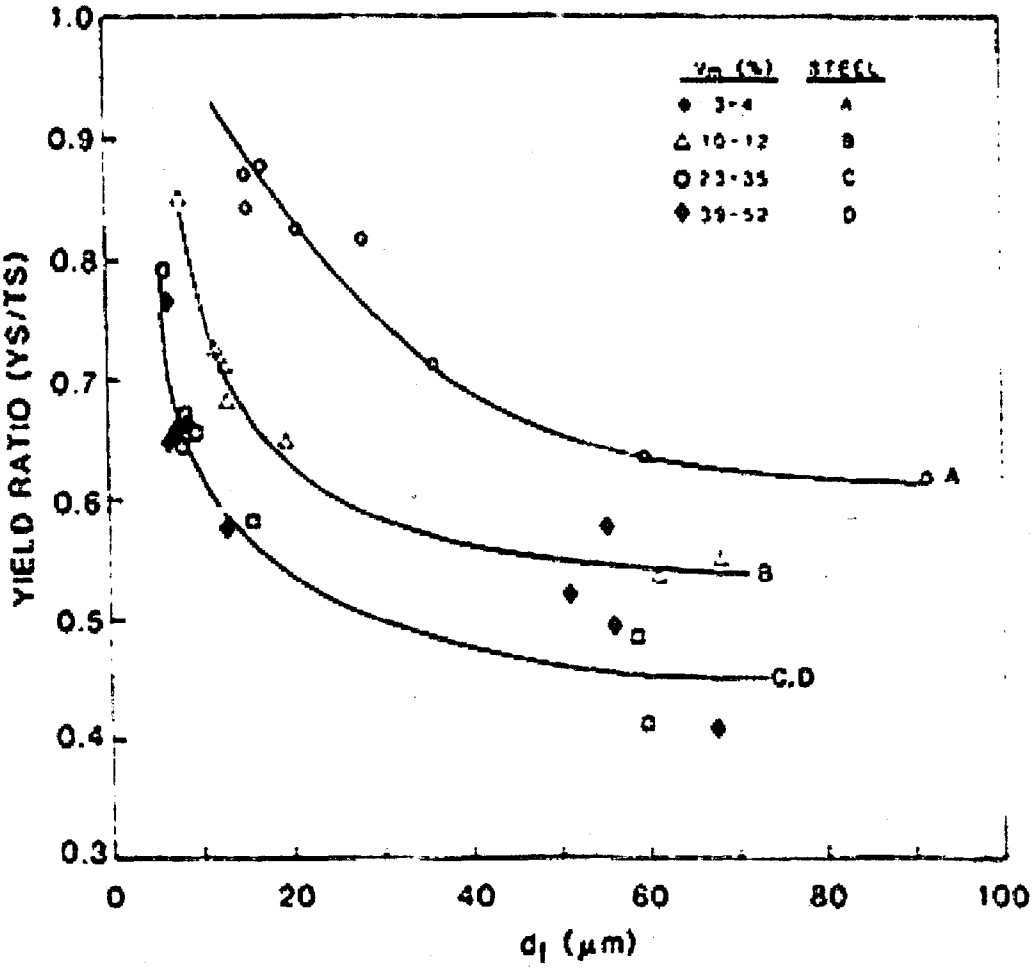

Figure 2-16. Effect of ferrite grain size, d_f, and martensite volume fraction, V_m, on the yield ratios of various dual phase materials[51].

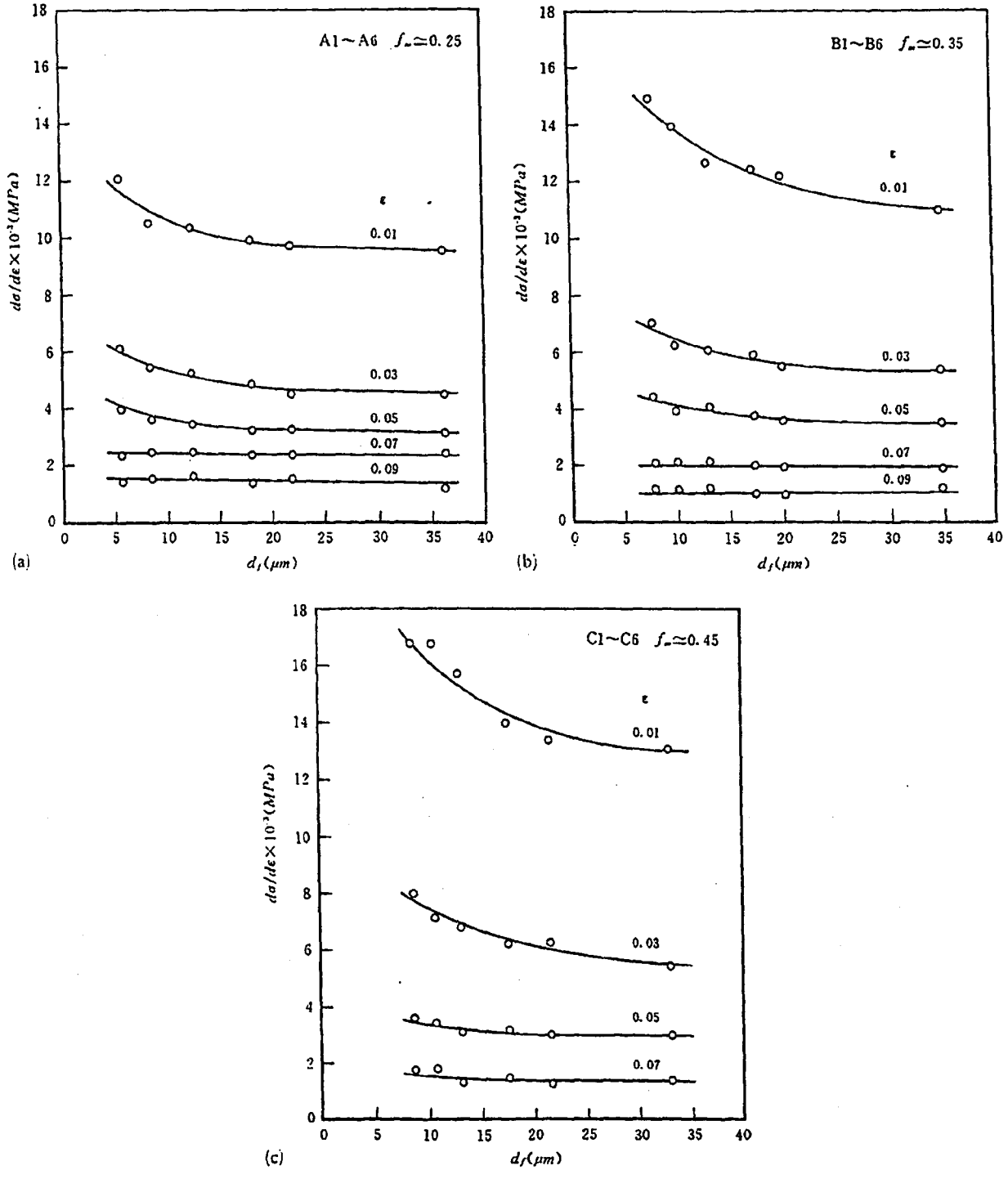

Figure 2-17. Change in strain hardening rate with ferrite grain size in various dual phase steels: a) martensite volume fraction ~0.25; b) martensite volume fraction ~0.35; c) martensite volume fraction ~0.45[50].

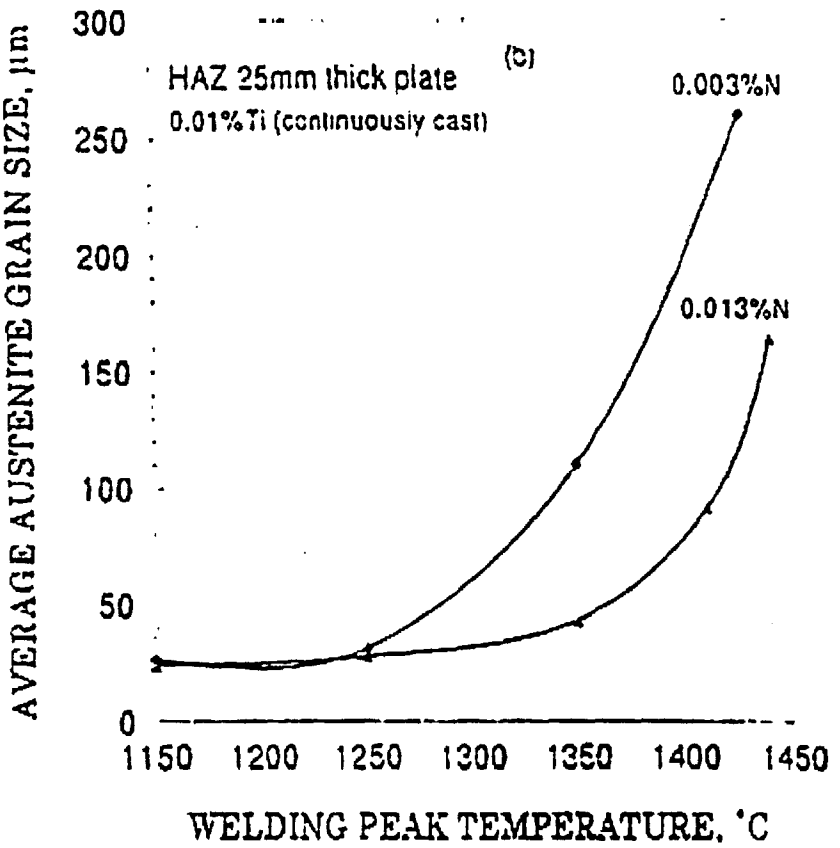

Figure 2-18. Austenite grain pinning effects of TiN precipitates present in the HAZ of microalloyed steels[59].

3. Experimental Procedure

3.1 Material System

Five hot-rolled microalloyed grades representing a range of compositions, strength levels, and gages were selected for this study for the reasons outlined in section 2.2. Table 3-1 summarizes the compositions and gages of the as-rolled material. The material was machined into square blanks 12 inches x 12 inches.

3.2 Tensile Testing of As-Rolled Materials

Tensile tests of the as-received grades were performed as per ASTM E8[63] using an Instron 4206 tensile machine. Standard tensile specimens, as shown in Figure 3-1, were machined in three orientations, 0°, 45°, and 90° from the rolling direction; tests were run in triplicate at a crosshead speed of 0.010 inches per minute. Strain measurements were taken with a 2 inch extensometer.

3.3 Laser Welding

To prepare for welding, the as-rolled 12 inch x 12 inch blanks were wire brushed vigorously to remove remnant scale from the hot rolling process.

Welding was performed with a CO_2 laser because of the popularity of that joining method in the industrial fabrication of TWBs. Specifically, an 8 kW continuous wave CO_2 Trumpf laser was used in welding all grades. Noble Metals Processing, a commercial producer of TWBs, provided the facilities and firsthand experience in welding each grade in a manner consistent with industrial practice.

Welding parameters (laser power and travel speed) were selected to produce a single, continuous, full-penetration autogenous weld along the mid-width position of each 12 inch x 12 inch blank, as shown in Figure 3-2. One set of welding parameters was decided upon for each grade, i.e., the effect of welding parameters within a single grade was not examined in this study. Because of gage similarities, Grades 1 and 2 were welded with the similar parameters, and Grades 4 and 5 were welded with similar parameters. All welds were made parallel to the rolling direction.

The blanks made in this manner cannot be considered "tailored blanks," because they do not join dissimilar sheets. Actually, no joining occurs at all; the welds are all autogenous bead-on-plate as described above and as illustrated in Figure 3-2. The matrix of experiments was intentionally designed in this manner to isolate the effects of the weld on formability, without the inherent complications that arise when considering the effects of dissimilar sheets. Entire studies have been dedicated to understanding variables such as gap and edge preparation [64,65]. These variables are undesirable in the current study and have therefore been avoided.

3.4 Characterization of Welds

Characterization of the welds was performed to determine the effect of microstructural and mechanical property gradients on the formability of laser welded blanks.

3.4.1 Sample Preparation

Samples for microstructural characterization were prepared by mounting welds in cold setting epoxy. Mounts were made to show both the cross section and the planar view of the weld. Each sample was ground and polished to 0.05 μm using a Struers ABRAPOL automatic grinder/polisher and Buehler Vibromet polisher. Samples were etched immediately after the final polishing step with 2% nital solution, 4% picral solution followed by 2% nital solution, or Marshall's Reagent. Typical etching times for all etchants were less than 10 seconds.

Metallographic specimens were prepared for mechanical characterization. Welds were mounted in planar orientation in thermosetting epoxy. Thermosetting epoxy was used in favor of cold epoxy to minimize mount compliance, as recommended when performing the automatic ball indentation technique. The samples were then ground and polished in the manner described above.

3.4.2 Microstructural Characterization

Standard quantitative metallurgical characterization techniques were performed using light optical microscopy (LOM) and scanning electron microscopy (SEM), by analyzing the planar samples of each weld. Microconstituent area fractions and grain sizes were measured in accordance with ASTM E562 and ASTM E112, respectively[63], over ten fields at each distance from the fusion zone centerline (FZCL). These techniques

allowed for characterization of the gradient in microstructures associated with the welding process. As a baseline, the as-rolled sheet was also characterized.

Quantitative microscopy was carried out as much as possible through LOM. However, some microconstituents could not be identified reliably with LOM alone, particularly because of the fine structure observed in these materials. In these instances, SEM allowed for the constituents to be identified with a reasonable degree of accuracy.

Knoop microhardness testing were performed on the planar samples used for microstructure characterization in a manner consistent with ASTM E384[63]. A 300 gram load was selected because the indentation was large enough to span several grains, making the measurement insensitive to individual metallurgical features. The long axis of the Knoop indenter was aligned parallel to the welding direction to allow for a high measurement density across the weld. Multiple rows of indentations were made, yielding measurements every 75 μm from the FZCL, Figure 3-3. Each reported value is the average of at least four measurements.

3.4.3 Automatic Ball Indentation

The ABI technique generates simulated tensile stress-strain curves by measuring applied load and displacement data during cyclic loading of a single area on a polished specimen by a rigid spherical indenter. The ABI method has been described in greater detail elsewhere[66-69]. The concept behind the technique is discussed only briefly here.

Figure 3-4 shows a schematic of the equipment needed for ABI testing, which is used to generate load-displacement curves such as those shown in Figure 3-5. From the load-displacement data, parameters such as applied load, P, and plastic indentation diameter, d_p are determined. Because of the spherical geometry of the indenter, the load-depth data can be manipulated to allow for the calculation of simulated tensile stress-strain values by the following equations:

$$\varepsilon_p = 0.2\frac{d_p}{D} \tag{3-1}$$

$$\sigma_t = \frac{4P}{\pi d_p^2 \delta} \tag{3-2}$$

where the true plastic strain, ε_p, is found to be a function of d_p, the plastic indentation diameter, and D, the diameter of the ball indenter. The true stress, σ_t, is calculated as a function of applied load, P, the plastic indentation diameter after each cycle, d_p, and δ, a parameter whose value depends in a complex manner on the development of the plastic zone caused by the indention. The plasticity theories governing the flow equations in the case of spherical indentation were developed largely by Tabor[70] and Nadai[71].

3.5 Development of Laser Welding Model

A simple two-dimensional heat flow model was developed using the SYSWELD software package to model the thermal cycles in the laser welds. Many studies have approximated welding processes by using the original Rosenthal model[56] or variations thereof, which assume a point heat source. However, studies have indicated that such models become increasingly inaccurate at distances close to the heat source, suggesting

the point heat source should not be used to approximate weld thermal cycles in regions where the peak temperature exceeds one-fifth of the melting temperature [72]. Therefore point sources were deemed unsuitable to estimate the fusion zone thermal cycles of interest in this study.

For this reason, a more realistic volumetric heat source was assumed in this model. The heat source assumed a gaussian power distribution over a conical or cylindrical volume, Figure 3-6, the details of which were determined as follows. The total power of the heat source, i.e., the summation of the power density distribution function over all its volume elements, was equated to the power delivered to the workpiece:

$$\int_0^{2\pi} \int_{y_b}^{y_t} \int_{r_b}^{r_t} PDDF(r, y, \theta) dr dy d\theta = \eta_t P$$

where the y_t, y_b, r_t, and r_y values are represented as labeled in Figure 3-6, the power density distribution function (PDDF) is as described above, η_t is the transfer efficiency, and P is the output power of the laser. A transfer efficiency of approximately 0.30, is commonly observed in laser welds made in conduction mode[73], and was assumed in this model. The values of y_t, y_b, r_t, and r_y were then adjusted so that the model predicted fusion zones that had the same geometry as were observed experimentally. This somewhat empirical approach has been used by others[74] and is expected to yield accurate predictions of weld thermal cycles.

Because of the rapid thermal cycles and steep temperature gradients expected in laser welds, the mesh and time steps used in this analysis were extremely refined. A separate mesh, each comprised of two-dimensional 8 node quadrilateral elements, was generated for each plate thickness (1.225 mm, 2 mm, and 3 mm), Figure 3-7. The meshes were refined until further refinement resulted in no appreciable change in weld thermal cycles, indicating mesh independence.

Because of the rapid nature of laser weld thermal cycles, conduction was expected to be the predominant mode of heat transfer. To accurately model conductive heat transfer, temperature dependent thermophysical properties of low carbon steel were applied in the model, as suggested in the literature[75].

Other mechanisms of heat transfer, i.e., convection and radiation, were also considered. Recommended convective heat transfer coefficients of 10 Wm^2-K [76] and emissivity values of 0.9 (typical of hot rolled steels[77]) were assumed. Neither mechanism is expected to contribute significantly to the calculated weld thermal cycles.

Two notable simplifications were made in this model. The phenomenological basis of weld pool convection was not considered; rather, the values of thermal conductivity at temperatures in the liquid region were artificially increased in the model. The conductivity values that were used have been shown to accurately predict weld pool convection in arc welds[75,77], but have not been verified in the context of laser welds.

Also, the latent heat of fusion associated with melting and solidification were not considered. These simplifications are discussed further in the context of the model results.

3.6 Heat Treatment of As-Rolled Grades

Based on the thermal cycle results of the laser welding model, samples of the as-rolled material were exposed to an austenite and quench heat treatment in an attempt to assess the possibility of autotempering in the fusion zone of laser welds. A chromel-alumel thermocouple was drilled into the midwidth, midthickness position of each sample, which was 0.50" x 0.75" x thickness. This allowed for direct measurement of quench rates during the heat treatment (1000°C for 15 minutes, followed immediately by quenching in iced brine, a saturated NaCl solution).

The austenitized and quenched samples were then mounted in cross section and polished as described in section 3.4.1. A light etch in 2% nital was used to reveal martensitic areas. Microhardness testing was performed on martensite packets in the midthickness region to avoid possible decarburization effects, using a 25g load and a Knoop indenter.

Table 3-1. Compositions (wt%) and gages of as-rolled materials. Compositions determined through arc-spark spectroscopy.

	Grade 1	Grade 2	Grade 3	Grade 4	Grade 5
C	**0.069**	**0.042**	**0.056**	**0.090**	**0.085**
Mn	0.73	0.34	0.76	1.06	1.46
P	0.010	0.007	0.010	0.013	0.016
S	0.012	0.007	0.010	0.007	0.009
Si	0.014	0.018	0.015	0.062	0.310
Cu	0.075	0.049	0.110	0.022	0.120
Ni	0.008	0.010	0.009	0.007	0.007
Cr	0.034	0.023	0.029	0.027	0.026
Mo	0.020	0.010	0.021	0.026	0.035
Ti	<.001	<.001	<.001	<.001	<.001
Nb	0.005	**0.054**	0.006	0.004	0.006
V	**0.034**	0.001	**0.055**	**0.025**	**0.079**
Al	0.043	0.030	0.033	0.048	0.013
N	0.008	0.010	0.009	0.007	0.007
Fe	balance	balance	balance	balance	balance
Gage (mm)	**2.010**	**2.050**	**1.225**	**2.980**	**3.105**

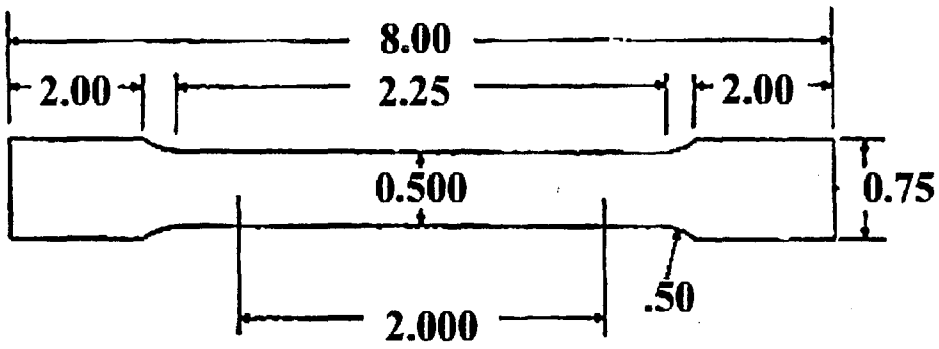

Figure 3-1. Standard tensile specimen geometry for sheet products[63].

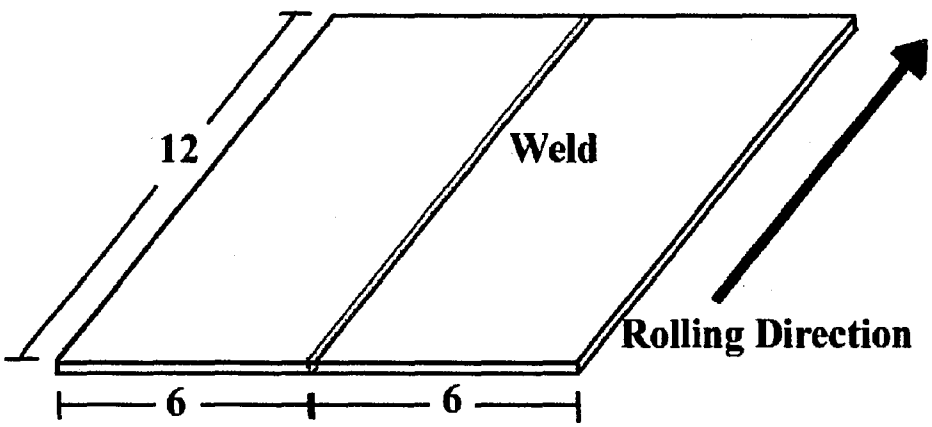

Figure 3-2. Schematic of welded blank.

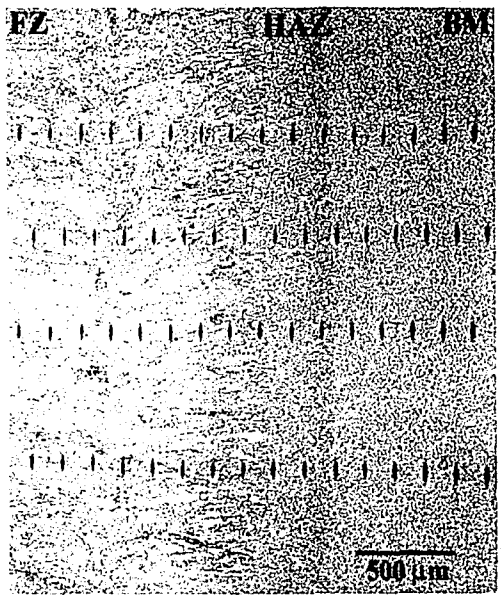

Figure 3-3. Light optical micrograph showing typical array of Knoop microhardness measurements.

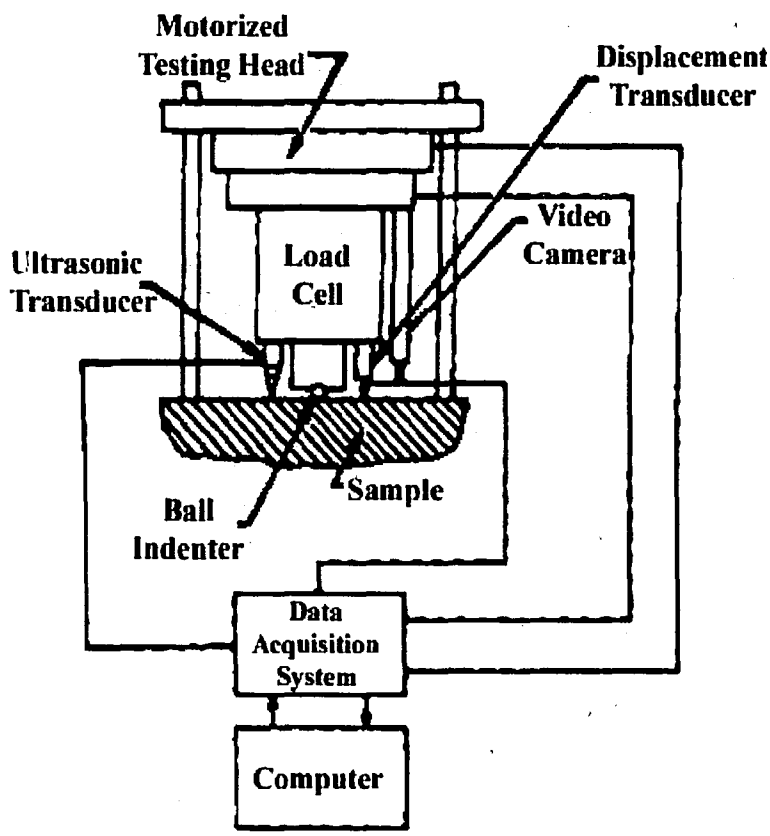

Figure 3-4. Schematic of automatic ball indentation testing apparatus.

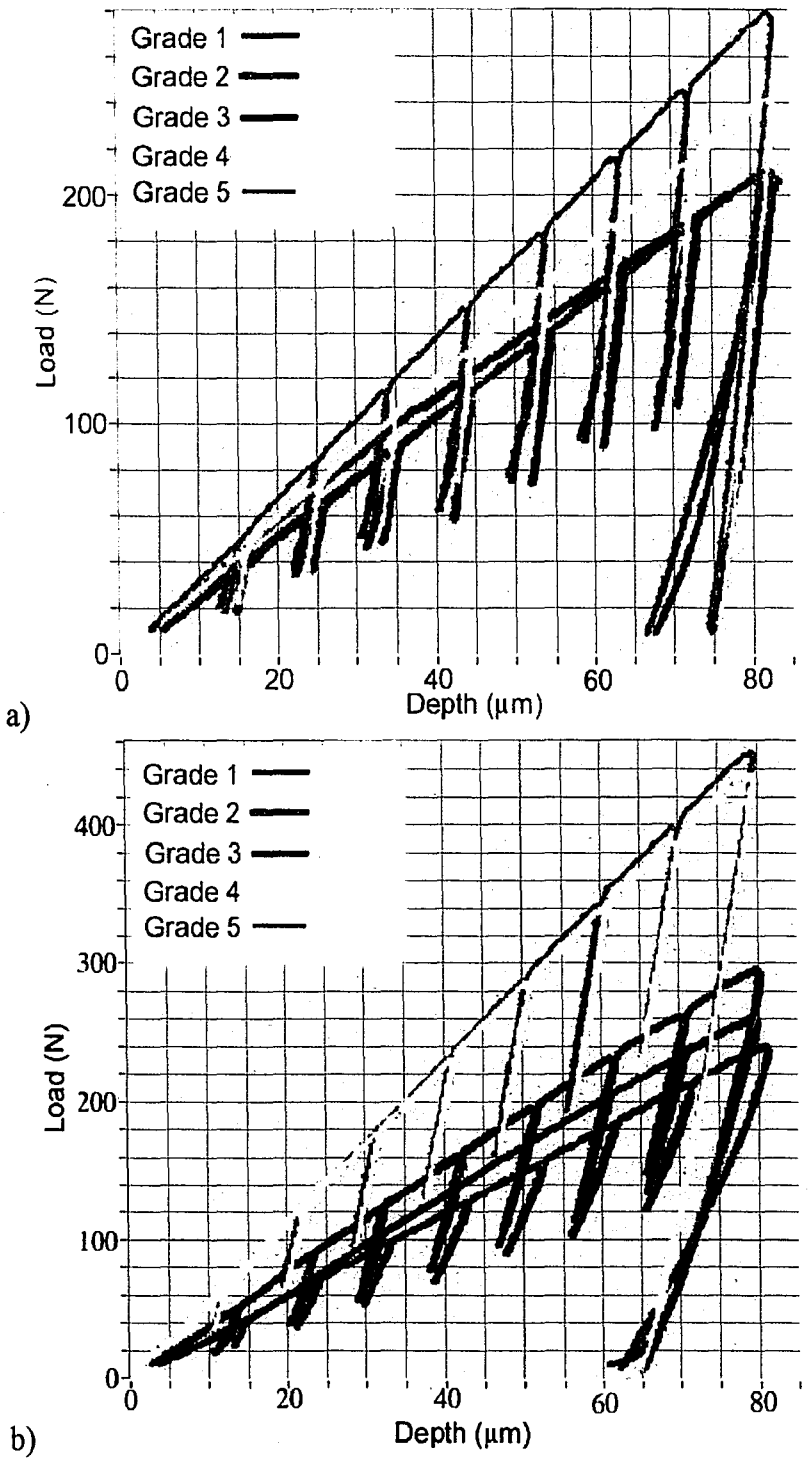

Figure 3-5. ABI load-displacement data for a) base metal indentations, and b) FZCL indentations.

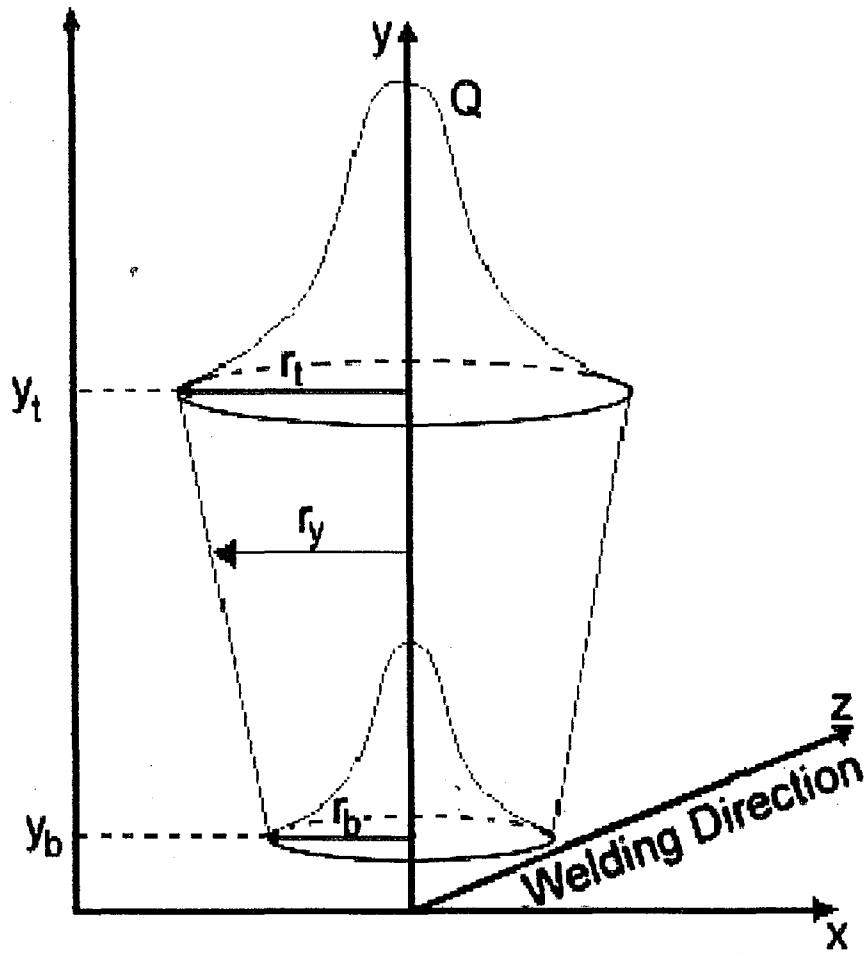

Grade	Mesh Gage (mm)	r_t (mm)	r_b (mm)	y_t	y_b
1	2.000	0.5	0.5	Top surface	1.8 mm from top surface
2	2.000	0.5	0.5	Top surface	1.8 mm from top surface
3	1.225	0.7	0.4	Top surface	1.15 mm from top surface
4	3.000	0.44	0.39	Top surface	Bottom Surface
5	3.000	0.44	0.39	Top surface	Bottom Surface

Figure 3-6. Schematic showing the assumed power distribution in the heat source.

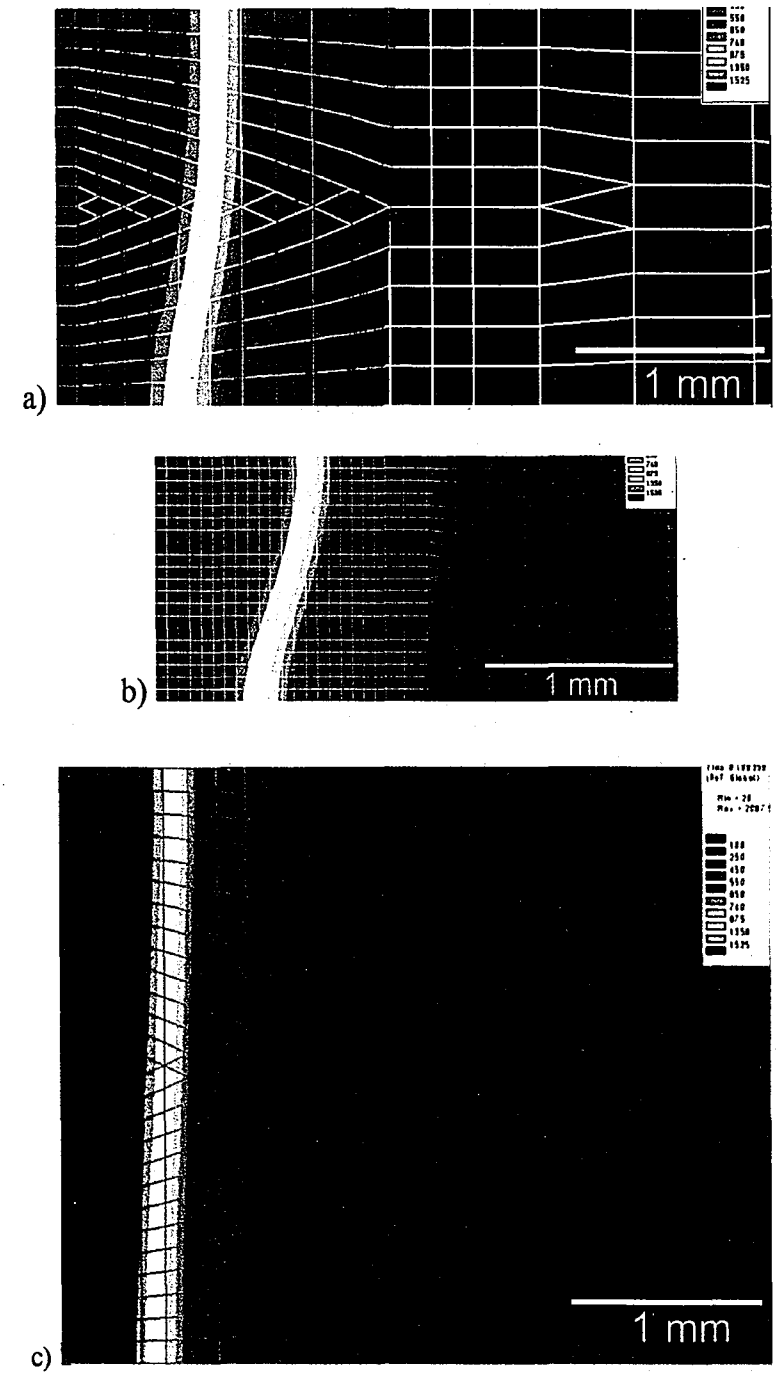

Figure 3-7. Meshes in the region of interest used in developing the laser weld heat flow model: a) grades1 and 2 (2 mm gage), b) grade 3 (1.2 mm gage), and c) grade 4 and 5 (3 mm thick gage). Contours indicate isotherms at a fixed time.

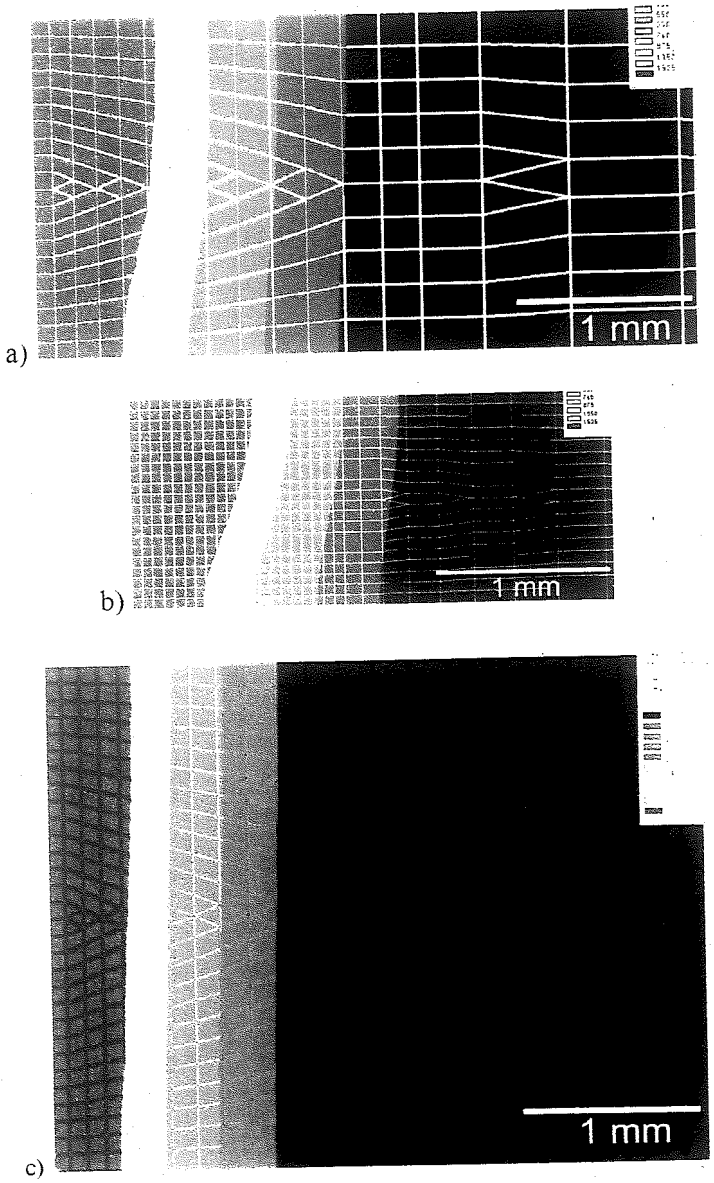

Figure 3-7. Meshes in the region of interest used in developing the laser weld heat flow model: a) grades1 and 2 (2 mm gage), b) grade 3 (1.2 mm gage), and c) grade 4 and 5 (3 mm thick gage). Contours indicate isotherms at a fixed time.

4. Results and Discussion

4.1 As-rolled Materials

4.1.1 Microstructure

Light optical micrographs of representative longitudinal sections are shown in Figure 4-1. Because of the fine microstructural features observed in these grades, scanning electron microscopy was used to more accurately delineate the microconstituents. Representative SEM images comparing the as-rolled grades appear in Figure 4-2.

Subtle differences in grain size and second phase volume fraction were quantified and summarized in Table 4-1. Grades 1, 2, and 3 have similar microstructures, marked by fine polygonal ferrite (grain size approximately 5 μm or less) and small amounts of pearlite and/or other precipitates. Pearlite was identified by the characteristic lamellar structure observed in the Figure 4-3 micrographs.

The grade 4 microstructure differed markedly from the other grades, having a bainitic-pearlitic structure, Figure 4-4. Grade 5 had a microstructure of polygonal ferrite similar to grades 1, 2, and 3, with a few notable differences. The ferrite grain size was significantly finer, approximately 3 μm. Also, the pearlite in grade 5 was noticeably banded in the rolling direction as in Figure 4-1e. In grade 5, two constituents were observed that comprised the "second phase," pearlite and another type of precipitate that was submicron in size, Figure 4-5. This is in contrast to grades 1, 2, and 3, in which the

only second phase observed by LOM or SEM was cementite within pearlite. The second phase was not identified.

It is commonly known and expected that dispersions of fine (nano-scale) (Nb,V)(C,N) exist in steels of these compositions.

4.1.2 Precipitation of Microalloy Carbides and Nitrides

Although quantitative transmission electron microscopy was not performed in this study, an attempt was made to understand what precipitates were undetected by scanning electron microscopy. Microalloy precipitation under equilibrium conditions served as the basis for the simple approach adopted here. The results of this approach allow for the estimation of 1) the temperatures at which these microalloy precipitates form and are stable, and 2) how much total microalloy precipitate is expected to exist in each grade.

This approach considers equilibrium (thermodynamics-governed) cooling from the austenite range, and assumes the formation of only simple nitrides and carbides: NbN, NbC, VN, and V_4C_3 in austenite and/or ferrite. This analysis supposes that these precipitates form in a mutually exclusive manner, meaning that only one species will form at each temperature, and that there is negligible solubility among the species. The literature indicates that both these assumptions are false; in actuality, complex microalloy carbonitrides form, indicating both competitive formation and extended solubility among these precipitates, as discussed previously.

Despite these complications, this approach remains valid. The grades involved in this study tend to be alloyed with appreciable amounts of either vanadium or niobium, but not both, Table 3-1. Also, the amount of nitrogen in these steels is fairly low, less than 0.010 wt%. These compositions conveniently minimize the amount of competitive growth between different types of precipitates. In instances where more than one microalloy precipitate is predicted to form, different precipitation sequences have been considered to give bounding values of how much of each precipitate forms.

The amount and type of precipitate that forms was estimated through the use of solubility diagrams, such as have been established for the precipitates of interest: NbN, NbC, VN, and V_4C_3; refer to Figure 4-6, Figure 4-7, Figure 4-8, and Figure 4-9, respectively. Values of each solubility product are readily available in the literature[37,78-80]. Each solubility diagram shows the solubility product as a function of composition and temperature. Compositions lying below the solubility product at a given isotherm indicate that precipitation will not occur at that temperature, whereas compositions above the solubility product isotherm are expected to precipitate in order to bring the system back to thermodynamic equilibrium. It is clear that decreasing temperature causes a shift in the solubility product to leaner matrix compositions. That is, at lower temperatures, the parent (austenite or ferrite) phase will have lower solubilities for the precipitate-forming elements.

An example of the analysis is seen when considering the equilibrium cooling of grade 2. The nominal composition is plotted alongside the solubility diagrams in Figure 4-6, Figure 4-7, Figure 4-8, and Figure 4-9. The figures indicate that NbN precipitation will occur at higher temperatures than NbC, VN, or V_4C_3, starting above 1100°C. It has been suggested that near-stoichiometric NbN precipitates should form[37], so precipitation depletes the austenite matrix of both Nb and N according to the ratio of atomic masses (approximately 93:14 Nb:N). The depletion of Nb and N in austenite during NbN precipitation reduces the driving force for Nb and N bearing precipitates. For example, Figure 4-7 suggests that NbC should begin to precipitate in grade 2 between 1050°C and 1000°C. However, NbN precipitation depleted the Nb content in the austenite from the nominal composition (0.054 wt%) to a lower effective composition (approximately 0.035 wt%) at 1050°C. This change in austenite composition decreased the onset temperature of NbC precipitation to below 1000°C.

The solubility diagrams indicate that NbN and NbC form competitively in austenite at temperatures below 1000°C. This overlap in NbN and NbC precipitation temperature ranges has been observed frequently, and the formation of complex Nb(C,N) has been attributed to this effect[37], as described previously. The competitive nature of NbC and NbN precipitation complicates the simple stoichiometry-based approach adopted here. To circumvent this complication, two bounding cases were considered:

1) The precipitation of NbN to the exclusion of NbC at temperatures below 1000°C. This assumption implies the change in austenite compositions shown by the (1-2-3A) sequence in Figure 4-6 and Figure 4-7.
2) The precipitation of NbC to the exclusion of NbN at temperatures below 1000°C. This assumption implies the change in austenite compositions shown by the (1-2-3B) sequence in Figure 4-6 and Figure 4-7.

Note that the possibility of VN precipitation in austenite was not considered in grade 2, because the nominal V composition was low enough to preclude that possibility (Figure 4-8).

Upon transformation from austenite to ferrite at approximately 900°C, it was assumed that precipitation of NbN, NbC, and VN went to completion, considering the low solubility these precipitates in ferrite as compared to austenite, as shown in Figure 2-11. Again, 1:1 atomic stoichiometries were assumed for NbN, NbC, and VN, as suggested in the literature[78,80].

Below the austenite-ferrite transformation temperature, the effective V and C composition of the ferrite was used to determine the amount of vanadium carbide precipitated, assuming a V_4C_3 stoichiometry as suggested by Taylor and others [79,81,82]. For all grades, V_4C_3 precipitation nears completion at 700°C, Figure 4-9.

This approach was applied to all alloys. The calculated weight percentages, as well as the precipitation sequences assumed in their calculation, are noted in Table 4-2. For each grade, the precipitation sequences yielding the minimum and maximum weight percent of precipitate are listed. Observe that the weight percentages calculated for each species depends heavily upon the precipitation sequence assumed, but the total microalloy precipitate content is extremely insensitive of precipitation sequence. For example, the calculated NbN content in grade 2 is calculated as either 0.033 wt% or 0.062 wt%, depending upon the assumed precipitation sequence, but the estimated total precipitate weight percentage only varies from 0.062 wt% to 0.063 wt%. As discussed previously, the calculated amount of each specific precipitate should be regarded only as an aid to calculation, with little physical significance, since observed precipitates tend to be of the complex ((Nb,V)(C,N)) nature. The importance of this calculation is in estimating the total weight percentage of microalloy precipitates, not the exact nature (chemistry or distribution) of each carbonitride. Very precise estimates of the total precipitate content were made using this approach. Table 4-2 indicates that the minimum and maximum precipitate weight percentages converge within 0.001 wt% for all grades except grade 1, in which the minimum and maximum precipitate weight differs by 0.007 wt%.

4.1.3 Mechanical Properties

Typical engineering stress-strain plots for as-rolled materials are shown in Figure 4-10, and results are summarized in Table 4-3. Ultimate tensile strengths levels for the five

grades ranged from approximately 440 MPa to 600 MPa, which is the established target for future door inners, Figure 2-2. In the steels studied here, particularly the ferrite-pearlite grades, the fine grain size (Table 4-1) and the microalloy precipitate content (Table 4-2) are expected to contribute significantly to the overall strength levels of the material, as suggested by the literature. For the ferrite-pearlite grades investigated, the strength levels for the ferrite-pearlite grades correlated well with microalloy precipitate content, Figure 4-11. This suggests that, for the small range of grain sizes in these materials, precipitation strengthening is the mechanism that best differentiates the behavior of these steels. Consideration of Figure 4-11 in light of the Orowon-Ashby precipitation strengthening model also implies similar precipitate size and distributions among the ferrite-pearlite grades, recall equation (2.5). Grade 4 is a notable outlier in Figure 4-11, indicating that the strength levels in grade 4 cannot be compared directly to the other grades, because the bainitic structure provides an additional strengthening mechanism that is absent in the ferritic grades.

It has been established that most strengthening mechanisms, with the exception of grain refinement, increase strength at the expense of ductility. The precipitation strengthened steels investigated generally reflect that tendency, with stronger grades (grades 3, 4, and 5) exhibiting smaller elongation at the ultimate tensile stress than the grades with lower strength levels (grades 1 and 2). This behavior is also noted in Figure 4-11.

4.2 Laser Welding Model Results

Evaluation of the weld thermal cycles at the fusion zone centerline (FZCL) showed that at temperatures lower than the liquidus, approximately 1525°C, the predicted thermal cycles at all thickness positions converge rapidly, Figure 4-12. This behavior is consistent with the two dimensional heat flow conditions expected in laser welding of thin sheet. However, the calculated peak temperatures and thermal cycles at temperatures greater than 1525°C vary unreasonably with thickness position. This anomaly can be attributed to two of the simplifications made in the model. The latent heat of fusion was not considered, which would have lowered the peak temperature in the fusion zone in a roughly uniform manner. Also, weld pool convection was simulated only by an artificial increase in thermal conductivity [75,77], which most likely were too low to properly simulate laser welding processes. The crude approximation of weld pool convection adopted in this model gave rise to the unrealistically large gradient in FZCL peak temperatures (1950°-3550°C) calculated at different thickness positions by this model.

Despite the shortcomings evident in modeling the fusion zone weld thermal cycles, the model is still applicable in evaluating solid-state transformations. Heat flow in the thickness direction quickly equilibrates the calculated temperatures, obviating the effects of the weld pool convection assumption. Also, the magnitude of the latent heat of fusion effect is not appreciable after weld solidification, because the latent heat of fusion term that would have been added during the heating cycle would also have been subtracted at

the liquidus temperature. These are the reasons for the rapid weld thermal cycle convergence at all thickness positions at approximately 1525°C.

Because of these limitations in the model, the model is only considered valid in regions and times in which the model predicts temperatures of less than approximately 1500°C.

4.3 Weld Characterization

4.3.1 Microstructural Characterization

Light optical micrographs of the weld cross sections are compared in Figure 4-13. Grades of similar gages (e.g., grade 1 and grade 2, and grade 4 and grade 5) have similar sized fusion and heat affected zones. These similarities in weld geometry were expected because of the similarity in welding parameters, which were selected to produce full penetration welds.

Micrographs showing gradients in weld microstructures in grades 1 through 5 are shown at higher magnification in Figure 4-14 through Figure 4-18. Quantitative microscopy revealed how the volume fraction of microconstituents varied as a function of distance from the fusion zone centerline (FZCL), shown in Figure 4-19. Microhardness profiles are also plotted on these figures to demonstrate the gradient in mechanical properties.

The weld thermal cycle and steel composition determine the types and amounts of microconstituents, which in turn control the weld mechanical properties. Weld thermal

cycles were determined for each grade at varying distances from the FZCL, and are shown in Figure 4-20. Of particular interest is 1) the region where the greatest difference in mechanical properties from the base metal is observed, and 2) the width of the region having changed mechanical properties.

4.3.2 Peak Hardness in Welds

4.3.2.1 Fusion Zone Microstructure

The peak hardness was observed at the FZCL in all the welds in this study. At the FZCL, the thermal cycle is most extreme, with the highest peak temperature and most rapid cooling rate, Figure 4-20. These thermal conditions gave rise to the microstructures shown in Figure 4-21, which indicate that none of the grades have fully martensitic structures, despite the rapid cooling rates associated with the laser welding process. In grades 1, 2, and 3, ferrite (F), upper bainite (UB), and lower bainite/lath martensite (M) microconstituents are observed, while grades 4 and 5 are predominantly lath martensite (M) with ferrite allotriomorphs (AF) decorating the prior austenite grain boundaries. These constituents were identified using commonly accepted criteria[83,84]; however, lower bainite could not reliably be distinguished from lath martensite using LOM or SEM[83-85]. Bainitic and lath martensitic phases are therefore termed "martensite constituent" in Figure 4-19 for lack of more specific identification. The microstructure of lower bainite/lath martensite is shown at higher magnification in Figure 4-22.

microstructure of lower bainite/lath martensite is shown at higher magnification in Figure 4-22.

The low hardenabilities of these grades allow for the formation of diffusion controlled quench products, such as ferrite and bainite, even during the extremely rapid cooling rates associated with the laser weld thermal cycle. For many HSLA steels, fully martensitic structures are expected to form if the weldment cools from 800°C to 500°C in less than 5 seconds (e.g., if $t_{8/5}$ is less than 5 seconds).[86] However, the grades studied here have lower carbon contents (and concomitantly lower hardenabilities), so that even the rapid cooling rates associated with the laser welding thermal cycle—yielding $t_{8/5}$ of less than 0.5 seconds—are not sufficient to induce fully martensitic structures.

It follows logically that the hardness of the FZCL would depend on the hardness and amount of martensite constituent present. Before drawing any conclusions as to the factors that control fusion zone hardness, though, the possibility of martensite autotempering during the weld thermal cycle should be considered. Many researchers have reported autotempering in the arc welding of low alloy grades,[85-88] although no research has been published on autotempering in HSLA laser welds. Specifically, Grong and Akselsen et. al. have commented that the martensite hardness in arc welds is lower than the hardness of water-quenched martensite in HSLA steels, lower than 400 VPN (approximately 440 HK),[85,86] because of autotempering effects. For low alloy grades,

the softening effects of autotempering can be particularly significant because of the high martensite start [M_s] temperatures of these grades.

Regardless of the operative strengthening mechanisms, the FZCL was found to be the hardest region in each of the welds. For this reason, ABI testing was performed at the FZCL to provide detail of the "upper boundary" of weld mechanical properties.

4.3.2.2 Investigation of Martensite Autotempering

To determine whether martensite forming in the fusion zone of the welds underwent autotempering, fusion zone cooling rates and microhardness measurements were compared with the cooling rates and microhardness measurements in austenitized and brine-quenched samples of the same composition. Martensite microhardness data was also compared with microhardness data that from the literature, in which the martensite was shown not to be autotempered through transmission electron microscopy.

Comparison of the cooling rates indicated in Figure 4-23 and Table 4-5 suggest that, at temperatures above the M_s, quenching in iced brine roughly approximates the thermal cycles expected in the fusion zones of laser welds on thin sheet. However, this approximation degrades at lower temperatures, with the quenched samples cooling much faster at temperatures below the M_f than the fusion zones of the laser welds, as previously discussed. From this observation, the question of autotempering within the fusion zones of the laser welds becomes a possibility. Studies concerning the autotempering of laser

welds have not been published. However, it has been suggested that martensite autotempering occurs within HSLA arc welds,[85,87,88] where the cooling rates are considerably slower than in laser welds.

The microhardness of the fusion zone martensite and austenitized and quenched martensite is compared to published hardness data of martensite that did not undergo autotempering[89,90] in Figure 4-24. In all cases, the brine quenched and fusion zone martensite investigated in this study exhibited the same hardness within experimental error, indicating that the differences in laser weld and brine quench cooling rates below the M_s temperatures do not influence autotempering behavior in these grades. Moreover, the hardness of the martensite in grades 4 and 5 (bearing 0.090 and 0.085 wt% C, respectively) correlates closely with published results[89,90] in which transmission electron microscopy verified that no autotempering occurred. It is therefore concluded that no significant amount of autotempering occurred in grades 4 and 5, either in the laser welded or austenitized and brine quenched martensite.

The martensite in grades 1, 2, and 3 also exhibits nearly identical hardness values in the laser-welded and austenitized and quenched condition. In contrast to grades 4 and 5, however, autotempering occurs during the laser welding of these grades. The difference between the measured martensite hardness in grades 1, 2, and 3 and the interpolated hardness values of untempered martensite having the same carbon content is illustrated in Figure 4-24. The comparatively low martensite hardness values in grades 1, 2, and 3 are

attributed to the autotempering response of steels with low carbon contents. Because autotempering is a diffusion controlled process, tempering effects occur rapidly at high temperatures. Therefore, martensite forming at high temperatures (i.e., in materials with high M_s temperatures) is more prone to autotempering than martensite that forms at low temperatures.[91] This is the reason low alloy steels are generally susceptible to autotempering.

The difference in hardness attributed to autotempering was calculated by subtracting the measured martensite hardness (e.g., from the fusion zone samples or the brine quenched samples) from the estimated hardness value of martensite with the same carbon content that was not autotempered, which was determined by curves of least-squares fit from the data of Speich and Warlimont.[90] As discussed, the extent of autotempering increases with increasing M_s temperatures, Figure 4-25. Comparison of grade 2 with grade 4 shows that an increase in M_s temperature of only 40°C can cause an autotempering-related decrease in martensite hardness of more than 50 HK_{25}.

The data presented in Figure 4-25 provides strong evidence for an empirical correlation between the autotemper softening response and the nominal M_s temperature in processes with rapid cooling rates, such as laser welding and brine quenching. Understanding the M_s temperature is of significant importance when assessing processing-microstructure-property relationships in low alloy laser welds. Grades with calculated M_s temperatures greater than approximately 465°C will autotemper significantly, which may have

important implications on the weld mechanical properties in these grades. Grades with nominal M_s temperatures below 450°C are not expected to undergo measurable autotempering, and therefore weld mechanical properties may be more appropriately related to the amount and morphology of microconstituents, not autotempering effects.

Interpretation of the Softening Response-Calculated M_s Temperature Trend

Figure 4-25, does not necessarily imply that the softening response occurs because of the high temperature autotempering phenomenon (i.e., near the calculated M_s temperature). The physical meaning of the autotemper softening response and the calculated M_s temperature should be considered carefully. The magnitude of the softening response is assumed to be influenced only by autotempering effects. However, to avoid the influence of softer non-martensitic phases during microhardness testing, only the highest microhardness measurements were used in calculating the softening response. This methodology introduced a bias in the data. Within each sample, the first martensite to form (which formed at the highest temperature) should undergo the greatest amount of autotempering. Hardness data from the first martensite that formed is therefore less likely to be reported than data from the last martensite to form. For this reason, the reported martensite hardness values are probably more representative of martensite that formed near the M_f temperature, and it is likely that softer martensite is present in the samples. The softening response reported in Figure 4-25 is therefore a conservative estimate of the effects of autotempering.

The phenomenology of autotempering also needs to be elucidated. It has already been established that the cooling rate and the M_s temperature generally influence the extent of autotempering.[91] Both of these factors need to be examined within the context of this investigation. A broad range of cooling rates has been examined in this study, Table 4-5. It is expected that slow cooling rates promote autotempering by increasing time at elevated temperatures, which favors diffusion. However, cooling rate effects on autotempering were insignificant in the range of thermal conditions investigated in this study. The nearly identical hardness values of fusion zone martensite and austenitized and brine quenched martensite despite cooling rate differences demonstrates this point. Also, the grades with the lowest M_s temperatures, grades 4 and 5, did not autotemper measurably, even though they cooled more slowly during brine-quenching than the grades with high M_s temperatures, grades 1, 2, and 3, which did autotemper. This suggests that the M_s temperature and not cooling rate is the best parameter with which to correlate autotempering response.

Although calculated M_s temperatures were used effectively to describe the empirical observations in this study, they are certainly not absolute. The standard deviation in the calculated M_s temperatures, approximately 20-25°C, is shown in Table 4-4. Other sources of error may also be significant. Besides chemical composition, M_s temperatures depend upon metallurgical conditions such as the presence of other (non-austenitic) phases and austenite grain size as well as processing variables such as cooling rate.

For martensite formation to actually begin at the calculated M_s temperature, it is necessary for the structure to be fully austenitic at the calculated M_s, i.e., the formation of diffusion-controlled phases, particularly ferrite, must be avoided for martensite to begin forming at the calculated M_s temperature. The formation of other phases typically leads to rejection of carbon and other alloying elements into the austenite, and the actual M_s temperature decreases as a result of the enrichment in austenite composition. None of the fusion zones in this study are fully martensitic, which means that some diffusion-controlled transformation product (ferrite and upper bainite) formed prior to the austenite-martensite transformation. It follows that the calculated M_s temperatures in Table 4-4 are higher than the actual temperature at which martensite started to form. The brine quenched samples (shown in Figure 4-26) had greater martensite volume percentages than their fusion zone counterparts, so this effect is not as significant for the brine quenched samples.

The effects of austenite grain size and cooling rate on M_s temperature are expected to be negligible compared to the effects of composition and second phase formation. Austenite grain size could affect the M_s temperature by influencing the density of nucleation sites. Decreasing austenite grain size would provide for more martensite nucleation sites and concomitantly higher M_s temperatures. Small austenite grain sizes also provide more nucleation sites for diffusion controlled microconstituents, though, and if the cooling rate is not rapid enough to prevent these diffusional transformations, the effective M_s temperature could decrease as a result of the formation of these second phases. In the

laser welded martensite, the austenite grains in each grade form via a similar mechanism from the molten fusion zone, so no major difference in austenite grain size is expected. The relative effect of cooling rate on M_s temperature is also expected to be insignificant compared to the effects of composition and second phase formation. The fusion zone and brine quenched cooling rates in the A_3-M_s temperature range are comparable to each other, Table 4-5.

The empirical nature of the trends drawn in Figure 4-25 has been reinforced by this discussion. The nominal M_s temperature does not lend direct physical meaning to the autotempering process, because no martensite has formed at the calculated M_s temperature. However, the M_s acts as an indicator of the extent of autotempering that occurs during laser welding processes. Similarly, the softening response does not completely capture the range of autotempering behavior that occurs in laser welds, but serves as a reasonable basis to compare autotempering effects in grades with a range of M_s temperatures.

Figure 4-27 summarizes the discussion of peak hardness in the fusion zone. The hardness of the fusion zone increases with carbon content for three reasons. By increasing carbon content, 1) the grade becomes more hardenable, increasing the amount of martensite that forms, 2) solid solution strengthening becomes more effective, increasing the hardness of the martensite phase as it forms, and 3) the M_s temperature is decreased, diminishing the extent of softening by martensite autotempering.

4.3.3 Width of Fusion and Heat Affected Zones

At distances away from the FZCL, the cooling rate of the weld thermal cycle becomes less severe, allowing less martensite to form, resulting in decreasing hardness as a function of distance from the FZCL, Figure 4-20. The extent of the hardness decrease depends heavily upon carbon content, with the high carbon steels (grades 4 and 5) exhibiting greater decreases in hardness than grades 1 and 3, which in turn exhibited greater hardness decreases than grade 2, which had the lowest carbon content. This mechanism explains the hardness profile in the fusion zone and much of the supercritical heat affected zone in all grades.

In the region of the heat affected zone where no martensite has formed, the hardness is governed by the presence of other microconstituents. In the high carbon grades (grades 4 and 5), fine grained (~ 1 μm) ferrite formed, Figure 4-17d. This phase was believed to form from the austenite by a massive transformation. The massive transformation is a civilian phase transformation in which only short range diffusion occurs. Therefore massive transformations generally require rapid cooling rates, slightly less severe than required for martensitic transformation, but rapid enough to prevent long range diffusion from occurring, thereby ensuring the massive ferrite phase has the same composition as the parent austenite phase. Although no experimental work has been performed to verify

distance of 600 μm from the FZCL, the steel is significantly harder than the base metal. The high hardness in the absence of martensite is attributed to the extremely small grain size and high dislocation density of the massive ferrite phase.

A local hardness peak was measured in grades 1, 2, and 3 in the heat affected zone. The reason for these peaks was not evident from the light optical microscopy characterization results; they did not coincide with a localized decrease in grain size or maximum of any particular microconstituent (e.g., pearlite). One possibility is that the weld thermal cycle at those positions is allows for precipitation strengthening by microalloy precipitates, which are likely less than 60 nm in diameter (the maximum precipitate size reported in the heat affected zones of arc welds on various microalloyed grades[94-96]) and would therefore not be observed by LOM or SEM.

The grain size measurements in Figure 4-19a,b,e indicate the existence of very narrow coarse-grained heat affected zones (CGHAZ) immediately adjacent to the fusion line. The small size of the CGHAZ and the limited grain growth observed in the CGHAZ are again attributed to the severe thermal gradient and limited time at elevated temperature that occurs in laser welds. Notably, the CGHAZ in the welds investigated remain harder than the base metal.

4.3.4 Automatic Ball Indentation Testing

Automatic ball indentation (ABI) was deemed a practical means to determine mechanical properties from small volumes of material, such as the fusion zones (as narrow as 650 μm) in this study. By performing ABI in the hardest and softest regions—the FZCL and the base metal—upper and lower bounds of weld mechanical properties were established. Also, the ABI base metal results allowed for direct comparison of ABI technique to more commonplace methods (standardized tensile tests). The FZCL strain hardening behavior and the gradient in strength levels observed from the FZCL to the base metal were of particular interest.

The ABI true stress-true plastic strain curves in the base metal and at the FZCL are plotted in Figure 4-28 alongside representative ASTM E8 tensile plots. Consideration of Figure 4-28 suggests validity to the ABI technique. Reasonable agreement exists between the ABI base metal results and standard tensile data, and the ABI fusion zone properties show increases in strength that were anticipated from the microhardness profiles. One exception to this statement is the grade 3 ABI base metal results, which shows a decrease in true strength after about 8% true plastic strain, which is physically unrealistic. The error is likely a result of the grade 3 geometry: the sheet was too thin to allow for the uninhibited development of the plastic zone beneath the indentation.

The strain hardening index, n, was determined in the base metal and the fusion zone by fitting the ABI data to the power law hardening described by Hollomon[97]

$$\sigma=K\varepsilon^{n} \qquad (4\text{-}1)$$

where true stress, σ, is expressed in terms of the strength coefficient, K, the true strain, ε, and the strain hardening exponent, n. The first data point in each case (corresponding to a true plastic strain ~0.002) was discounted so the ABI strain-hardening index was evaluated over the same strain range as the strain-hardening index was evaluated over the same strain range as the standardized tensile test, in which the yield point elongation regime was not considered in determining the strain hardening exponent.

Comparison of the base metal and fusion zone yield strengths, tensile strengths, and strain hardening values is shown in Figure 4-29. Again, reasonable agreement exists between the base metal tensile test and ABI results, which further emphasizes the validity of the ABI technique. Increases in fusion zone strength parallel the measured increases in fusion zone hardness, and decreases in strain-hardening capacity are observed in all grades. In this respect, the findings of this study are similar to other investigations of weld mechanical properties[98-100]. Despite the diminished fusion zone strain hardening values, reasonable ductility exists in the fusion zones of all grades, as evidenced by the strain-hardening values, which range from 0.10 to 0.14.

The fusion zone mechanical properties are predominantly dependent upon carbon content, Figure 4-30. The higher the carbon content in the steel, the higher the strength

levels in the fusion zone, as previously discussed regarding hardness(Figure 4-27). This result is consistent with published work investigating the effect of martensite content on tensile properties in dual phase (ferrite-martensite) steels[45,50,51]: yield strength and ultimate tensile strength increase with martensite volume fraction.

Studies of ferrite-martensite steels have also shown that increasing martensite volume fraction gives rise to improved strain hardening capacity, as measured either through higher $d\sigma/d\varepsilon$ values[50] or lower yield strength/tensile strength ratios[51]. Figure 4-30 indicates that the opposite trend—decreasing strain hardening exponents with increasing martensite volume fraction—occurred in the fusion zones investigated in this study. This seeming discrepancy is most likely the result of two microstructural differences. First, the martensite content in the fusion zones was significantly higher (54-95 volume percent) than the studies cited, none of which examined grades that were more than 55 volume percent martensite. Also, significant morphological differences exist between the evenly dispersed polygonal ferrite-martensite grades evaluated by Jiang[50] and Chang[51] and the solidification structure of the laser welds in question. The polygonal martensite resided in a continuous matrix of ferrite in the cited studies, whereas no continuous ferrite phase was established by the allotriomorphic and polygonal ferrite within the fusion zone microstructure, even in the grade 2, which was comprised of only 54% martensite. The high strain hardening values associated with multiphase (ferrite-martensite) steels was not achieved in the steels with carbon contents between 0.042wt% and 0.090wt% under the welding conditions in this study.

4.4 Suggestions for Alloy Development

The impetus for this research lies in the determination of laser weld mechanical properties, which are known to decrease the formability of laser welded blanks. In some instances, low weld ductility is specifically cited as the formability-limiting parameter[1], i.e., when the weld is less ductile than the base metal. For every grade in this study, the weld was less ductile than the base metal.

Factors that control base metal and fusion zone ductility were identified in this study. Weld ductility (measured by strain hardening exponent) decreases as martensite content increases, which in turn increases with carbon content. The weld thermal cycle may also affect the amount of martensite formed, but in the range of welding parameters and gages [typical of laser welding processes] investigated here, it seems likely that carbon content is by far the more dominant factor in determining martensite content and therefore fusion zone ductility.

The strain hardening capability of the base metal is correlated strongly with microalloy precipitate content: the greater the precipitate content, the lower the n value. Of course, this statement is not strictly true for all materials, but it was applicable in the fine-grained microalloyed ferrite-pearlite grades in this study, which presumably had similar precipitate sizes and distributions, as discussed earlier.

The factors influencing weld and base metal ductility have already been discussed and illustrated in Figure 4-30 and Figure 4-11, respectively, but are juxtaposed in Figure 4-31 for ease of comparison. Automakers interested in using high strength steels that do not experience significant formability decreases in the laser welded condition (as a result of poor weld ductility) may be advised to use a steel that derives its strength from high microalloy precipitate content (i.e., precipitation hardening) with as low a carbon content as possible. For example, Figure 4-31 suggests that it may be possible to produce a grade with a carbon content of 0.04wt% and a microalloy content of 0.100wt%, in which the base metal and the fusion zone are predicted to have nearly identical strain hardening values (approximately 0.15).

Of course, this assessment is tenuous, based upon the limited composition ranges investigated in this study. Additional metallurgical or production complications may arise if this strategy is used to increase the weld ductility of high strength precipitation strengthened steels.

Table 4-1. Summary of quantitative light microscopy characterization of as-rolled materials.

Grade	Ferrite Grain Size[1] (μm)	Second Phase Volume Percent[2] (%)
1	5.7+/- 0.8	5.9+/-1.8
2	3.7+/-0.3	1.1+/-0.7
3	5.3+/-0.5	1.3+/-0.8
4	NA	7.5+/-1.5
5	3.1+/- 0.1	7.2+/-1.9

[1] Measurements taken from longitudinal section

[2] Measurements taken from planar section

Table 4-2. Calculated equilibrium microalloy precipitate wt%. Assumed precipitation sequences are noted below.

		NbN (wt%)	NbC (wt%)	VN (wt%)	VC (wt%)	Total Precipitate (wt%)
Grade 1	Min[1]	0.000	0.006	0.030	0.006	0.041
	Max[2]	0.006	0.000	0.034	0.008	0.048
Grade 2	Min[3]	0.033	0.028	0.001	0.000	0.062
	Max[4]	0.062	0.000	0.001	0.000	0.063
Grade 3	Min[1]	0.000	0.007	0.042	0.027	0.075
	Max[2]	0.007	0.000	0.038	0.030	0.075
Grade 4	Min[5]	0.000	0.005	0.032	0.000	0.036
	Max[6]	0.005	0.000	0.029	0.002	0.036
Grade 5	Min[1]	0.000	0.007	0.033	0.063	0.102
	Max[2]	0.007	0.000	0.028	0.067	0.102

[1] VN (austenite) – VN (ferrite) – NbC (ferrite) – NbN (ferrite) – V_4C_3 (ferrite)

[2] VN (austenite) – NbN (ferrite) – VN (ferrite) – NbC (ferrite) - V_4C_3 (ferrite)

[3] NbN (to 1000°C) – NbC (ferrite) – NbN(austenite) – VN(ferrite) - V_4C_3 (ferrite)

[4] NbN (austenite) – NbN (ferrite) – NbC (ferrite) – VN (ferrite) - V_4C_3 (ferrite)

[5] VN (ferrite) – NbC (ferrite) – NbN (ferrite) – V_4C_3 (ferrite)

[6] NbN (ferrite) – VN (ferrite) – NbC (ferrite) - V_4C_3 (ferrite)

Table 4-3. Summary of tensile test results for as-rolled materials.

Grade	θ[1]	k[2] (MPa)	n[2]	YS[3] (MPa)	UTS[4] (MPa)	UTE[5] (%)	YPE[6] (%)	UE[7] (%)	Etot[8] (%)	YS/TS	r_θ
1	0°	619.2	0.179	357.2	440.6	16.0	2.6	13.0	25.2	0.81	0.75
1	45°	613.0	0.182	369.6	439.9	17.9	3.5	14.1	27.8	0.84	0.93
1	90°	587.5	0.175	357.9	435.8	17.0	2.9	15.2	26.6	0.82	0.86
1	**Mean[9]**	**606.5**	**0.178**	**361.5**	**438.8**	**17.0**	**3.0**	**14.1**	**26.5**	**0.82**	**0.87**
2	0°	593.0	0.169	394.4	446.8	15.7	4.9	10.5	23.2	0.88	0.84
2	45°	579.2	0.169	403.4	448.2	16.8	5.5	11.2	26.6	0.90	1.06
2	90°	577.1	0.165	406.8	446.8	16.7	5.6	10.9	25.4	0.91	0.86
2	**Mean[9]**	**583.1**	**0.168**	**401.5**	**447.3**	**16.4**	**5.3**	**10.9**	**25.1**	**0.90**	**0.95**
3	0°	664.7	0.154	444.0	499.9	14.2	3.9	10.0	22.4	0.89	0.85
3	45°	662.6	0.147	447.5	503.3	14.0	3.8	9.8	22.0	0.89	1.04
3	90°	655.0	0.147	447.5	501.3	13.0	4.2	9.0	20.4	0.89	0.80
3	**Mean[9]**	**660.8**	**0.149**	**446.3**	**501.5**	**13.7**	**4.0**	**9.6**	**21.6**	**0.89**	**0.93**
4	0°	707.4	0.127	384.7	496.4	13.1	0.0	13.2	24.0	0.78	1.04
4	45°	678.5	0.124	375.8	475.8	14.8	0.0	14.6	24.9	0.79	1.28
4	90°	685.4	0.119	391.6	486.1	13.7	0.0	13.3	22.3	0.81	1.10
4	**Mean[9]**	**690.4**	**0.124**	**384.1**	**486.1**	**13.9**	**0.0**	**13.7**	**23.7**	**0.79**	**1.17**
5	0°	831.5	0.145	495.1	595.7	13.9	1.7	10.5	22.7	0.83	0.82
5	45°	809.5	0.146	494.4	588.1	13.2	1.7	10.9	22.4	0.84	1.08
5	90°	839.1	0.15	507.5	608.1	13.9	1.9	11.5	22.3	0.83	0.85
5	**Mean[9]**	**826.7**	**0.147**	**499.0**	**597.3**	**13.7**	**1.8**	**11.0**	**22.5**	**0.84**	**0.96**

[1] Orientation with respect to the rolling direction

[2] As defined by (2-1): $\sigma=k\varepsilon^n$. For discontinuously yielding grades, n was calculated in the region of uniform (continuous) yielding

[3] 0.2% Offset Yield Strength. Although grades 1, 2, 3, and 5 yielded discontinuously, the differences between upper yield strength and lower yield strength were negligible.

[4] Ultimate Tensile Strength

[5] Ultimate Tensile Elongation

[6] Yield Point Elongation

[7] Uniform Elongation, defined here as the amount of continuous (non YPE) elongation prior to the onset of necking.

[8] Total elongation to failure

[9] Arithmetic mean of 0°, 45°, and 90° orientations, except for r_m: $r_m = \frac{r_0 + 2r_{45} + r_{90}}{4}$

Table 4-4. M_s and M_f temperatures calculated using published equations.

M_s Temperature (°C)	Grade 1	Grade 2	Grade 3	Grade 4	Grade 5
Payson & Savage[101]	453	474	456	435	421
Carapella[102]	441	467	444	421	402
Rowland & Lyle[103]	452	473	455	434	420
Grange & Stewart[104]	484	509	488	465	451
Nehrenberg[105]	454	475	457	437	422
Steven & Haynes[106]	503	529	508	482	469
Andrews (linear)[107]	487	510	491	468	456
Andrews (product)[107]	478	492	484	466	464
Average	469	491	473	451	438
Standard Deviation	22	23	23	22	25

M_f Temperature (°C)	Grade 1	Grade 2	Grade 3	Grade 4	Grade 5
Steven & Haynes[106]	288	314	293	267	256

Table 4-5. Calculated cooling rates (A_3-M_s), (M_s-M_f), and (M_f-150°C) during laser welding and quenching in iced brine.

	Cooling Rate (°C/s) A_3 to M_s		M_s (°C)	Cooling Rate (°C/s), M_s to M_f		M_f(°C)	Cooling Rate (°C/s), M_f to 150°C	
Grade	FZCL	Brine Quenched		FZCL	Brine Quenched		FZCL	Brine Quenched
1	726	644	469	162	1097	288	22	777
2	790	635	491	199	907	314	24	860
3	826	1098	473	208	1245	293	32	864
4	1602	962	451	253	394	267	44	377
5	1504	946	438	216	390	256	42	362

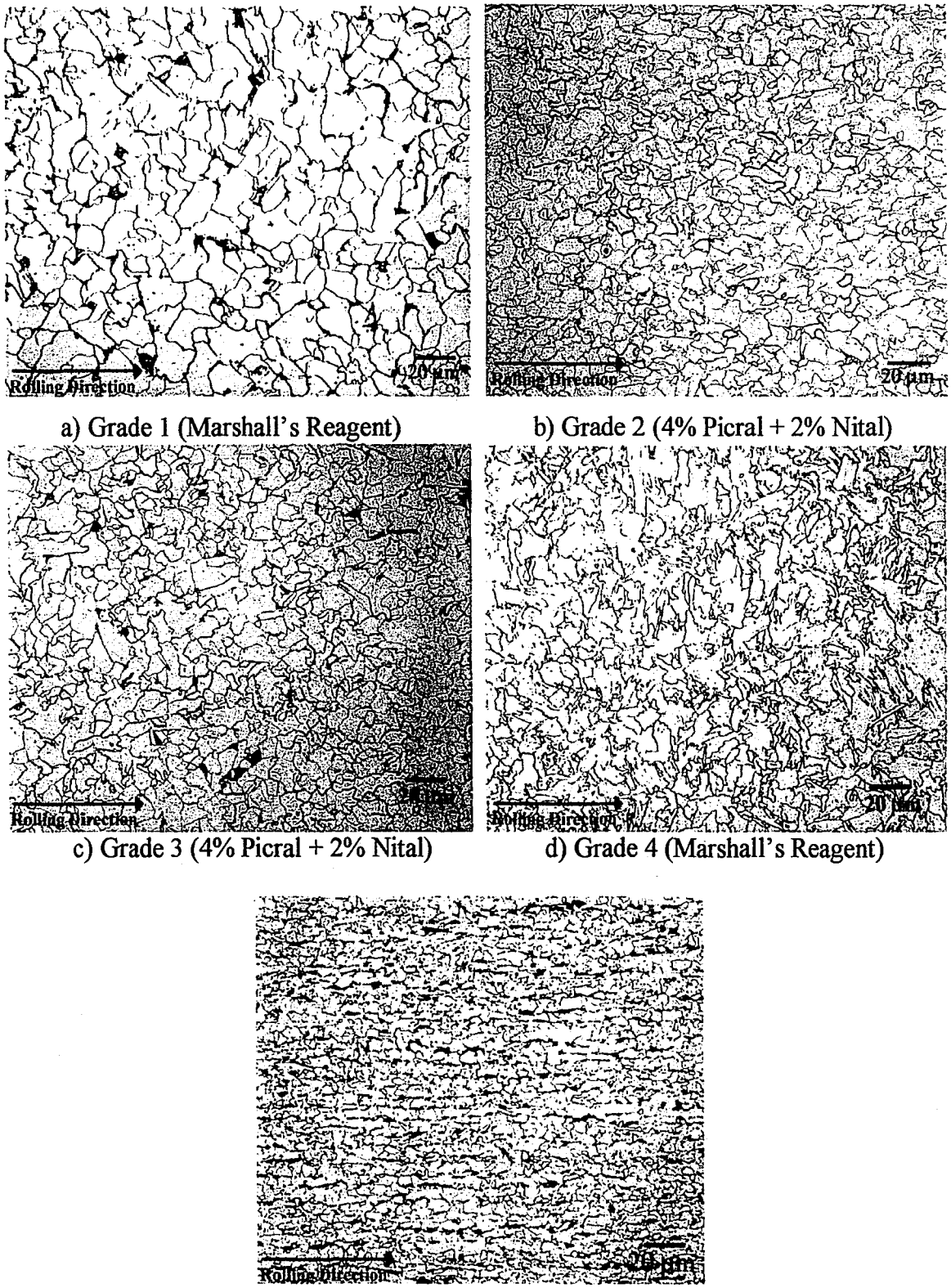

a) Grade 1 (Marshall's Reagent)

b) Grade 2 (4% Picral + 2% Nital)

c) Grade 3 (4% Picral + 2% Nital)

d) Grade 4 (Marshall's Reagent)

e) Grade 5 (4% Picral + 2% Nital)

Figure 4-1. Representative light optical micrographs of the as-rolled grades.

a) Grade 1 (Marshall's Reagent)

b) Grade 2 (4% Picral + 2% Nital)

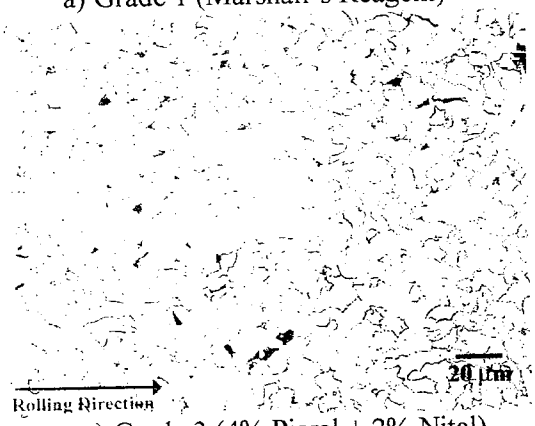

c) Grade 3 (4% Picral + 2% Nital)

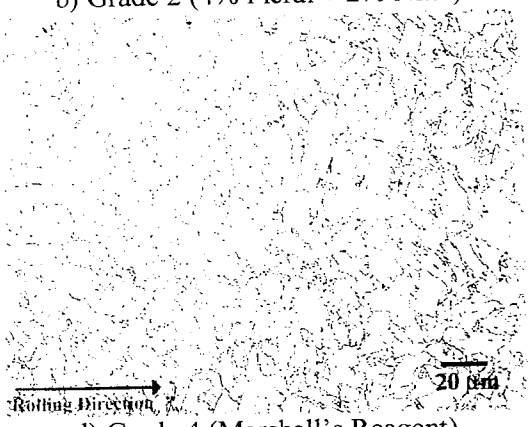

d) Grade 4 (Marshall's Reagent)

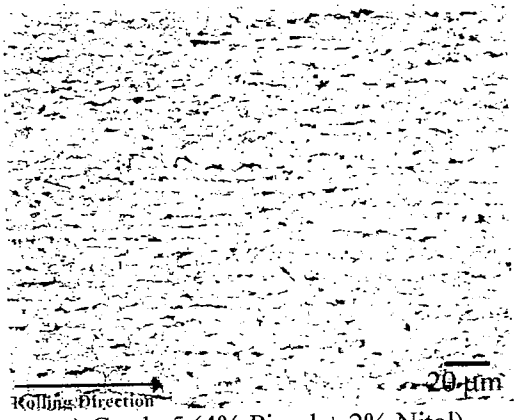

e) Grade 5 (4% Picral + 2% Nital)

Figure 4-1. Representative light optical micrographs of the as-rolled grades.

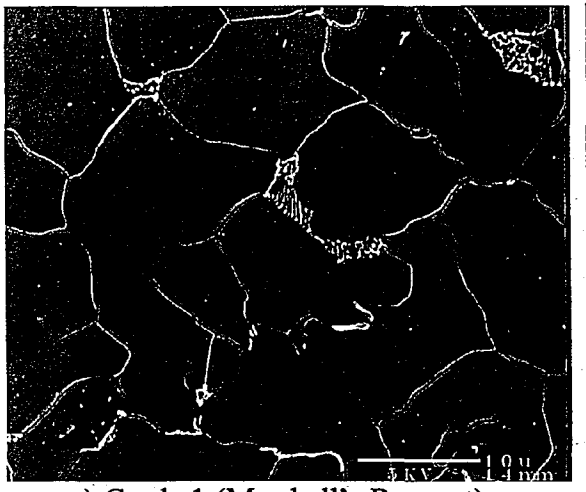

a) Grade 1 (Marshall's Reagent)

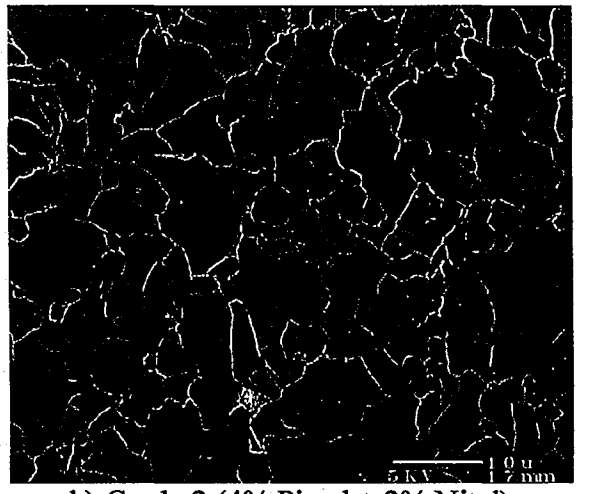

b) Grade 2 (4% Picral + 2% Nital)

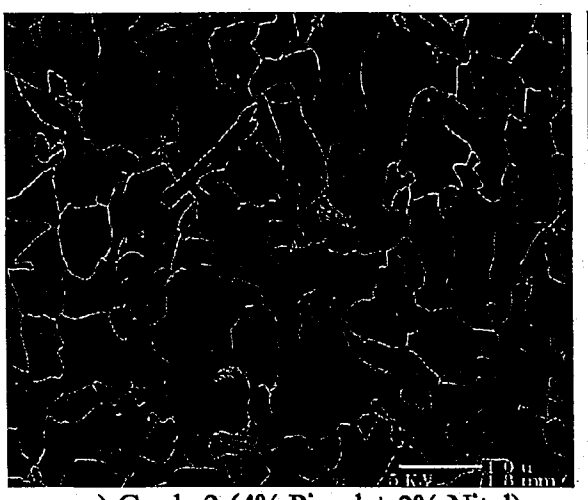

c) Grade 3 (4% Picral + 2% Nital)

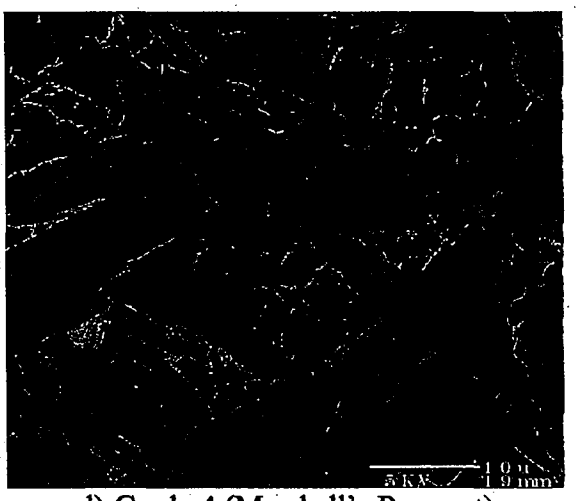

d) Grade 4 (Marshall's Reagent)

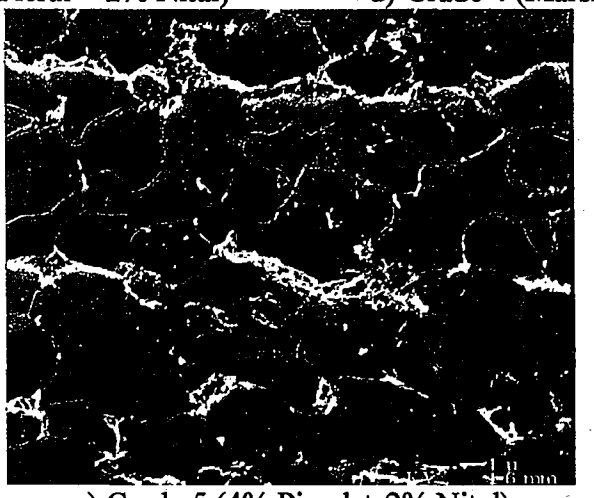

e) Grade 5 (4% Picral + 2% Nital)

Figure 4-2. SEM images of the as-rolled grades.

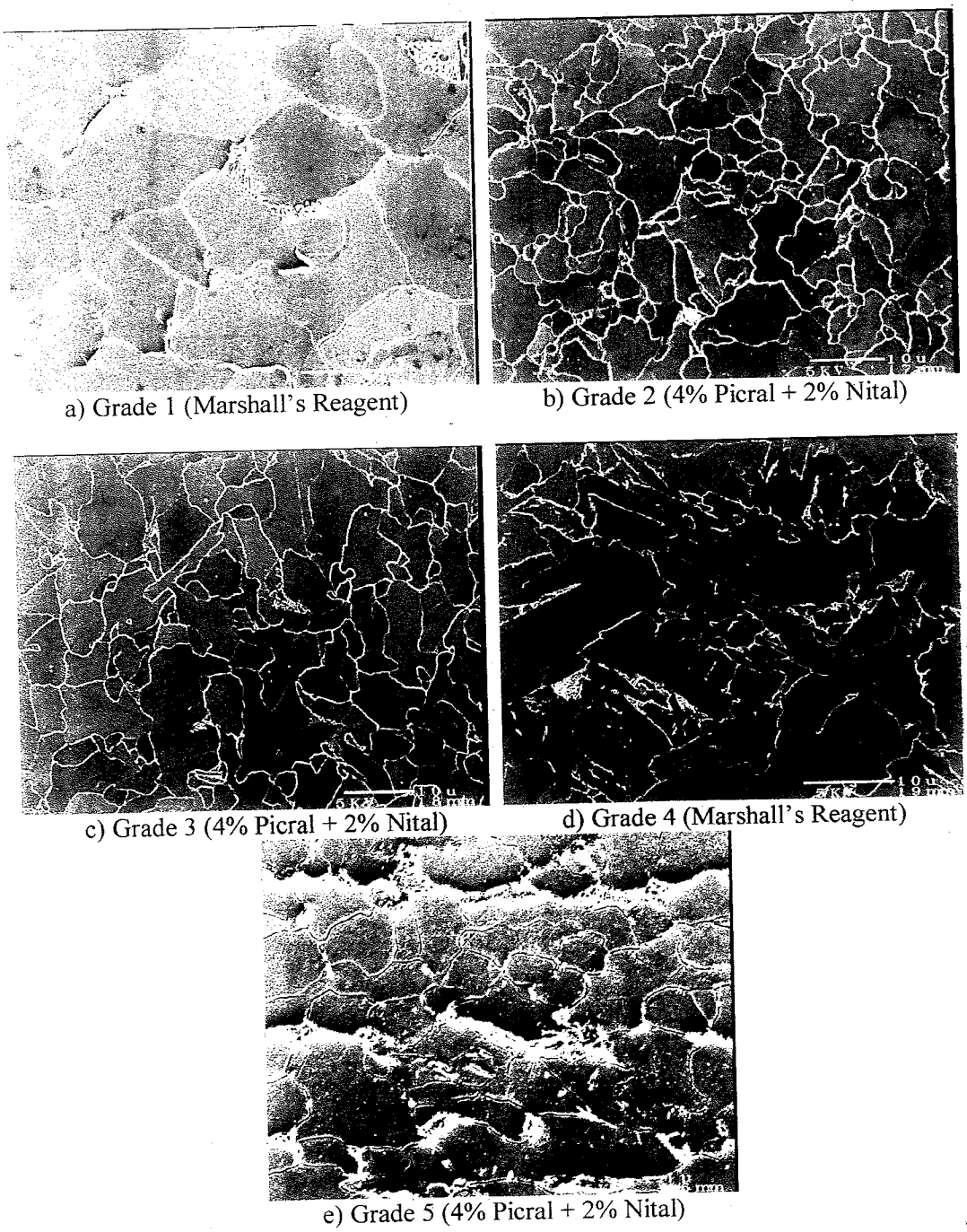

a) Grade 1 (Marshall's Reagent)

b) Grade 2 (4% Picral + 2% Nital)

c) Grade 3 (4% Picral + 2% Nital)

d) Grade 4 (Marshall's Reagent)

e) Grade 5 (4% Picral + 2% Nital)

Figure 4-2. SEM images of the as-rolled grades.

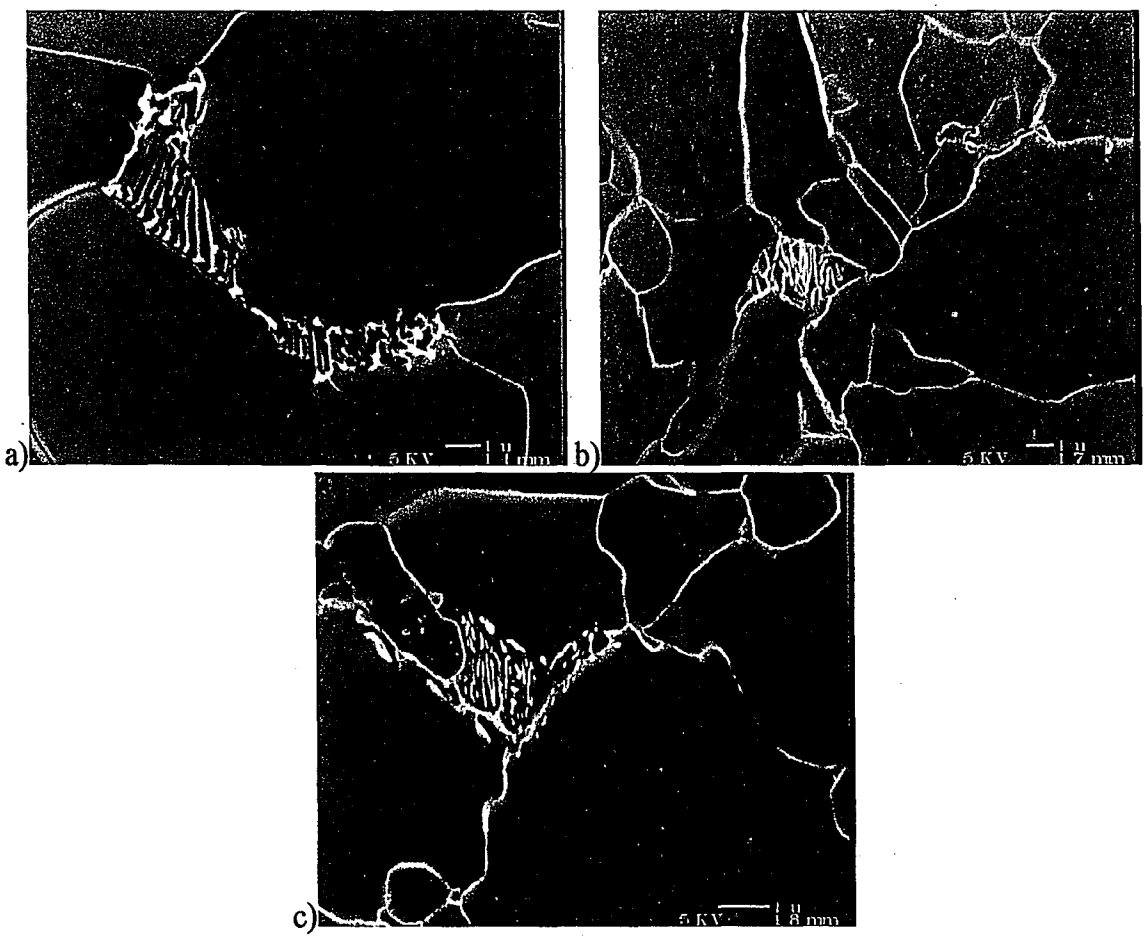

Figure 4-3. SEM images showing pearlite in as-rolled materials. a) grade 1, b) grade 2, c) grade 3.

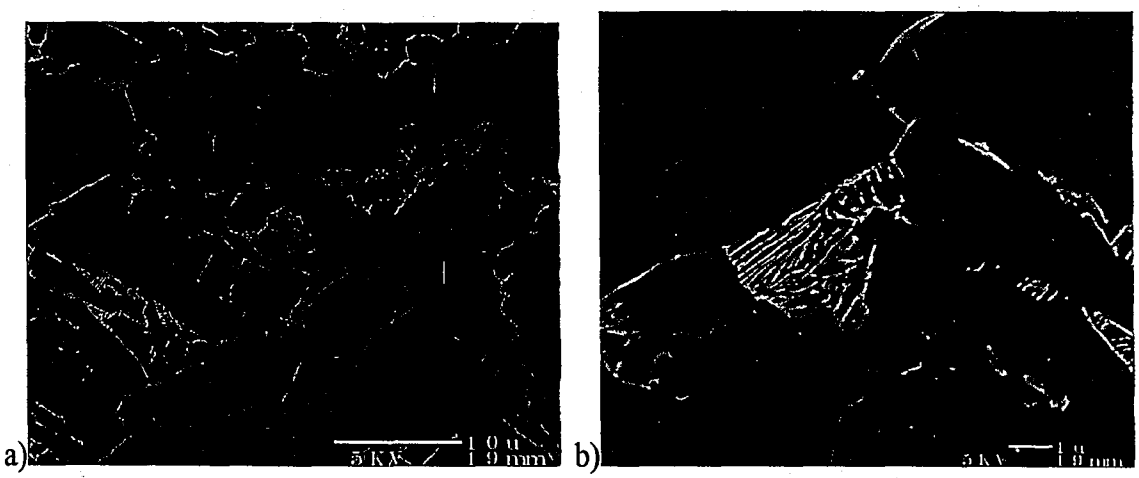

Figure 4-4. SEM images showing the a) bainitic and b) pearlitic nature of grade 4.

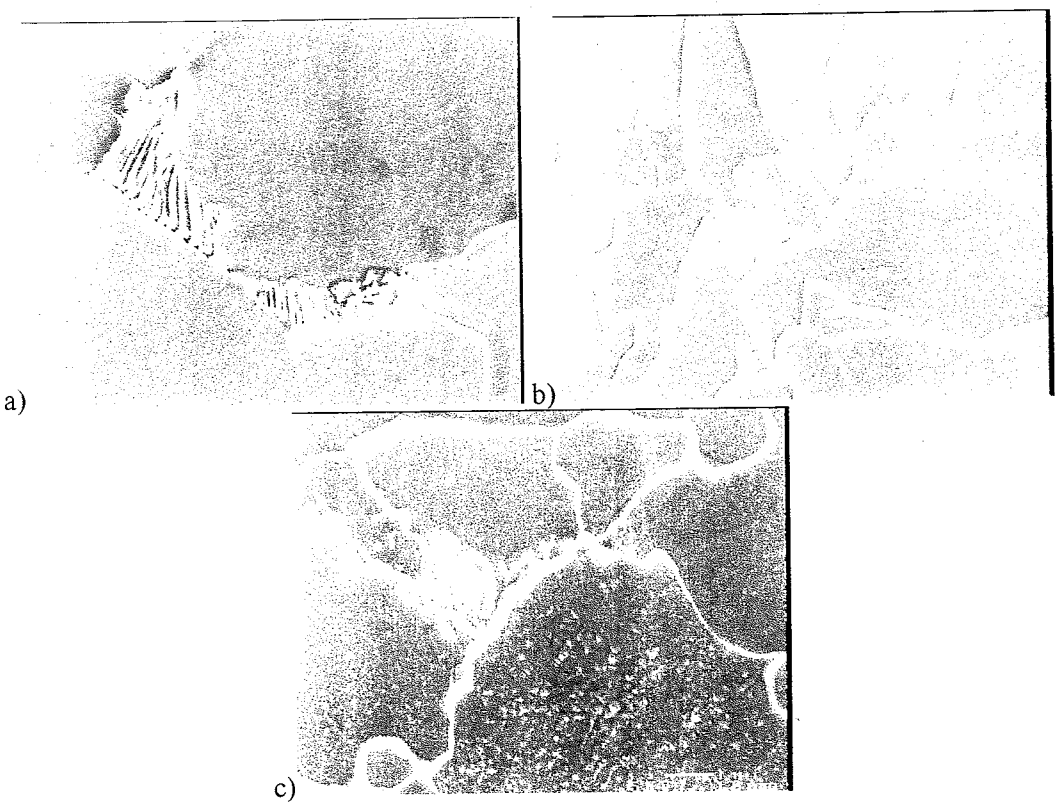

Figure 4-3. SEM images showing pearlite in as-rolled materials. a) grade 1, b) grade 2, c) grade 3.

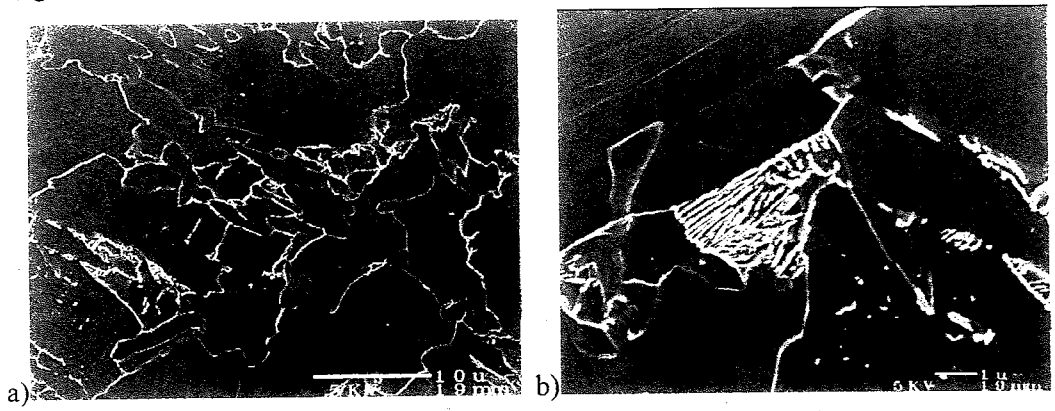

Figure 4-4. SEM images showing the a) bainitic and b) pearlitic nature of grade 4.

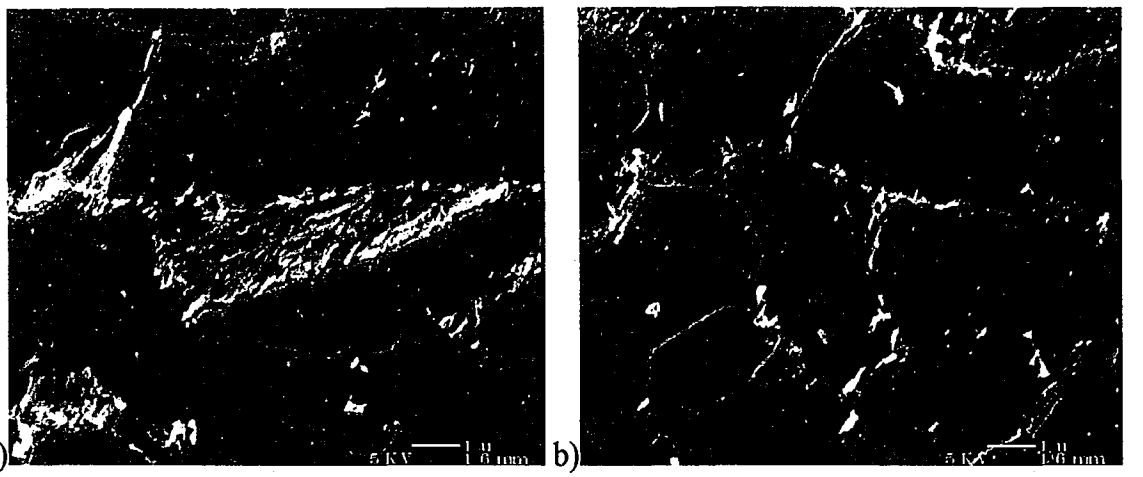

Figure 4-5. SEM micrographs of as-rolled Grade 5, showing the size range of the second phase(s) observed. a) Large (greater than 1μm) phase and b) submicron precipitates, forming preferentially on ferrite grain boundaries. 4 % picral + 2% nital.

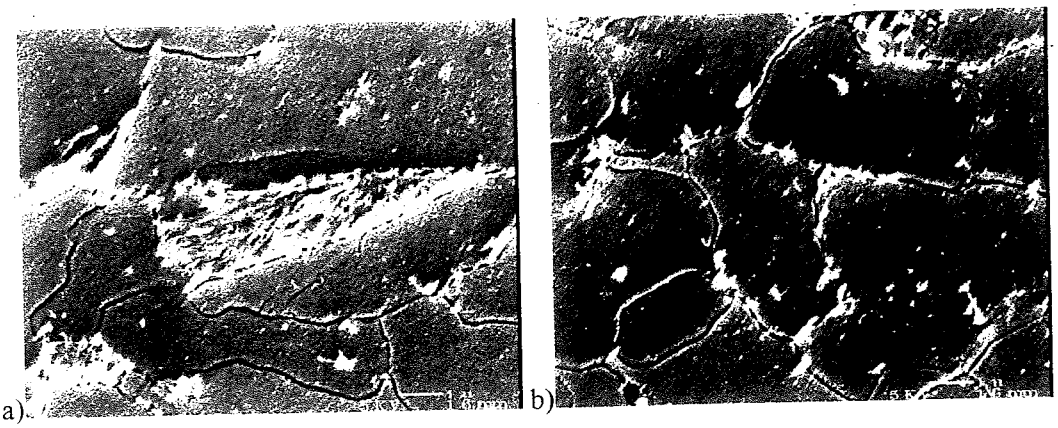

Figure 4-5. SEM micrographs of as-rolled Grade 5, showing the size range of the second phase(s) observed. a) Large (greater than 1μm) phase and b) submicron precipitates, forming preferentially on ferrite grain boundaries. 4 % picral + 2% nital.

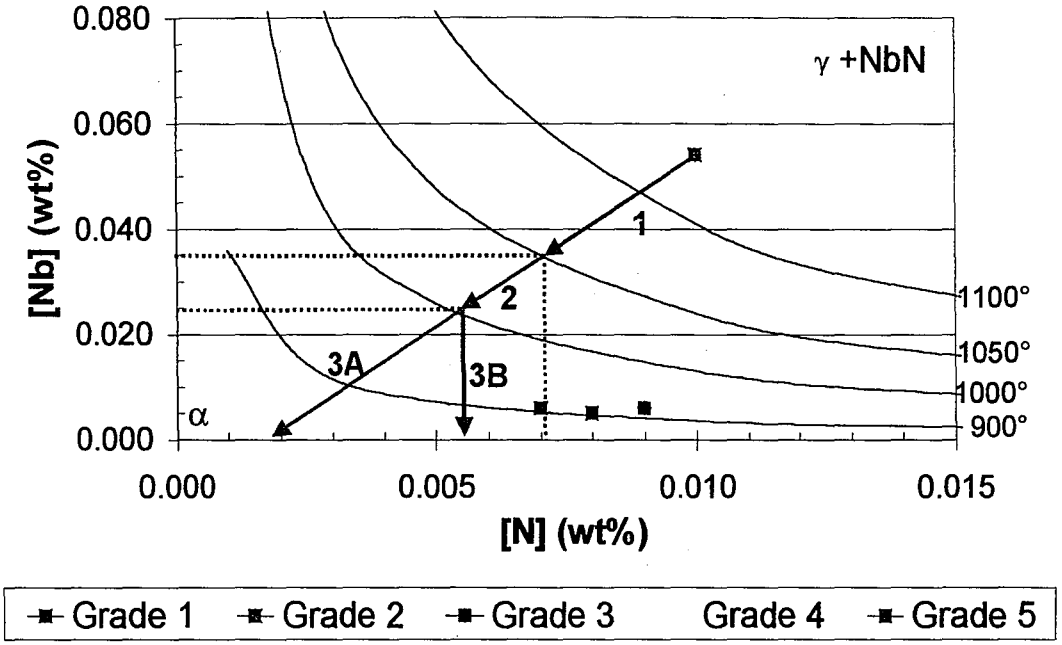

Figure 4-6. Solubility diagram of NbN in austenite. In grades 1, 3, 4, and 5, negligible NbN precipitation is expected within austenite. The effect of uninterrupted NbN precipitation on the austenite composition is considered for grade 2 in the (1-2-3A) sequence. The effect of NbN precipitation followed by NbC precipitation at 1000°C is considered in the (1-2-3B) sequence.

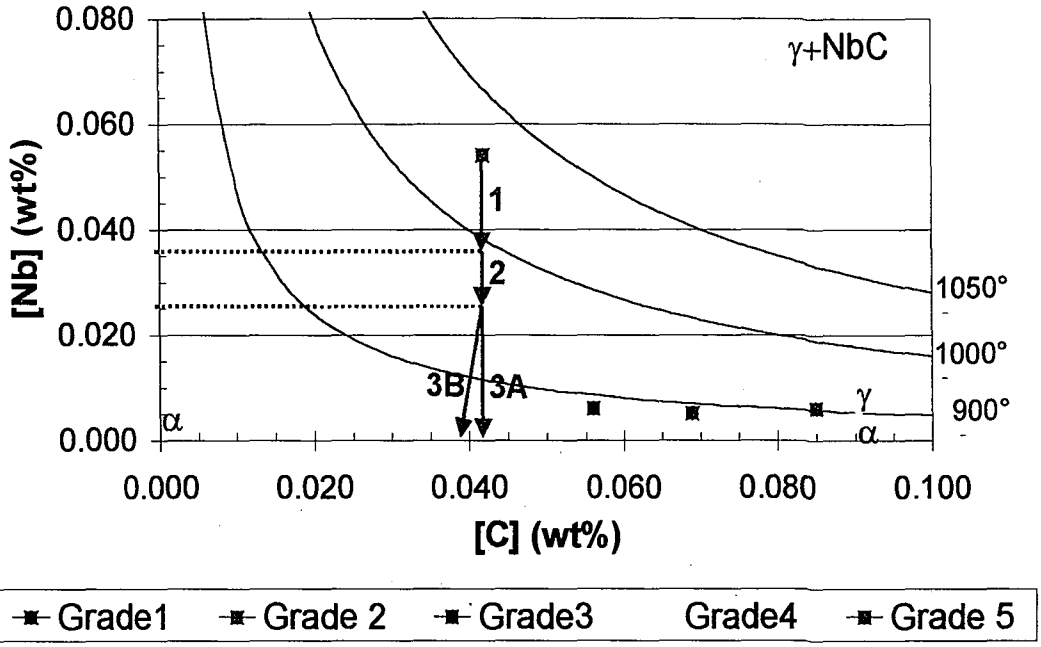

Figure 4-7. Solubility diagram of NbC in austenite. In grades 1, 3, 4, and 5, NbC precipitation in austenite is not expected. For grade 2, the (1-2-3A) sequence demonstrates the effect of uninterrupted NbN precipitation on austenite composition, whereas the (1-2-3B) sequence shows the effect of NbN precipitation at temperatures greater than 1000°C, followed exclusively by NbC precipitation.

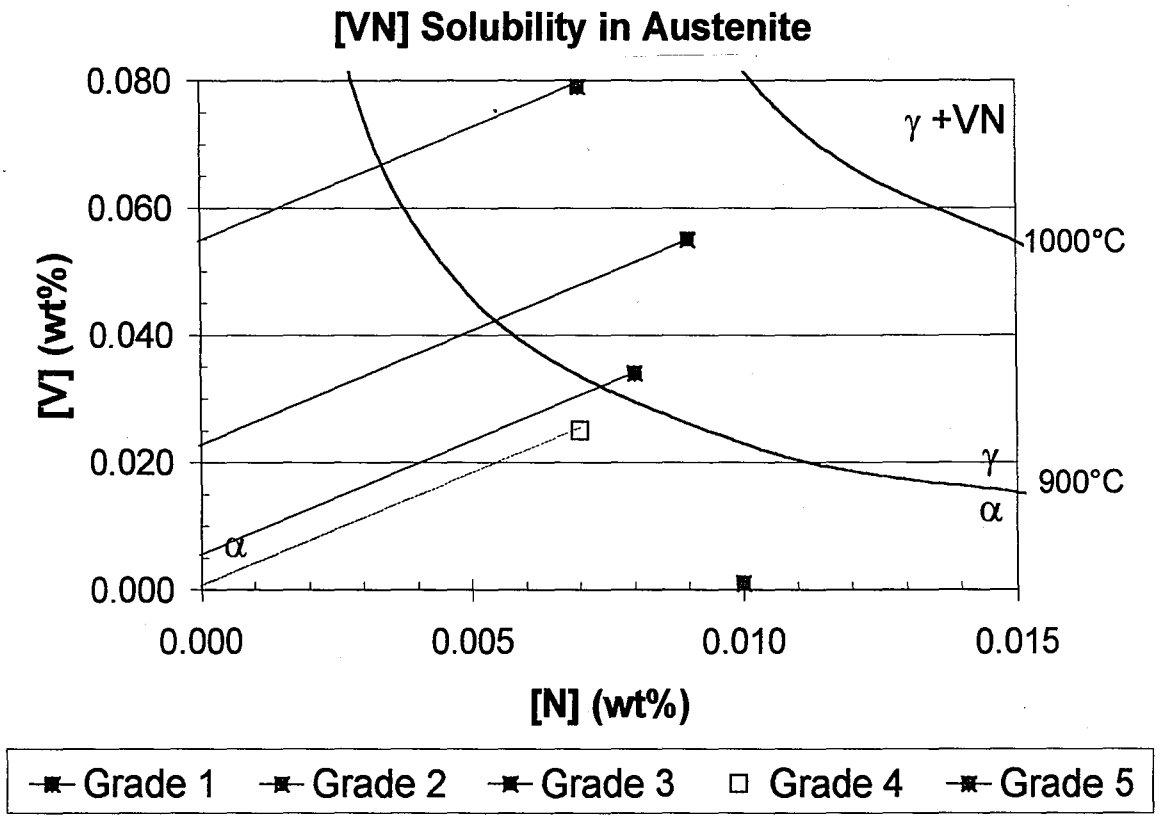

Figure 4-8. Nominal compositions imposed upon the solubility diagram of VN in austenite. Lines of VN stoichiometry are indicated.

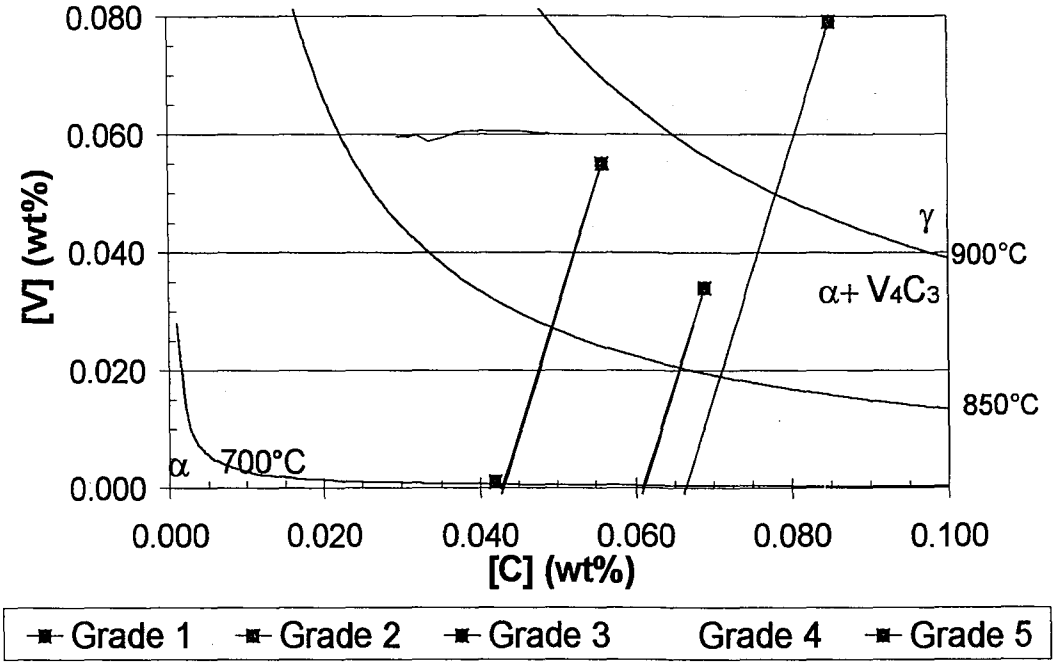

Figure 4-9. Nominal compositions imposed upon the solubility diagram of V_4C_3 in ferrite. Lines of stoichiometry indicate how the ferrite composition changes during the precipitation of V_4C_3.

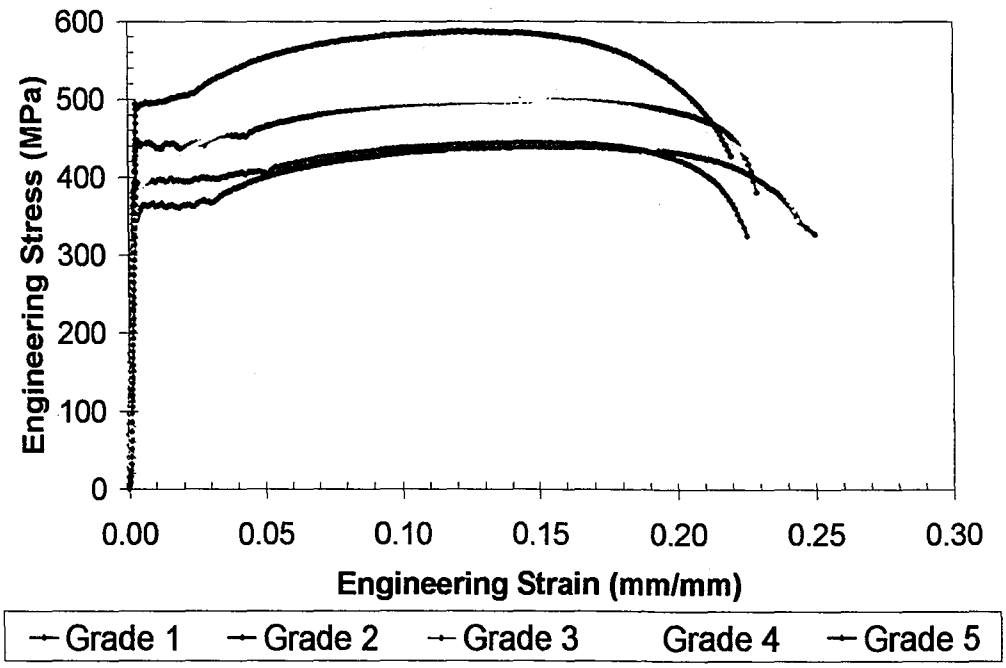

Figure 4-10. Typical engineering stress-strain curves for the as-rolled grades.

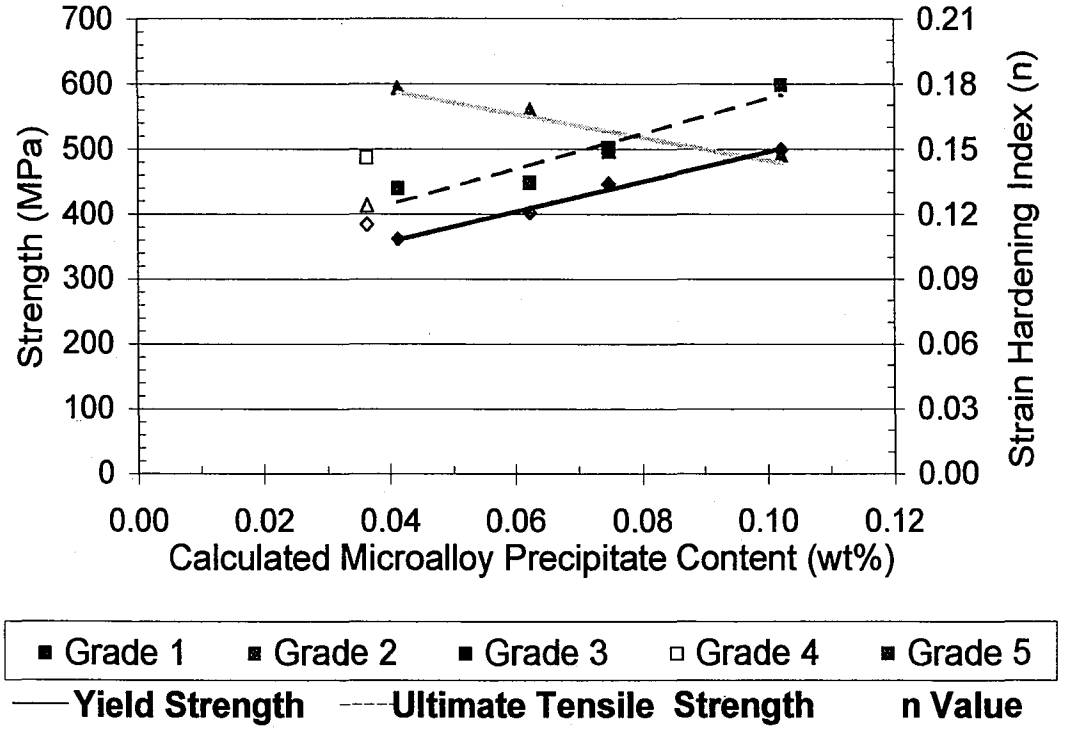

Figure 4-11. Effect of microalloy precipitate content on the mechanical properties of the as-rolled grades.

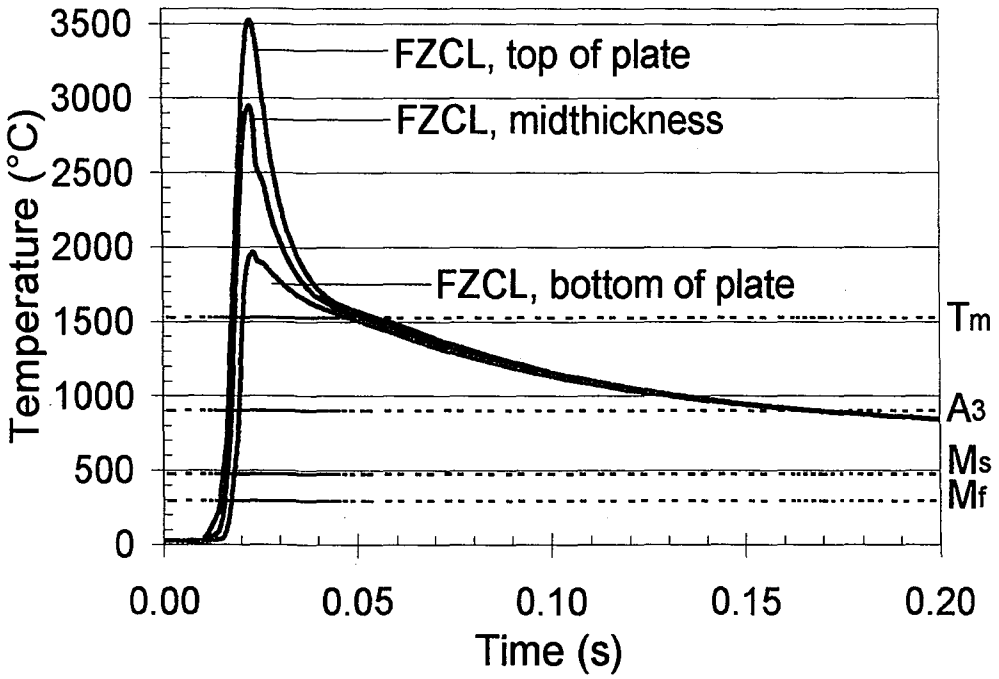

Figure 4-12. Plot of calculated FZCL laser weld thermal cycles for grade 3, showing the difference in calculated peak temperature as a function of thickness position.

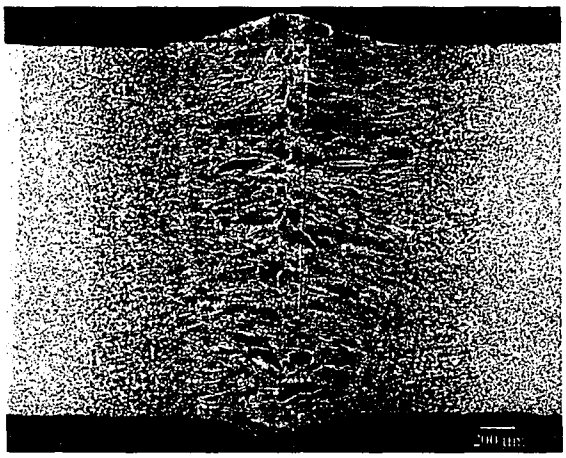

a) Grade 1 (2% Nital)

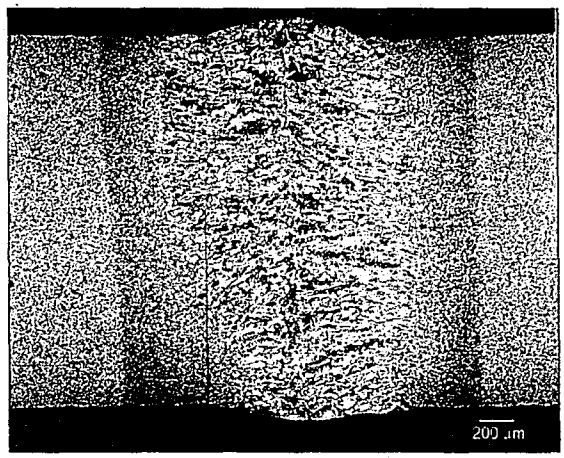

b) Grade 2 (2% Nital)

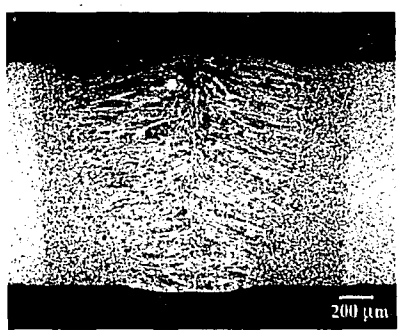

c) Grade 3 (2% Nital)

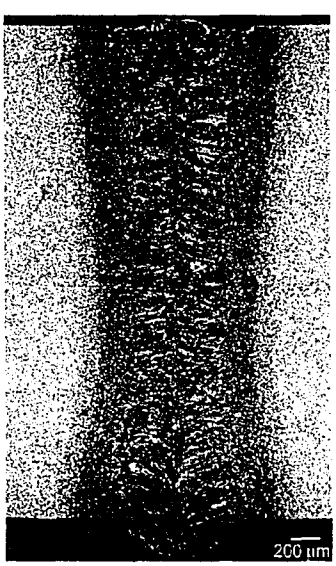

d) Grade 4 (2% Nital)

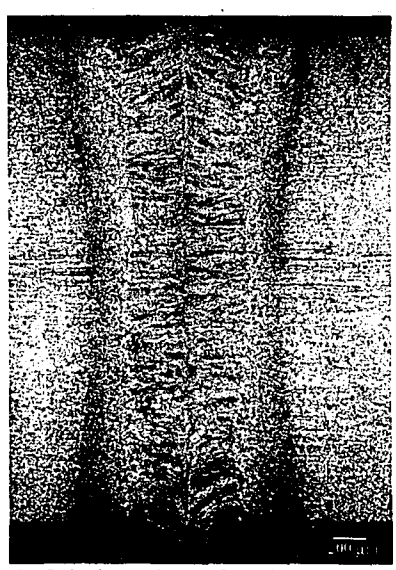

e) Grade 5 (4%Picral + 2% Nital)

Figure 4-13. Light optical micrographs comparing weld cross sections.

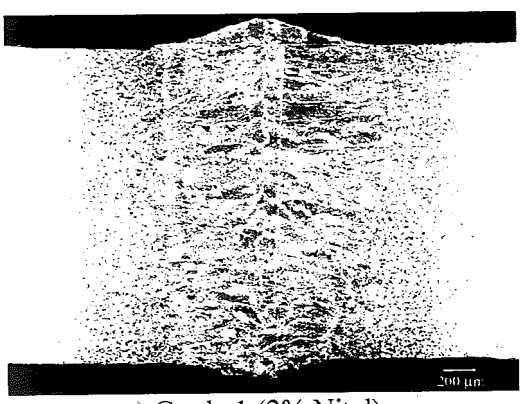

a) Grade 1 (2% Nital)

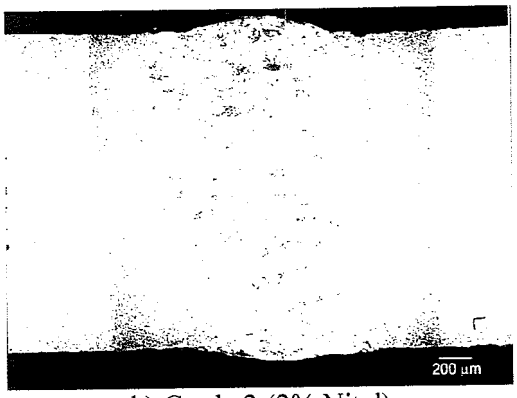

b) Grade 2 (2% Nital)

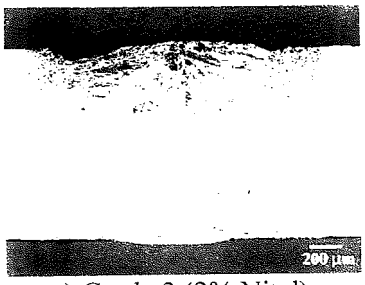

c) Grade 3 (2% Nital)

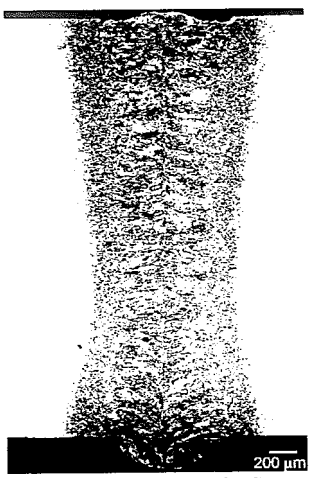

d) Grade 4 (2% Nital)

e) Grade 5 (4%Picral + 2% Nital)

Figure 4-13. Light optical micrographs comparing weld cross sections.

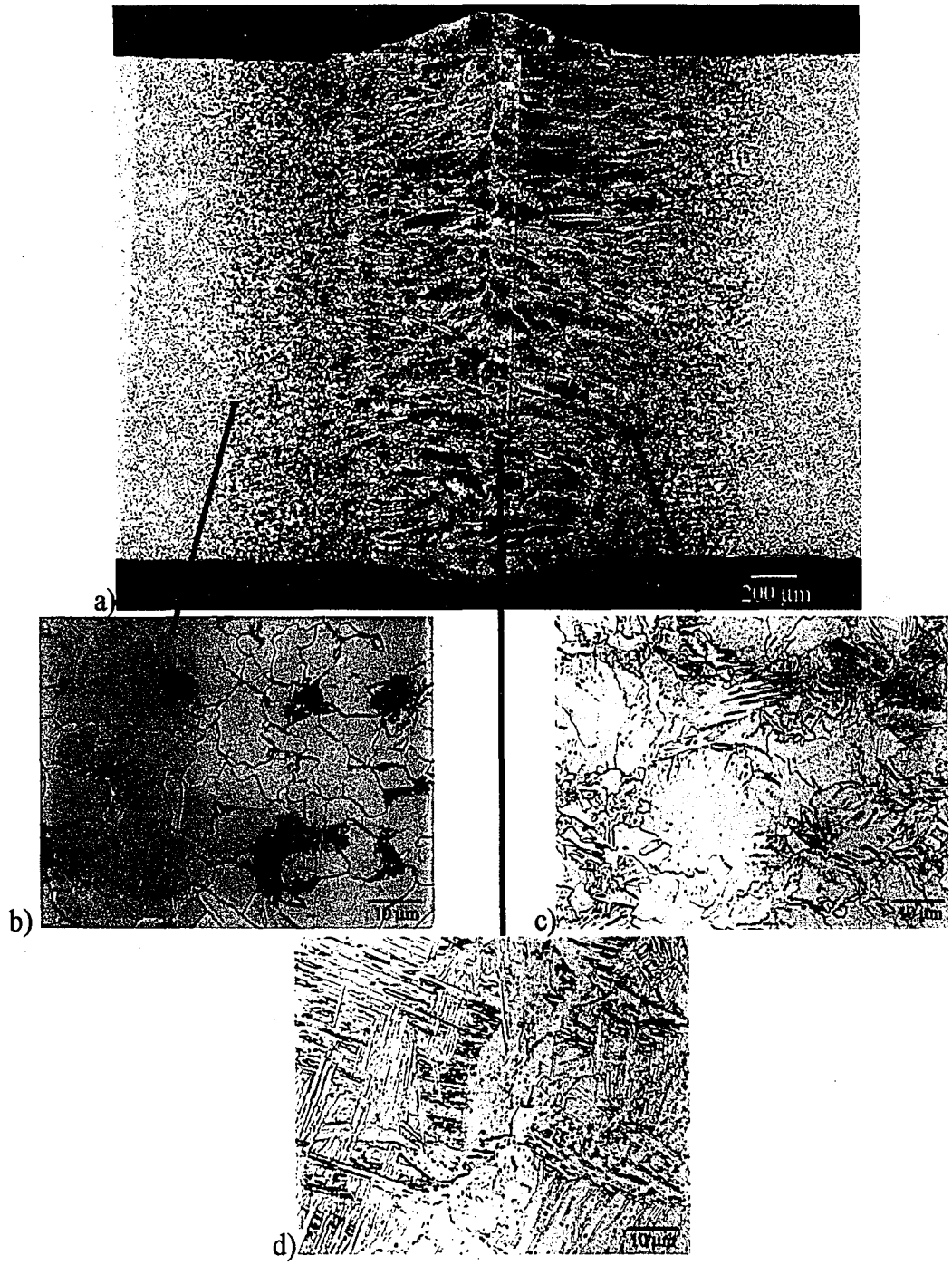

Figure 4-14. Light optical micrographs showing detail of the microstructures in grade 1 welds. a) Grade 1 cross section; b) in the subcritical HAZ; c) in the HAZ directly adjacent to the fusion line; d) at the FZCL. 2% Nital.

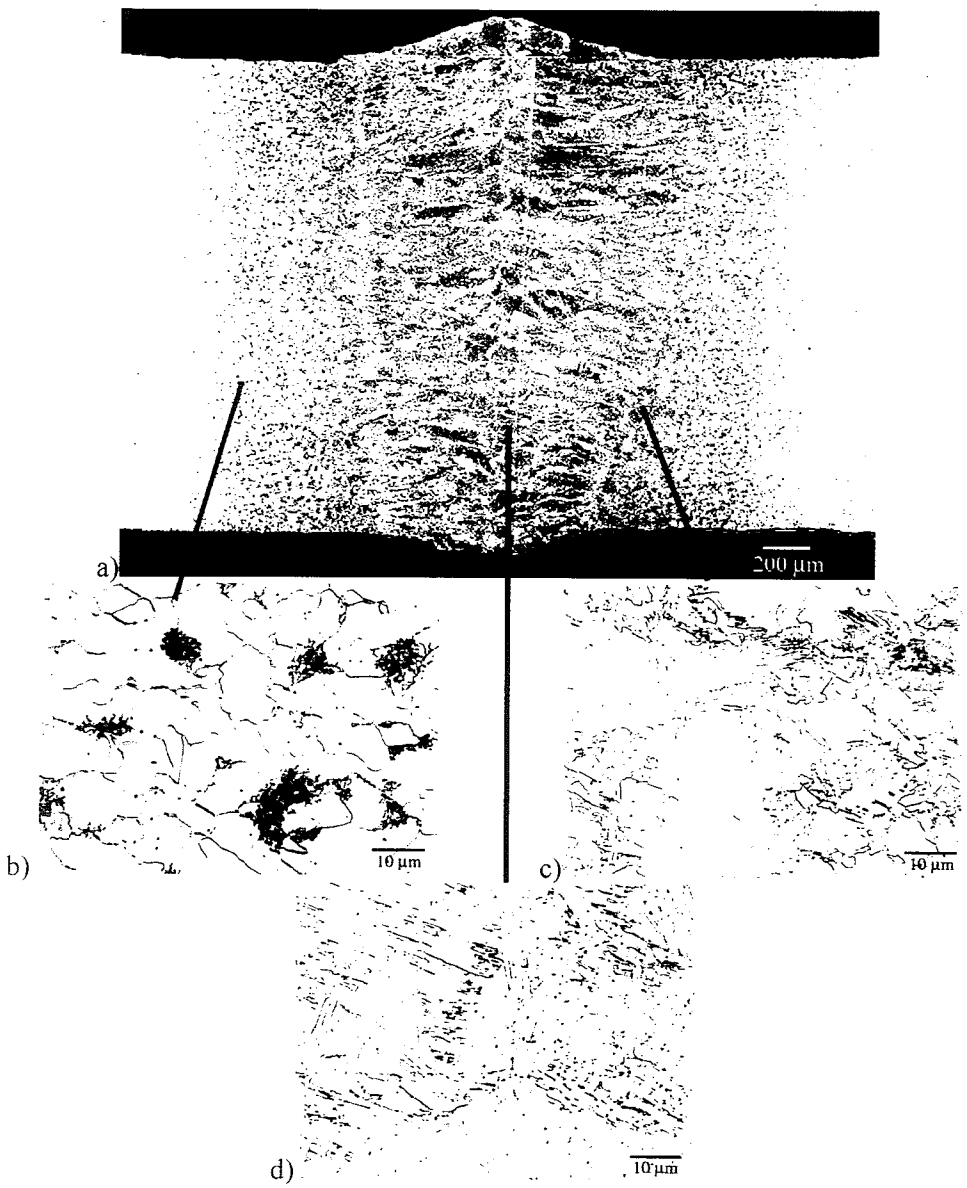

Figure 4-14. Light optical micrographs showing detail of the microstructures in grade 1 welds. a) Grade 1 cross section; b) in the subcritical HAZ; c) in the HAZ directly adjacent to the fusion line; d) at the FZCL. 2% Nital.

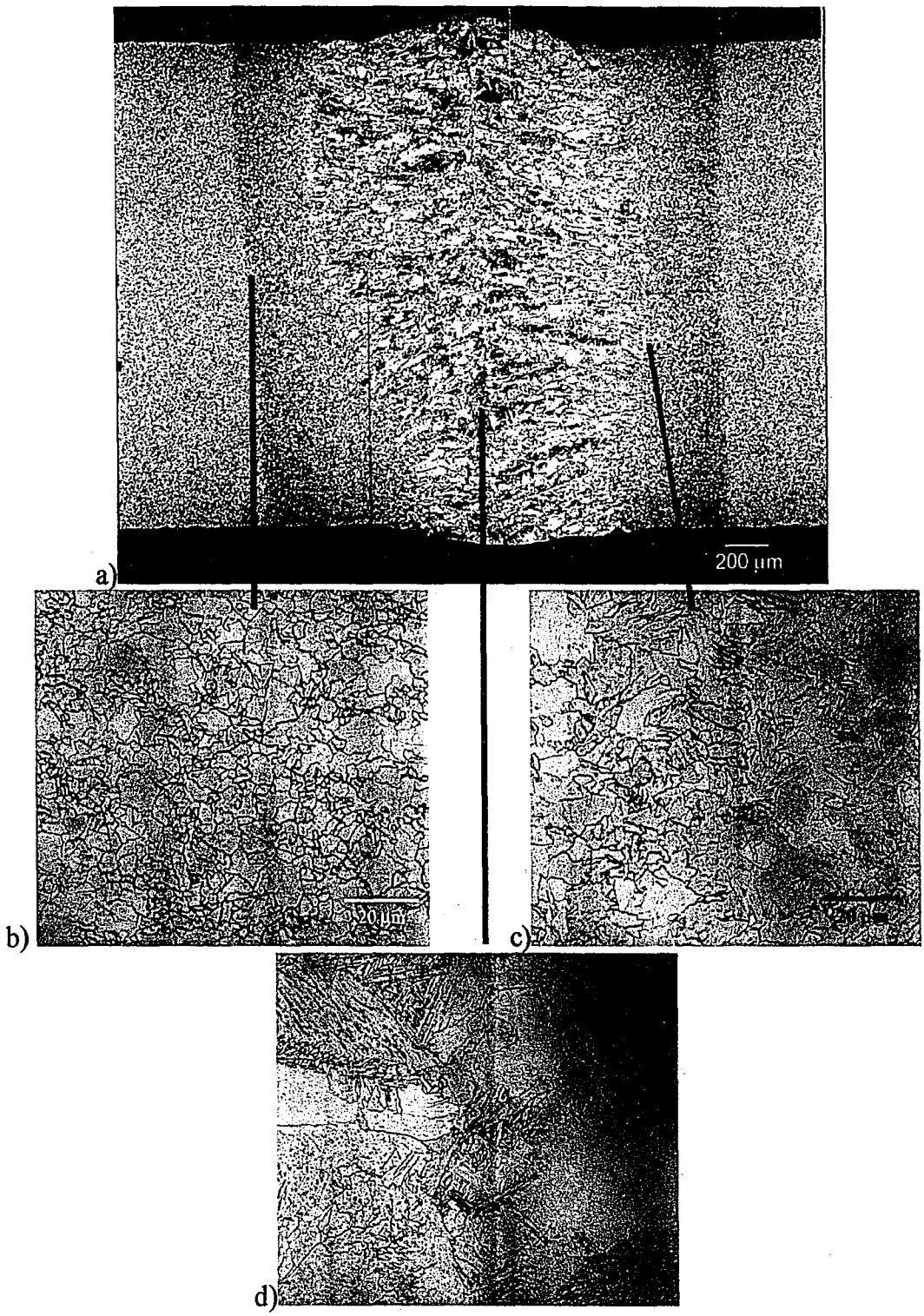

Figure 4-15. Light optical micrographs showing detail of the microstructures in grade 2 welds. a) Grade 2 cross section; b) in the fine-grained HAZ; c) in the HAZ directly adjacent to the fusion line; d) at the FZCL. 2% Nital.

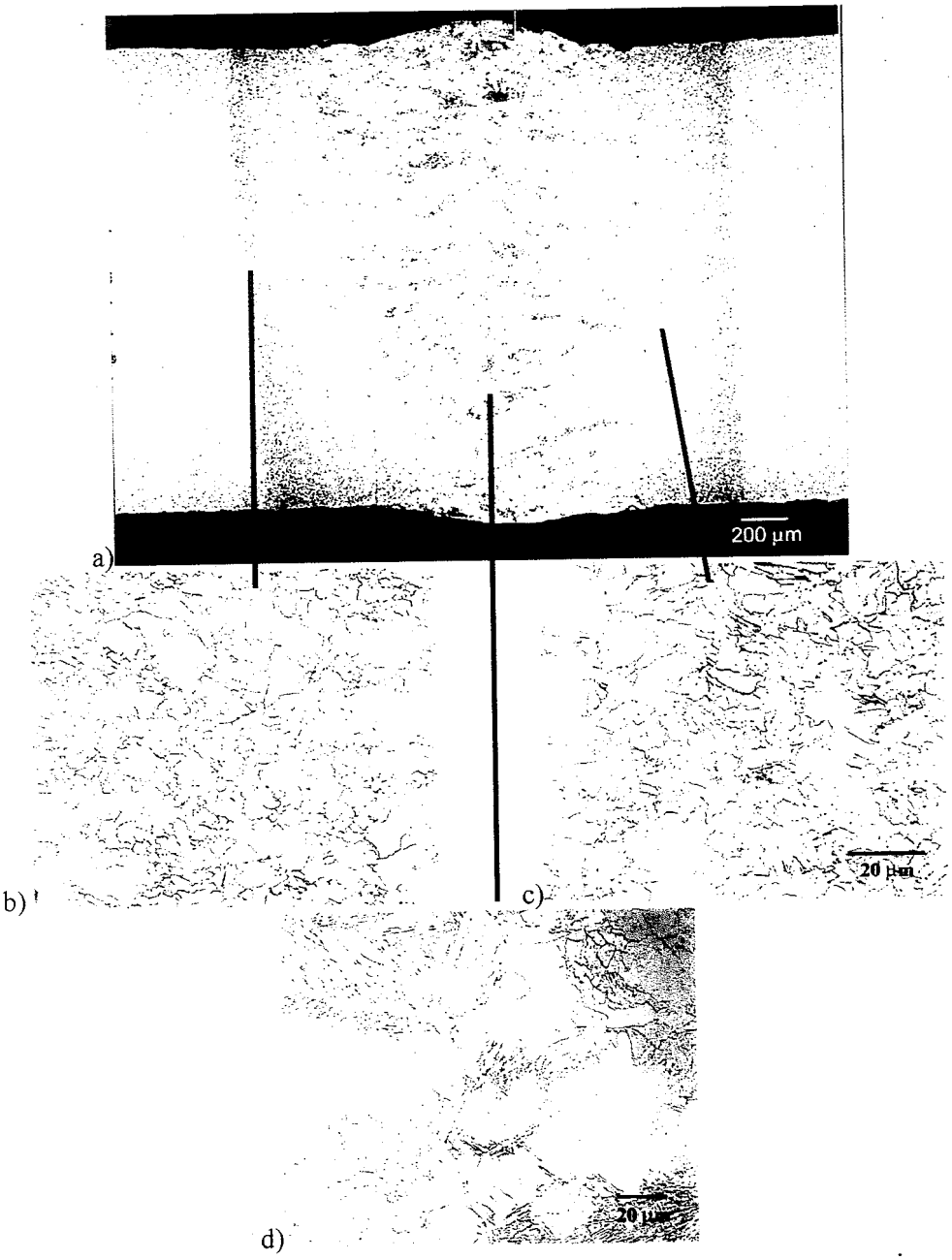

Figure 4-15. Light optical micrographs showing detail of the microstructures in grade 2 welds. a) Grade 2 cross section; b) in the fine-grained HAZ; c) in the HAZ directly adjacent to the fusion line; d) at the FZCL. 2% Nital.

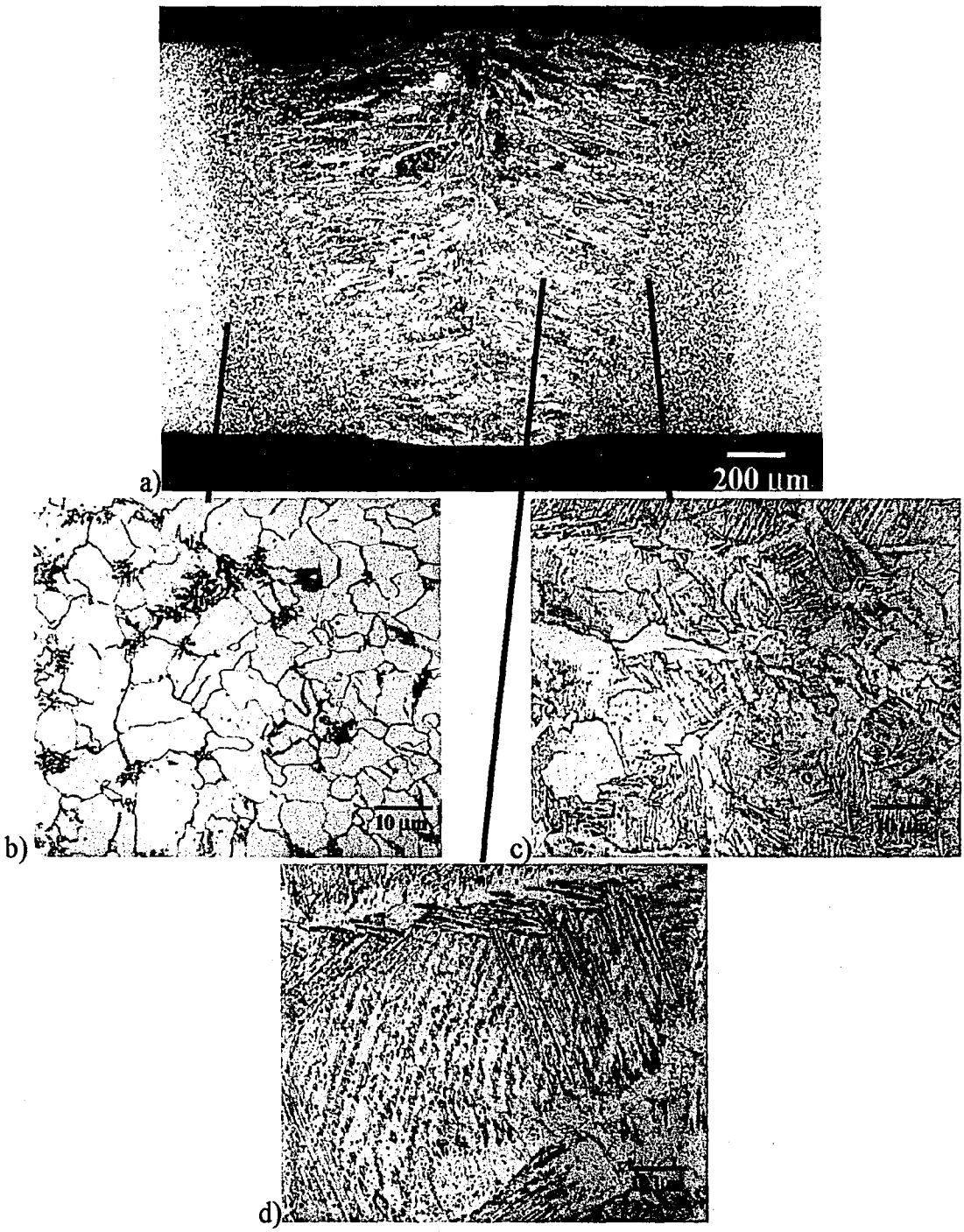

Figure 4-16. Light optical micrographs showing detail of the microstructures in grade 3 welds. a) Grade 3 cross section; b) in the subcritical HAZ; c) in the HAZ directly adjacent to the fusion line; d) within the fusion zone. 2% Nital.

Figure 4-16. Light optical micrographs showing detail of the microstructures in grade 3 welds. a) Grade 3 cross section; b) in the subcritical HAZ; c) in the HAZ directly adjacent to the fusion line; d) within the fusion zone. 2% Nital.

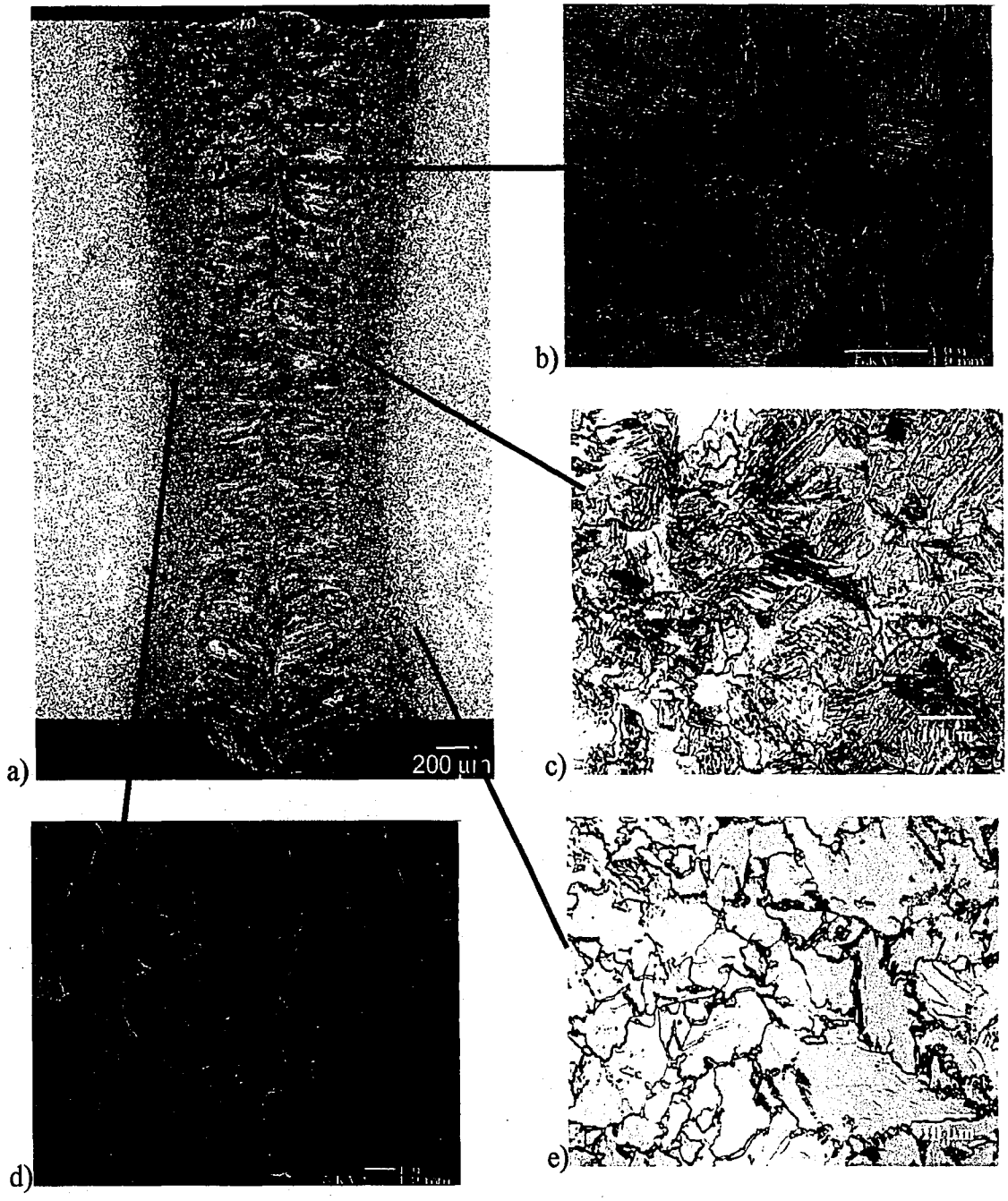

Figure 4-17. Micrographs showing detail of the microstructure in the grade 4 welds. a) cross section; b) at the FZCL; c) in the HAZ directly adjacent to the fusion line; d) massive ferrite in the HAZ; e) in the subcritical HAZ. 2% Nital.

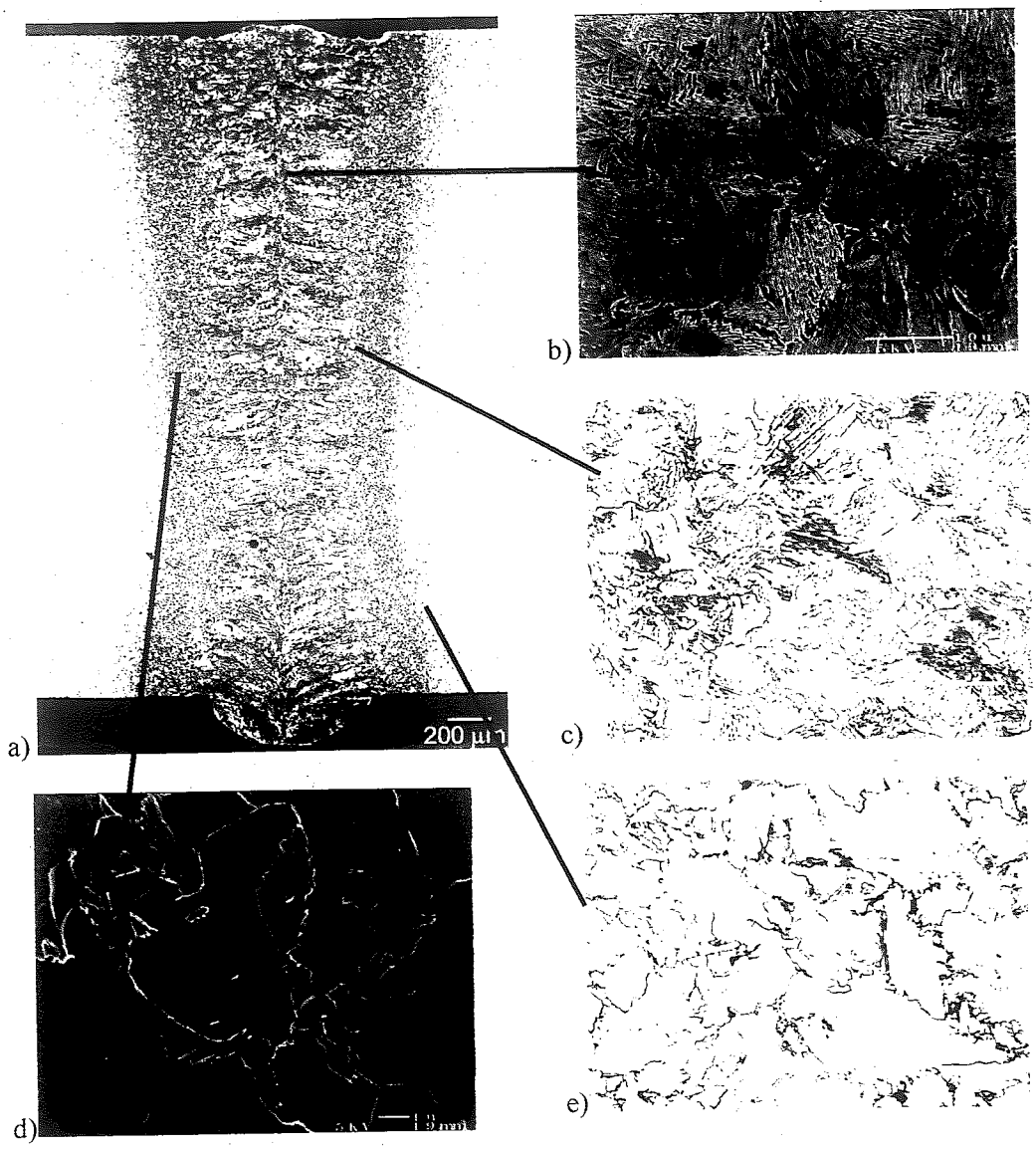

Figure 4-17. Micrographs showing detail of the microstructure in the grade 4 welds. a) cross section; b) at the FZCL; c) in the HAZ directly adjacent to the fusion line; d) massive ferrite in the HAZ; e) in the subcritical HAZ. 2% Nital.

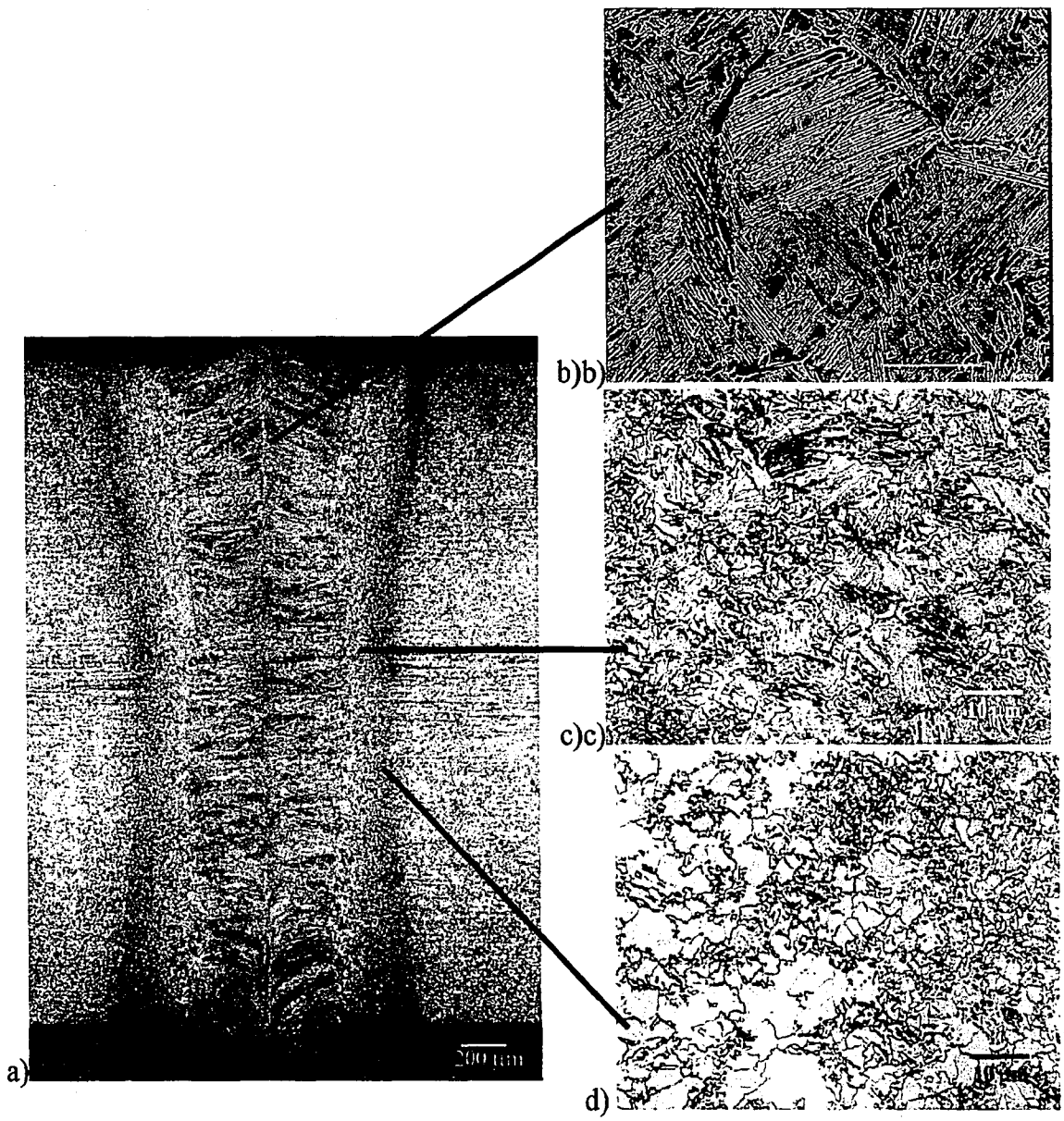

Figure 4-18. Micrographs showing detail of the microstructural gradient in the grade 5 welds. a) cross section (4% Picral + 2 % Nital); b) at the FZCL; c) in the HAZ directly adjacent to the fusion line; d) in the subcritical HAZ. 2% Nital.+ 4% Picral.

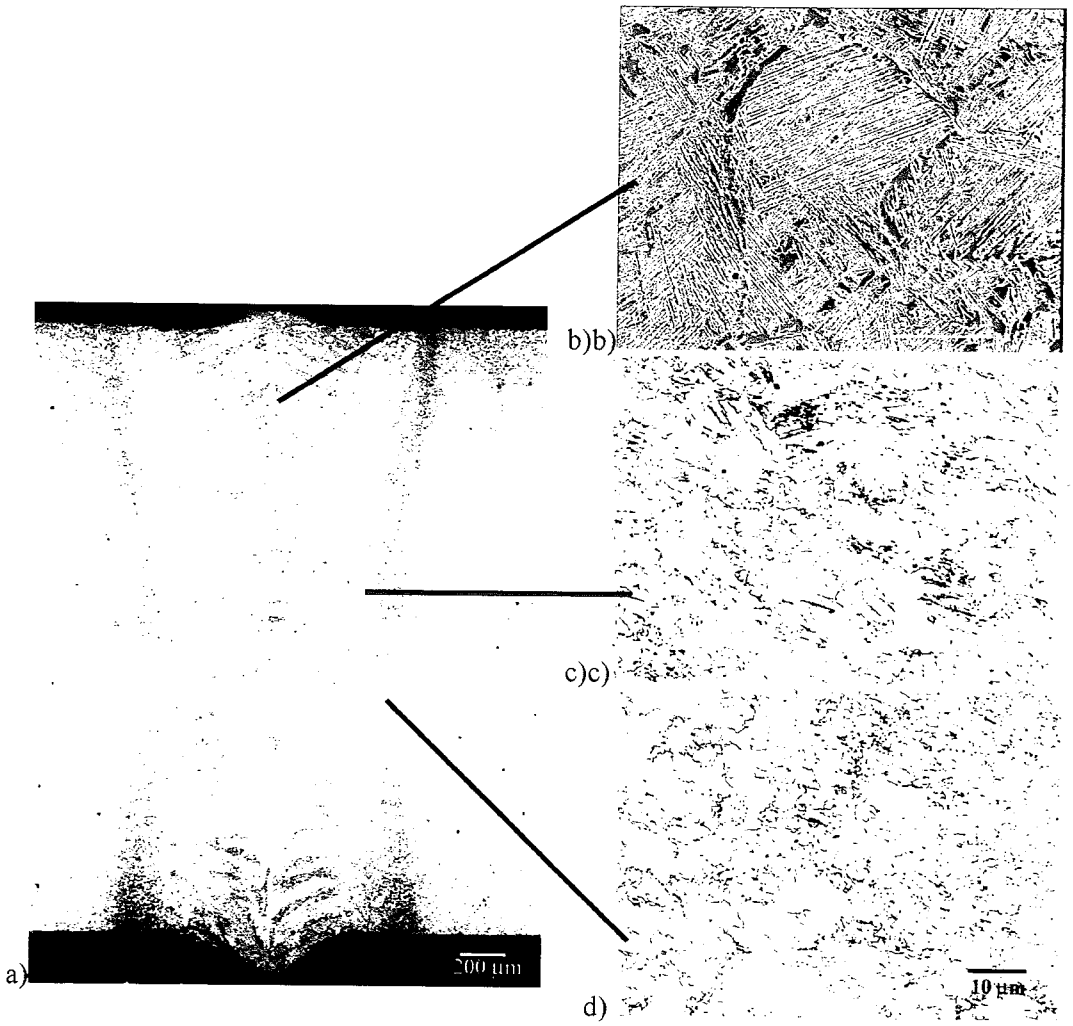

Figure 4-18. Micrographs showing detail of the microstructural gradient in the grade 5 welds. a) cross section (4% Picral + 2 % Nital); b) at the FZCL; c) in the HAZ directly adjacent to the fusion line; d) in the subcritical HAZ. 2% Nital.+ 4% Picral.

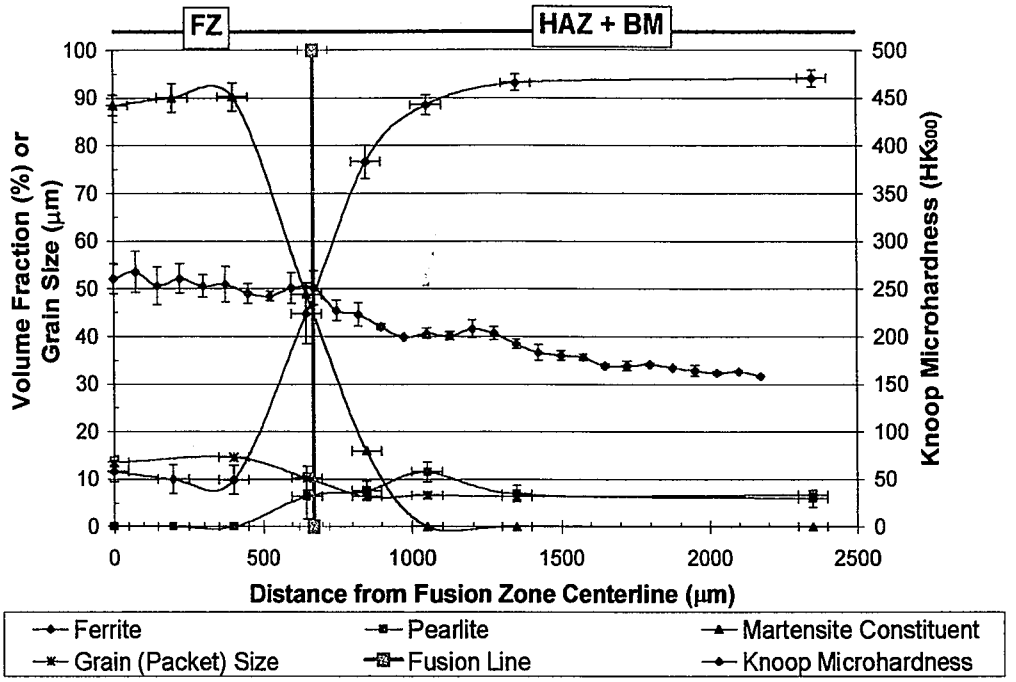

Figure 4-19a. Results of quantitative microscopy and microhardness testing of grade 1, showing the constituents and microhardness as a function of distance from the FZCL.

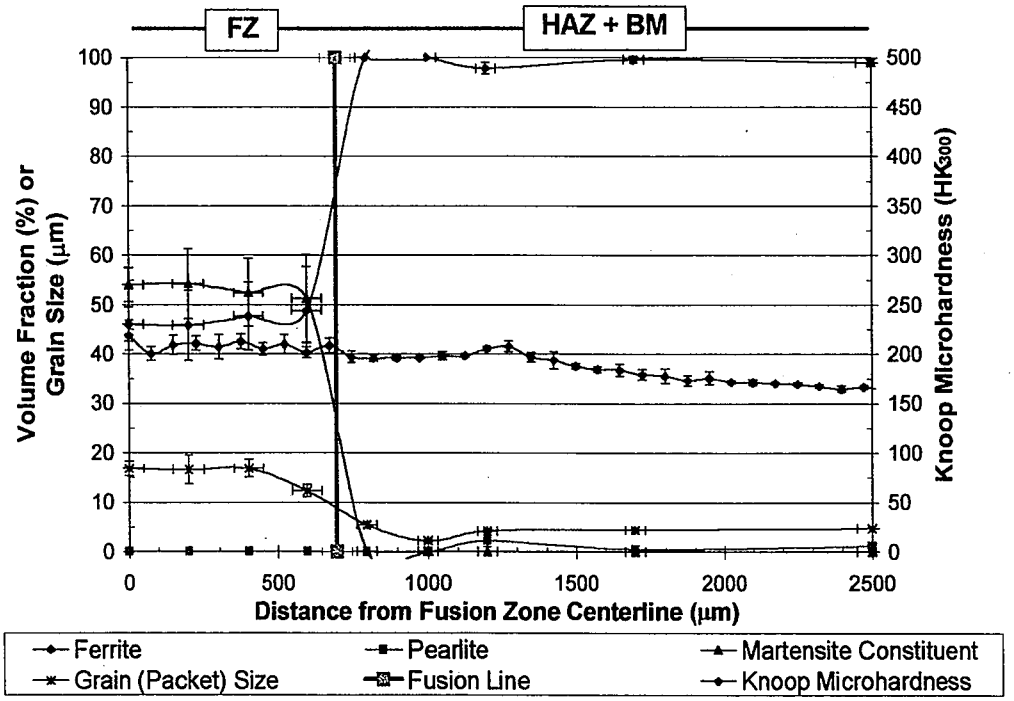

Figure 4-19b. Results of quantitative microscopy and microhardness testing of grade 2, showing the constituents and microhardness as a function of distance from the FZCL.

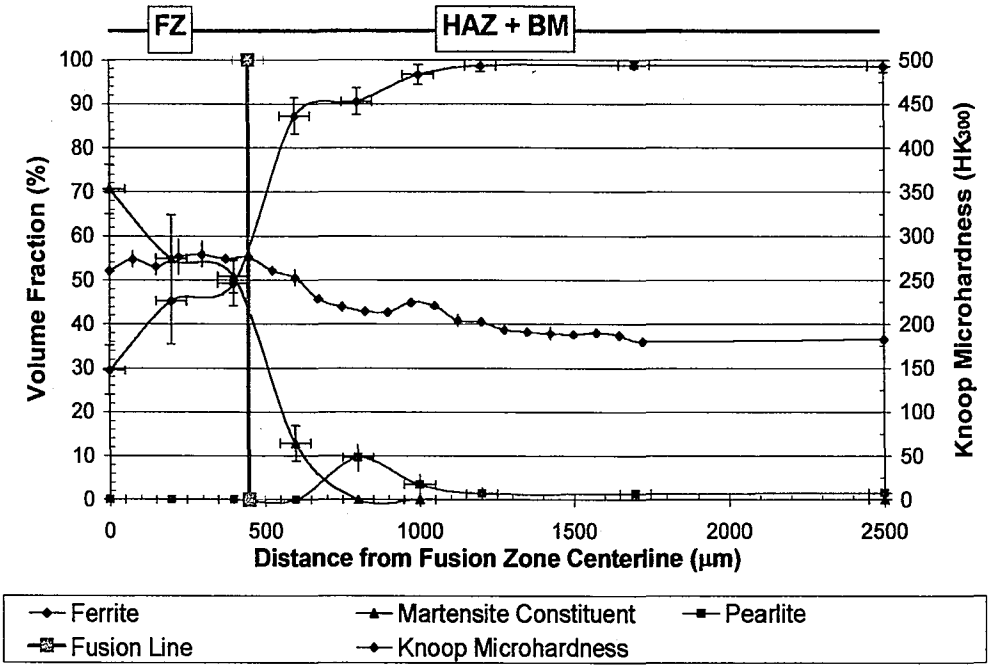

Figure 4-19c. Results of quantitative microscopy and microhardness testing of grade 3, showing the constituents and microhardness as a function of distance from the FZCL.

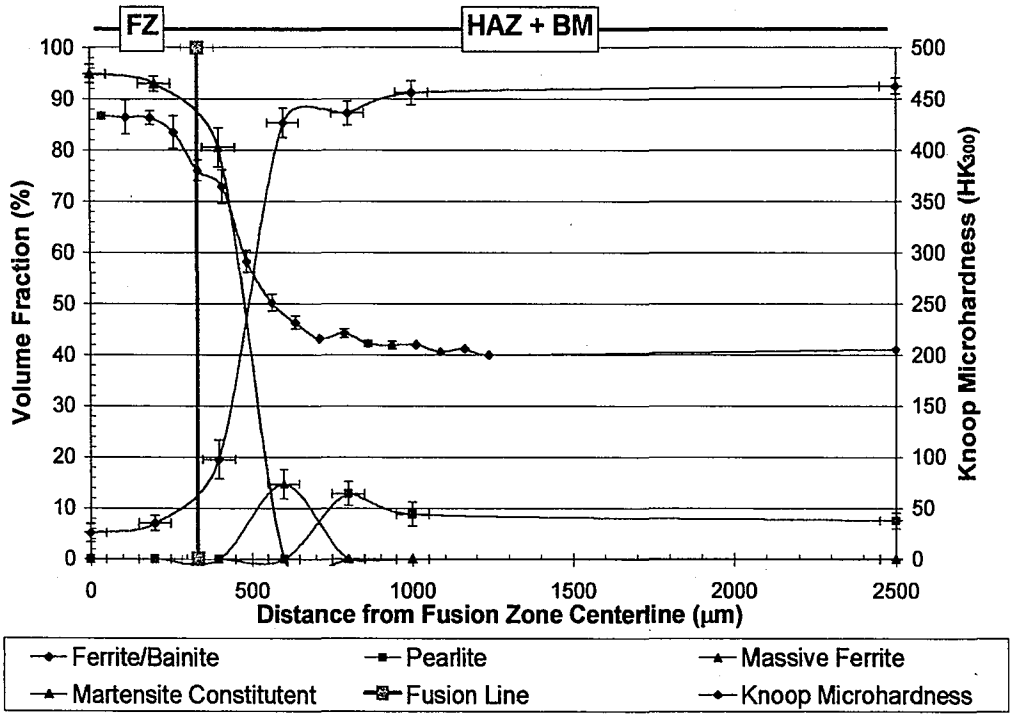

Figure 4-19d. Results of quantitative microscopy and microhardness testing of grade 4, showing the constituents and microhardness as a function of distance from the FZCL.

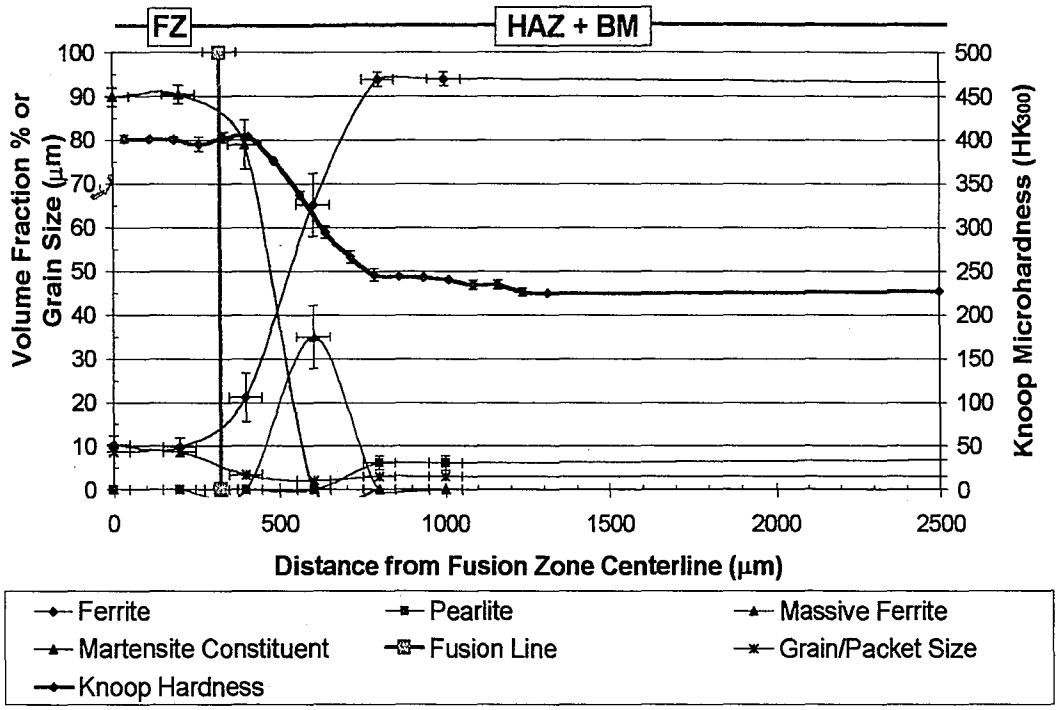

Figure 4-19 e. Results of quantitative microscopy and microhardness testing of grade 5, showing the constituents and microhardness as a function of distance from the FZCL.

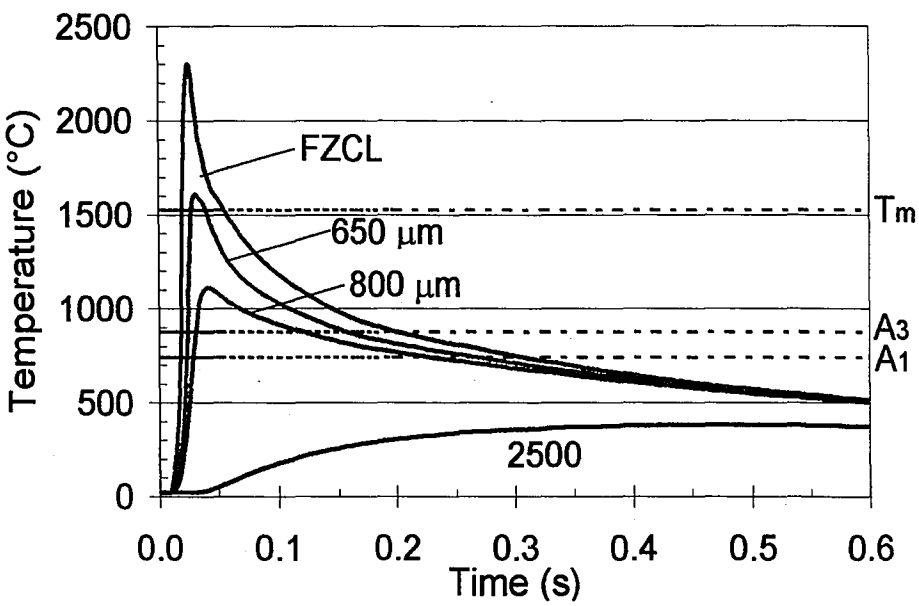

Figure 4-20 a. Calculated weld thermal cycles at selected distances from the FZCL of grades 1 and 2.

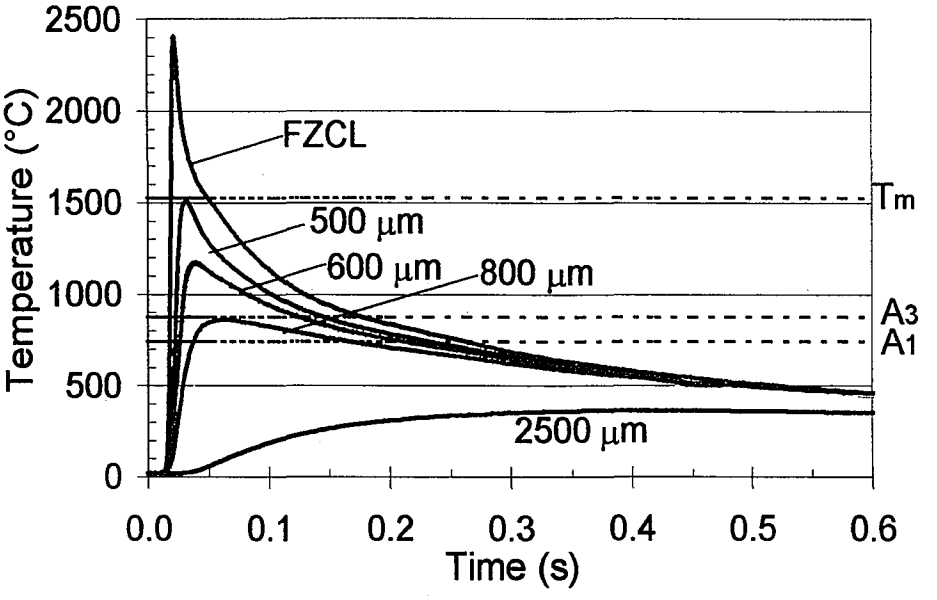

Figure 4-20 b. Calculated weld thermal cycles at selected distances from the FZCL of grade 3.

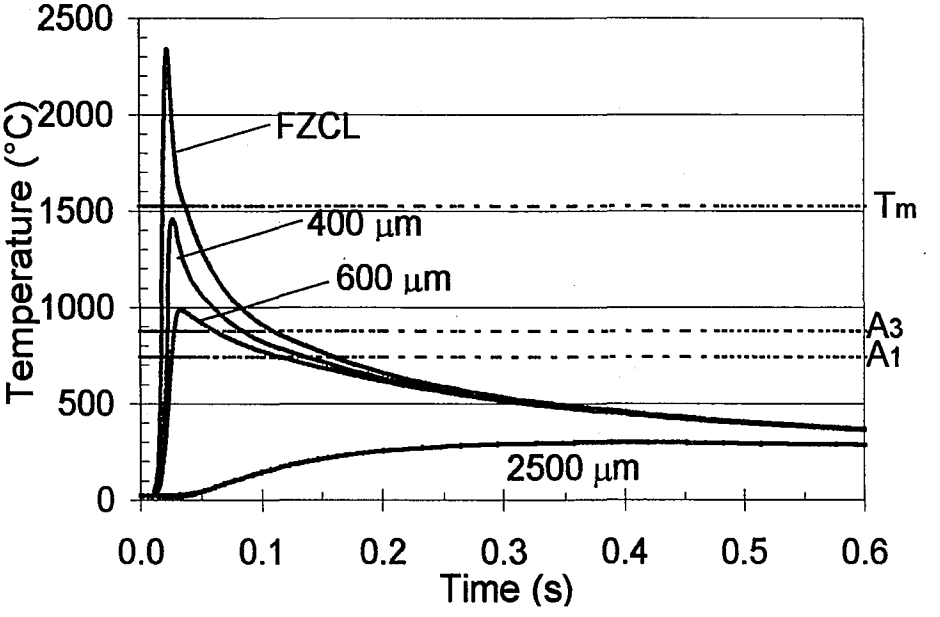

Figure 4-20 c. Calculated weld thermal cycles at selected distances from the FZCL of grades 4 and 5.

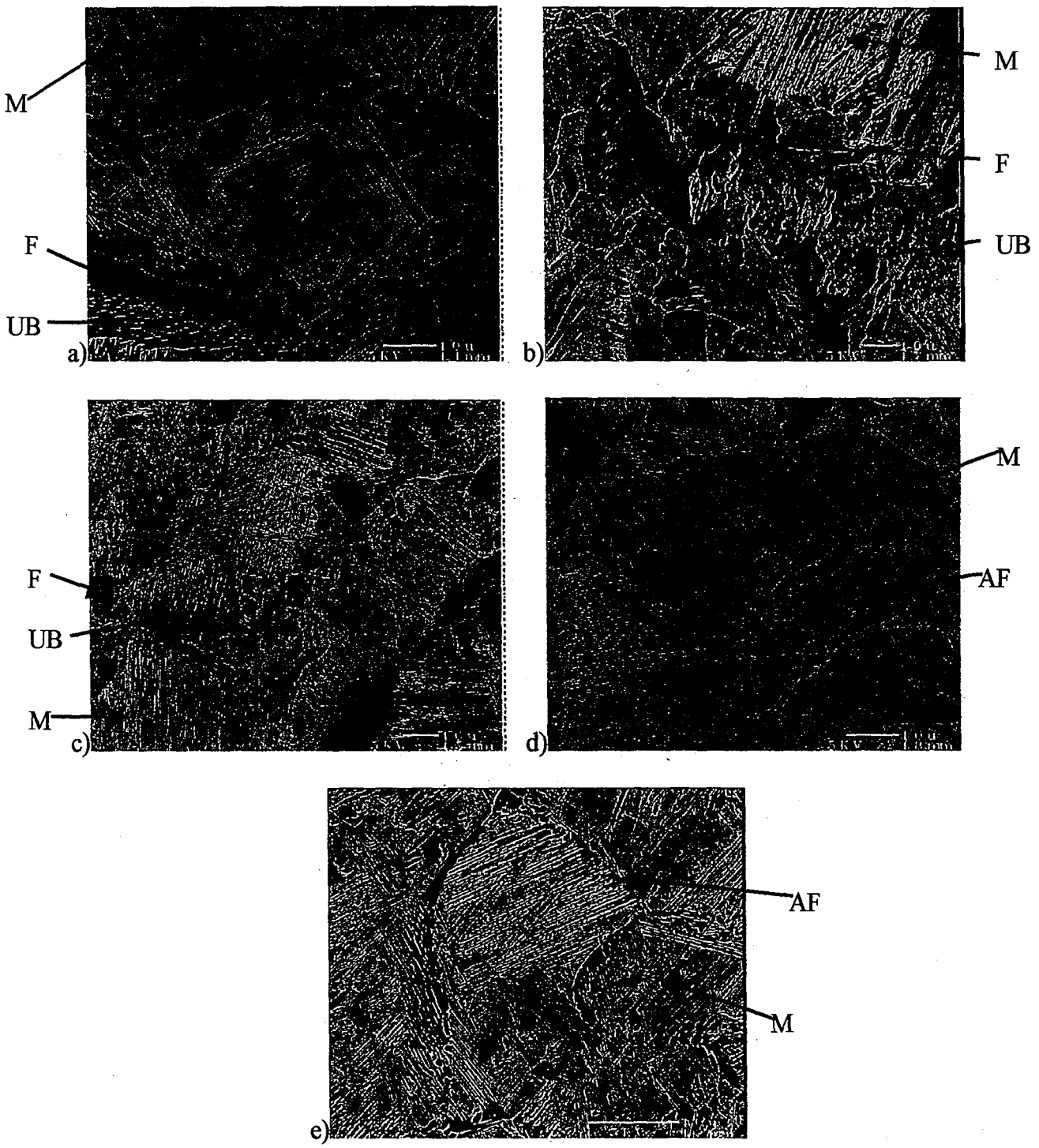

Figure 4-21. Typical appearance of lath martensite in HSLA laser weld fusion zones: a) grade 1, b) grade 2, c) grade 3, d) grade 4, e) grade 5. Microconstituents are labeled F (ferrite), UB (upper bainite), M (lower bainite and/or lath martensite), and AF (allotriomorphic ferrite).

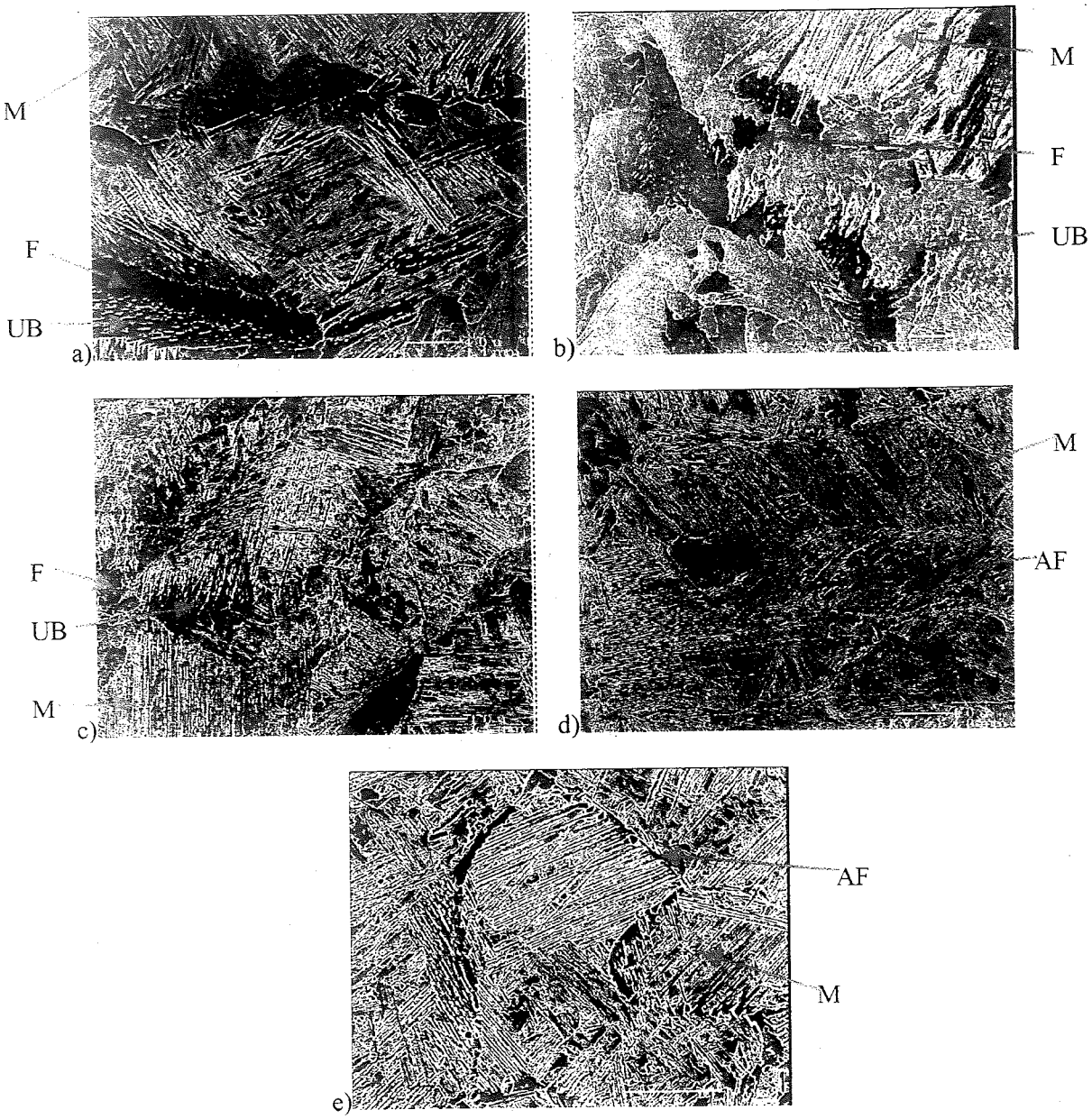

Figure 4-21. Typical appearance of lath martensite in HSLA laser weld fusion zones: a) grade 1, b) grade 2, c) grade 3, d) grade 4, e) grade 5. Microconstituents are labeled F (ferrite), UB (upper bainite), M (lower bainite and/or lath martensite), and AF (allotriomorphic ferrite).

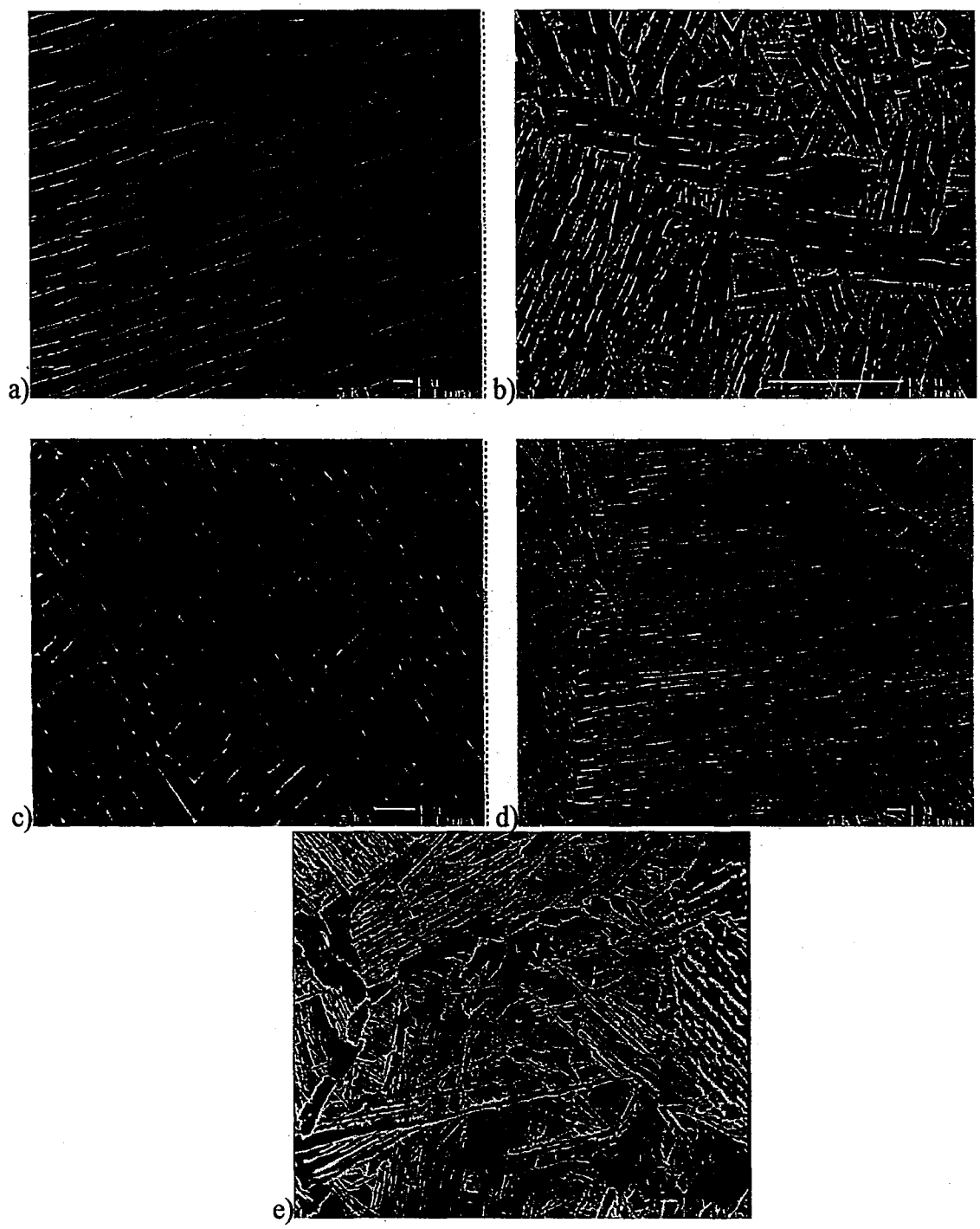

Figure 4-22. SEM micrographs showing detail of the lath martensite structure, as observed in the fusion zones of a) grade 1, b) grade 2, c) grade 3, d) grade 4, e) grade 5.

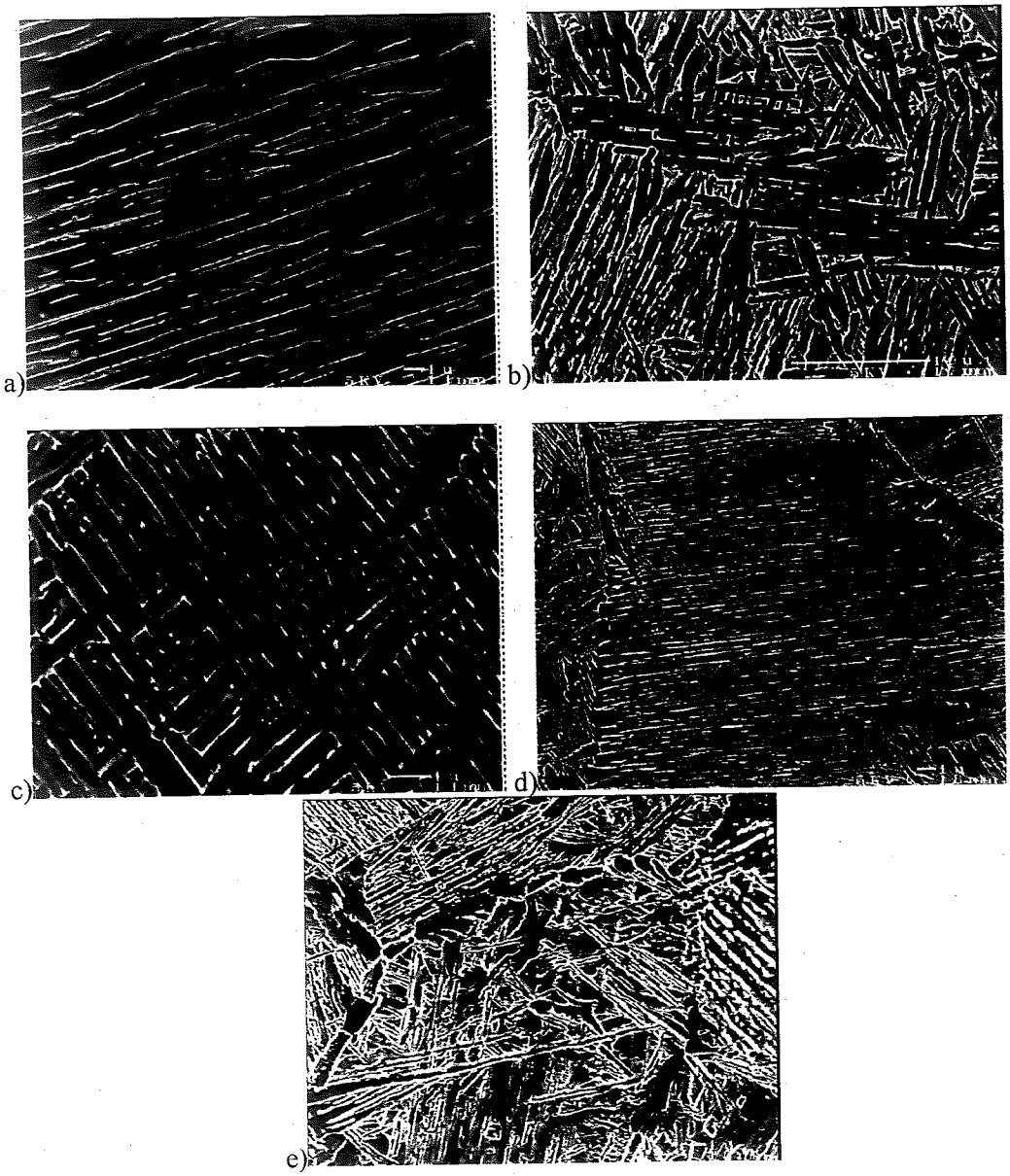

Figure 4-22. SEM micrographs showing detail of the lath martensite structure, as observed in the fusion zones of a) grade 1, b) grade 2, c) grade 3, d) grade 4, e) grade 5.

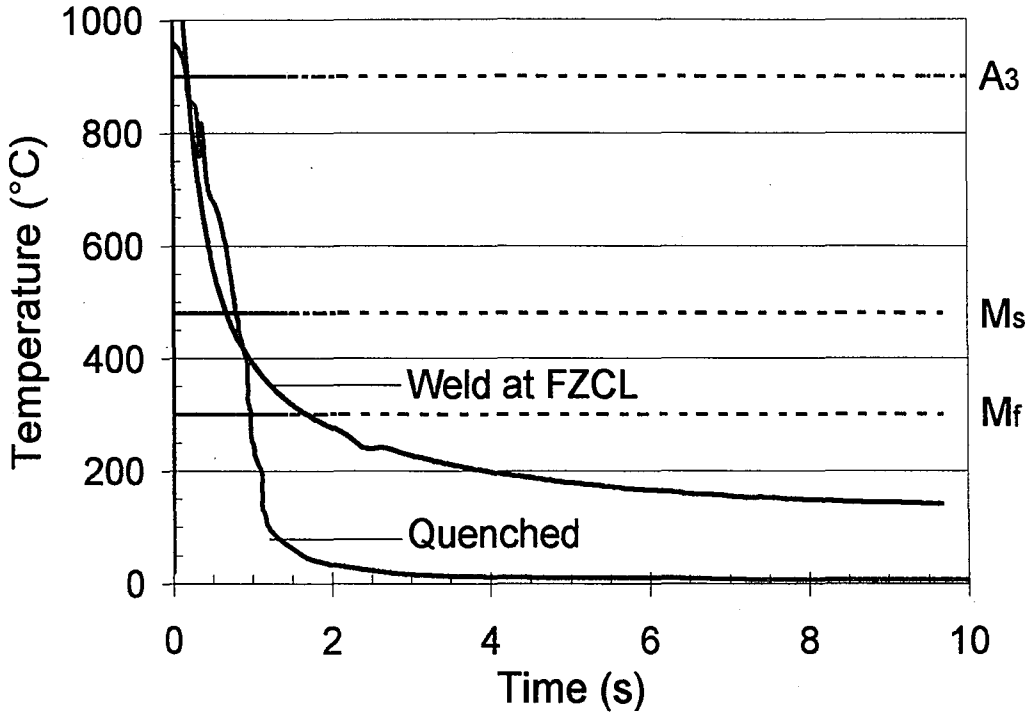

Figure 4-23 a. Comparison of calculated cooling rates during FZCL weld thermal cycles and experimentally determined cooling rates from brine quench for grades 1 and 2.

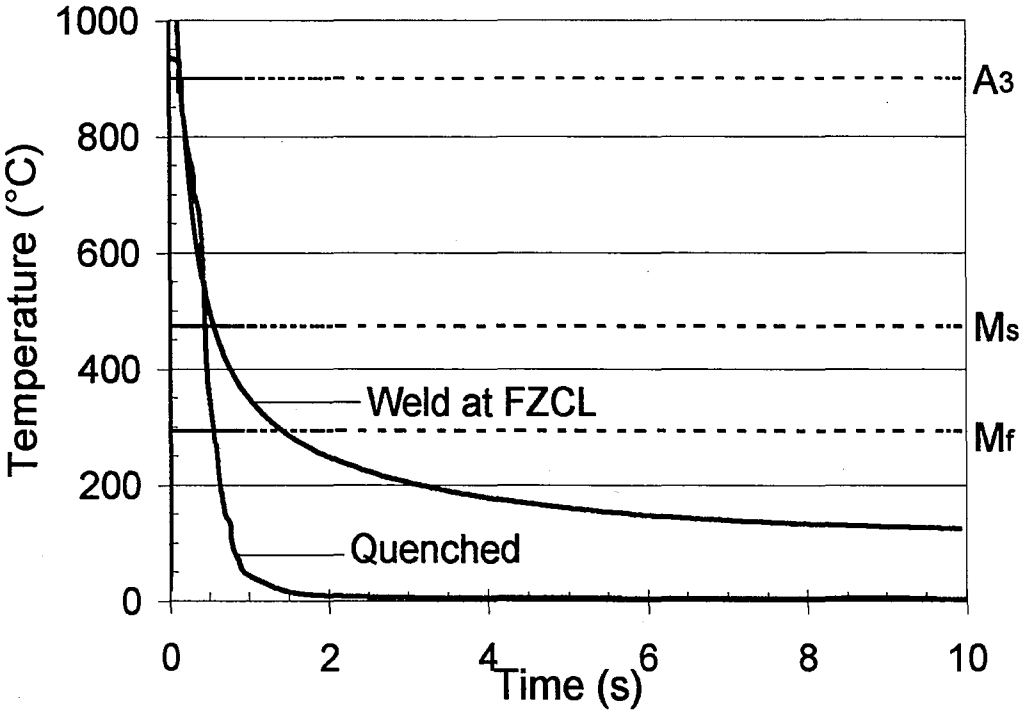

Figure 4-23 b. Comparison of calculated cooling rates during FZCL weld thermal cycles and experimentally determined cooling rates from brine quench for grade 3.

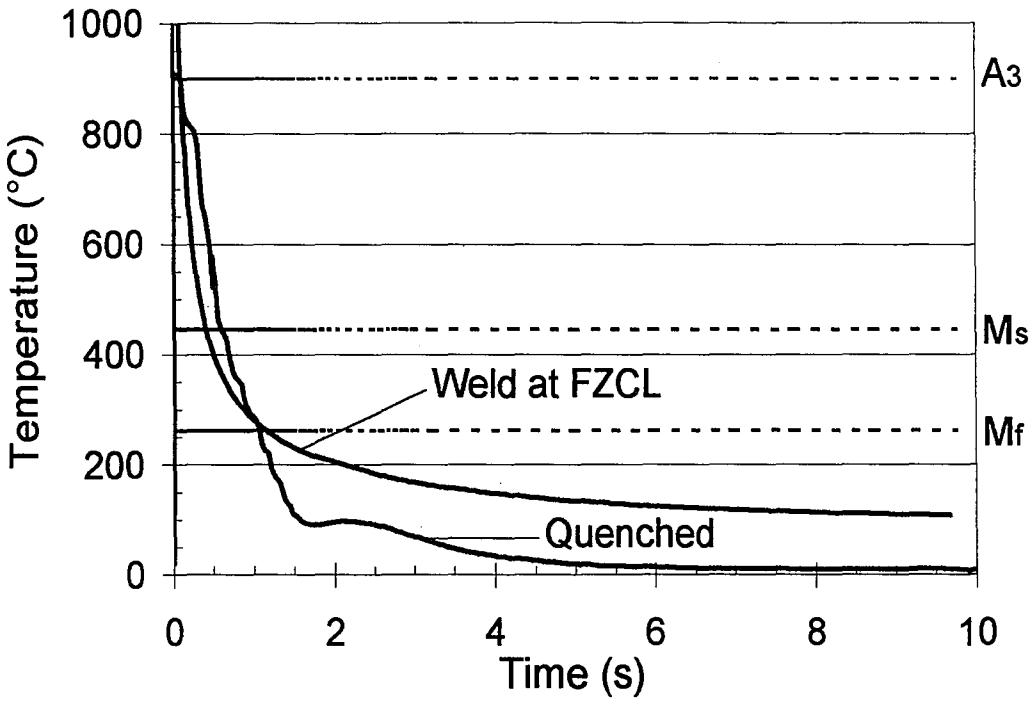

Figure 4-23 c. Comparison of calculated cooling rates during FZCL weld thermal cycles and experimentally determined cooling rates from brine quench for grades 4 and 5.

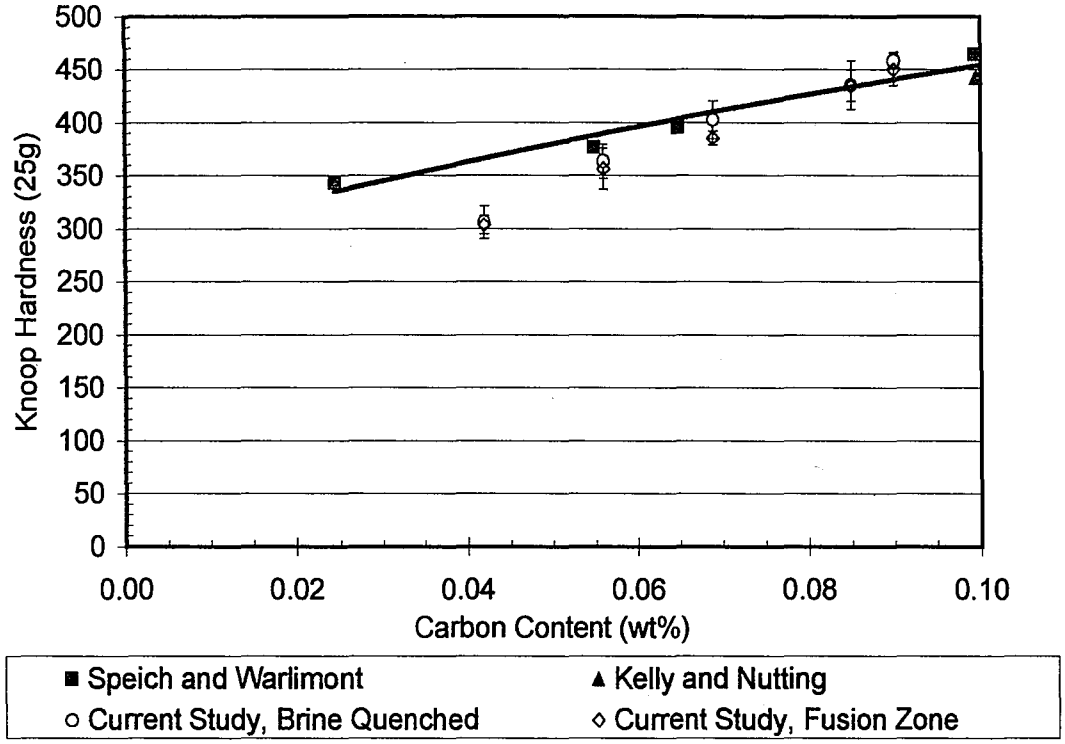

Figure 4-24. Comparison of martensite hardness in laser welds and austenitized and brine quenched samples to other researchers measurements on martensite that was not autotempered. The regression curve fits the data of Speich and Warlimont[90] and was used in calculating the softening response caused by autotempering.

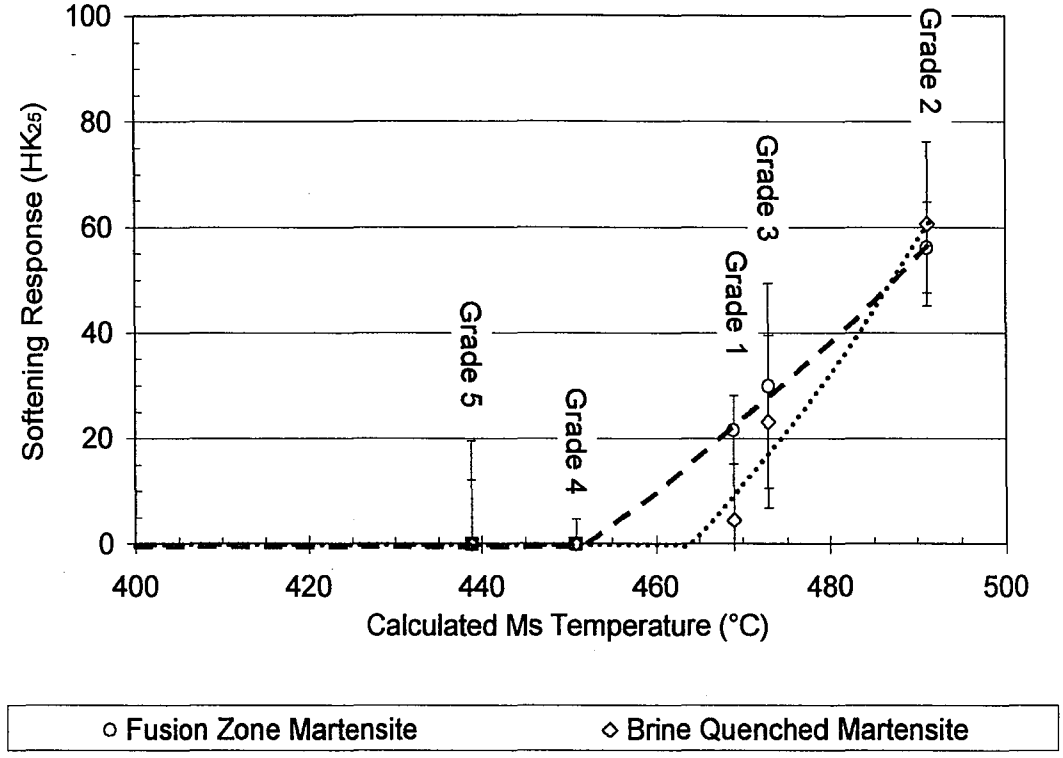

Figure 4-25. Effect of M_s temperature on the softening response associated with autotempering.

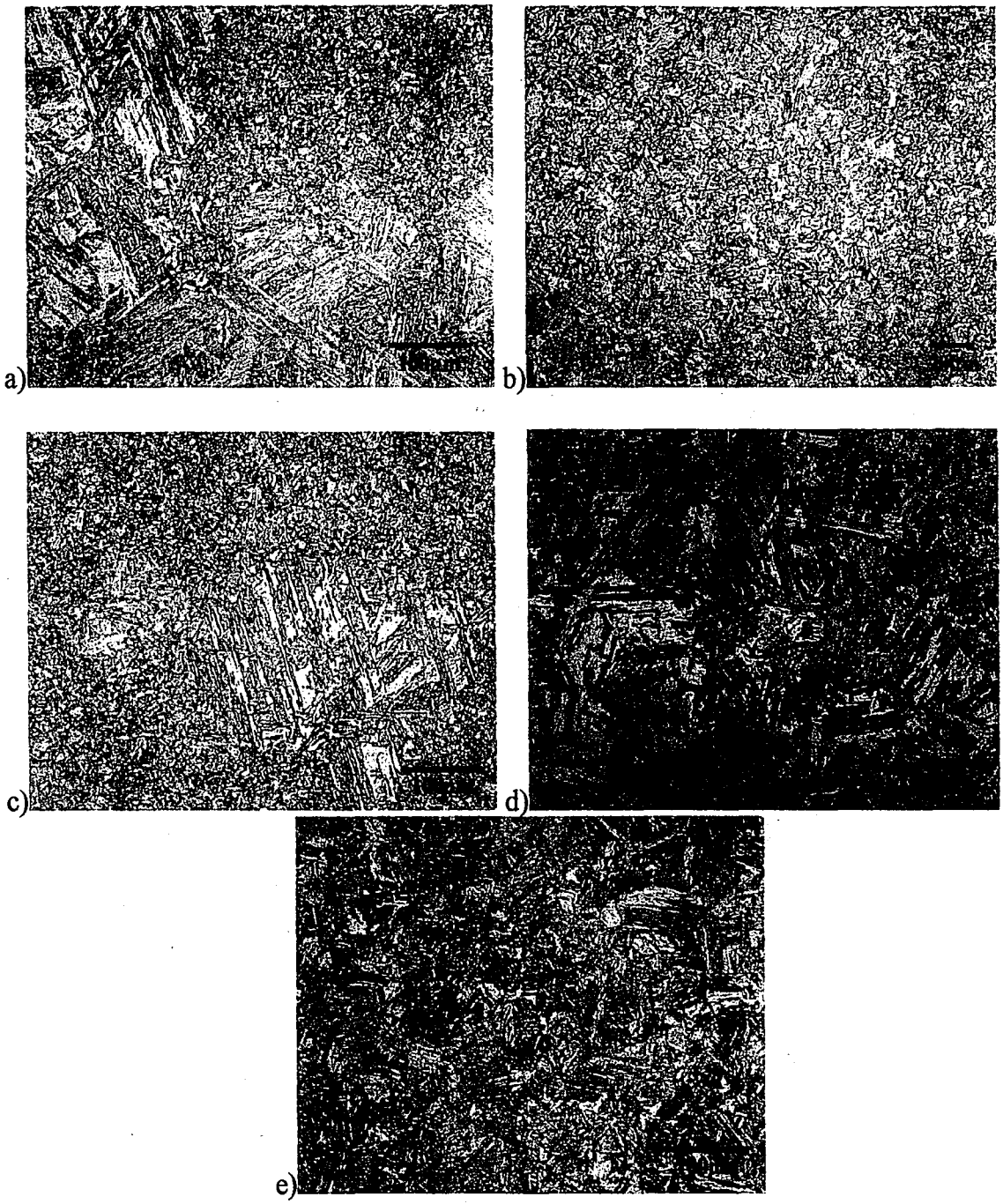

Figure 4-26. Micrographs showing representative microstructures of the austenitized and brine quenched samples: a) grade 1, b) grade 2, c) grade 3, d) grade 4, e) grade 5.

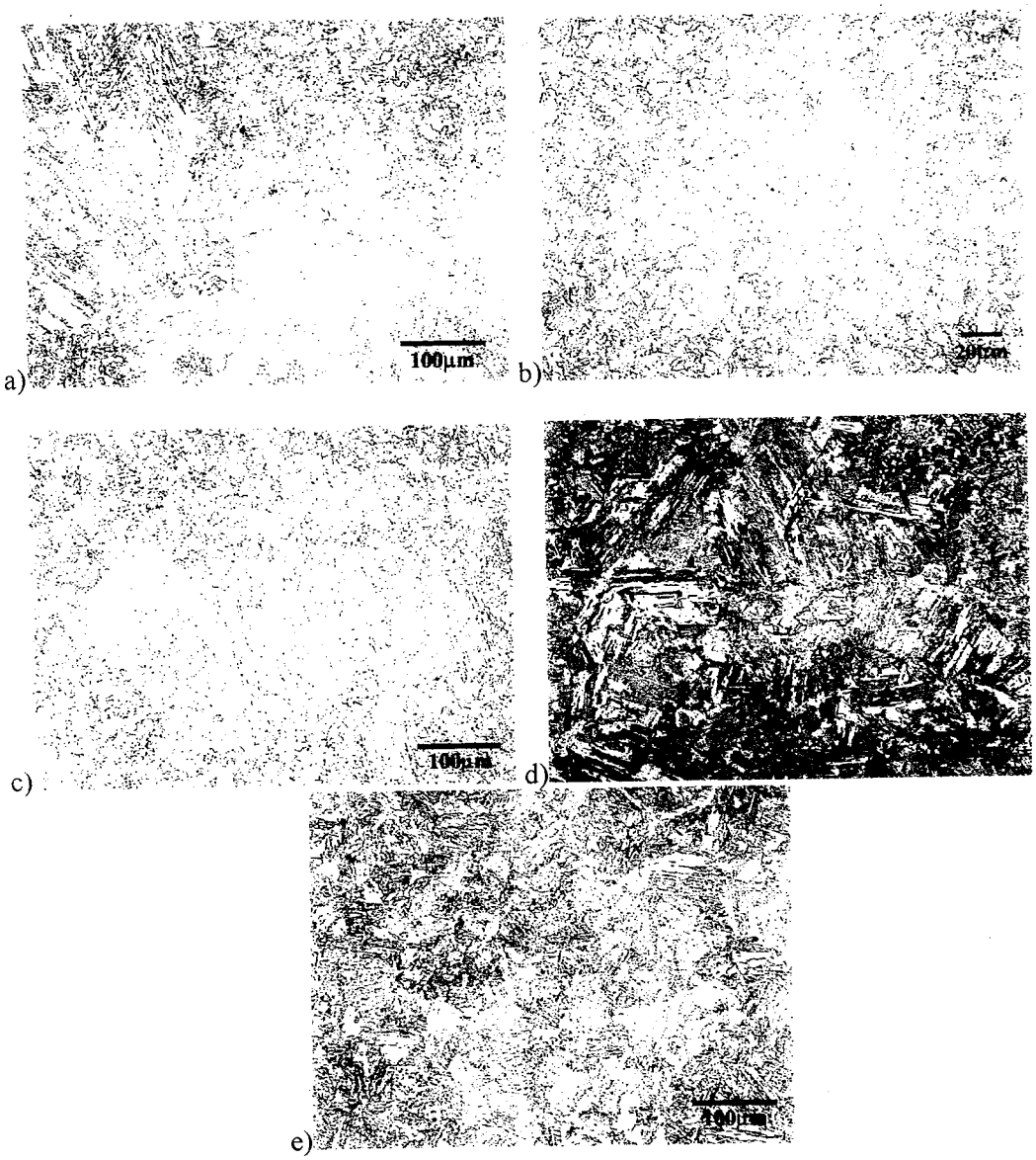

Figure 4-26. Micrographs showing representative microstructures of the austenitized and brine quenched samples: a) grade 1, b) grade 2, c) grade 3, d) grade 4, e) grade 5.

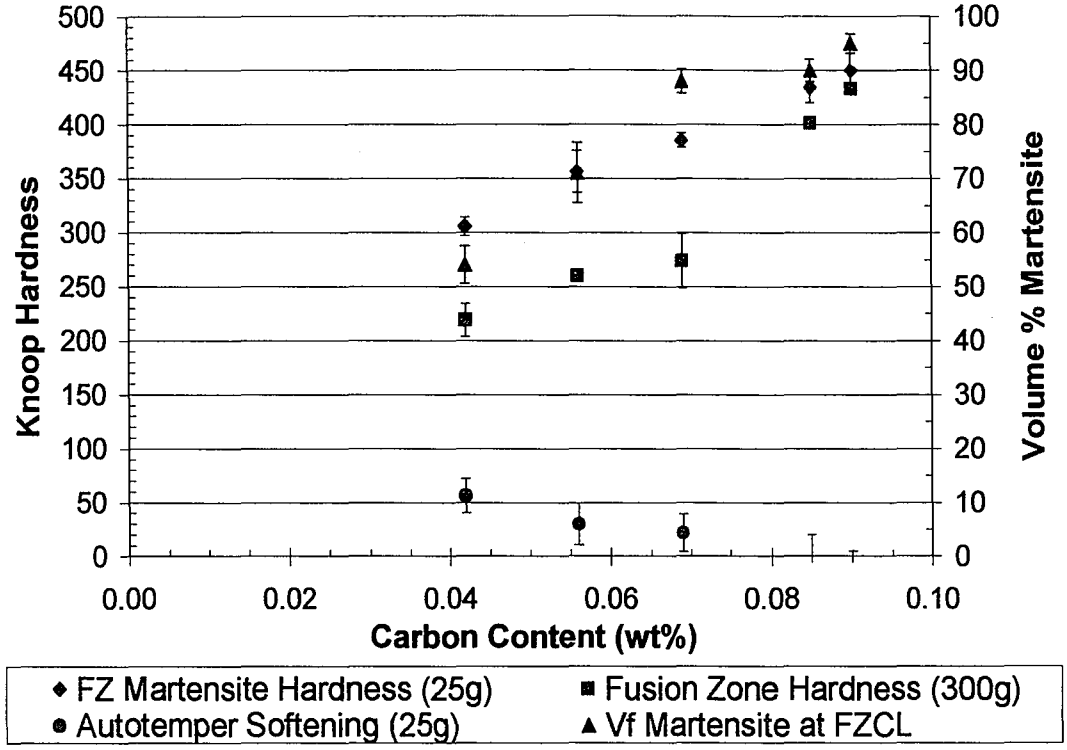

Figure 4-27. The effect of carbon content on FZCL hardness.

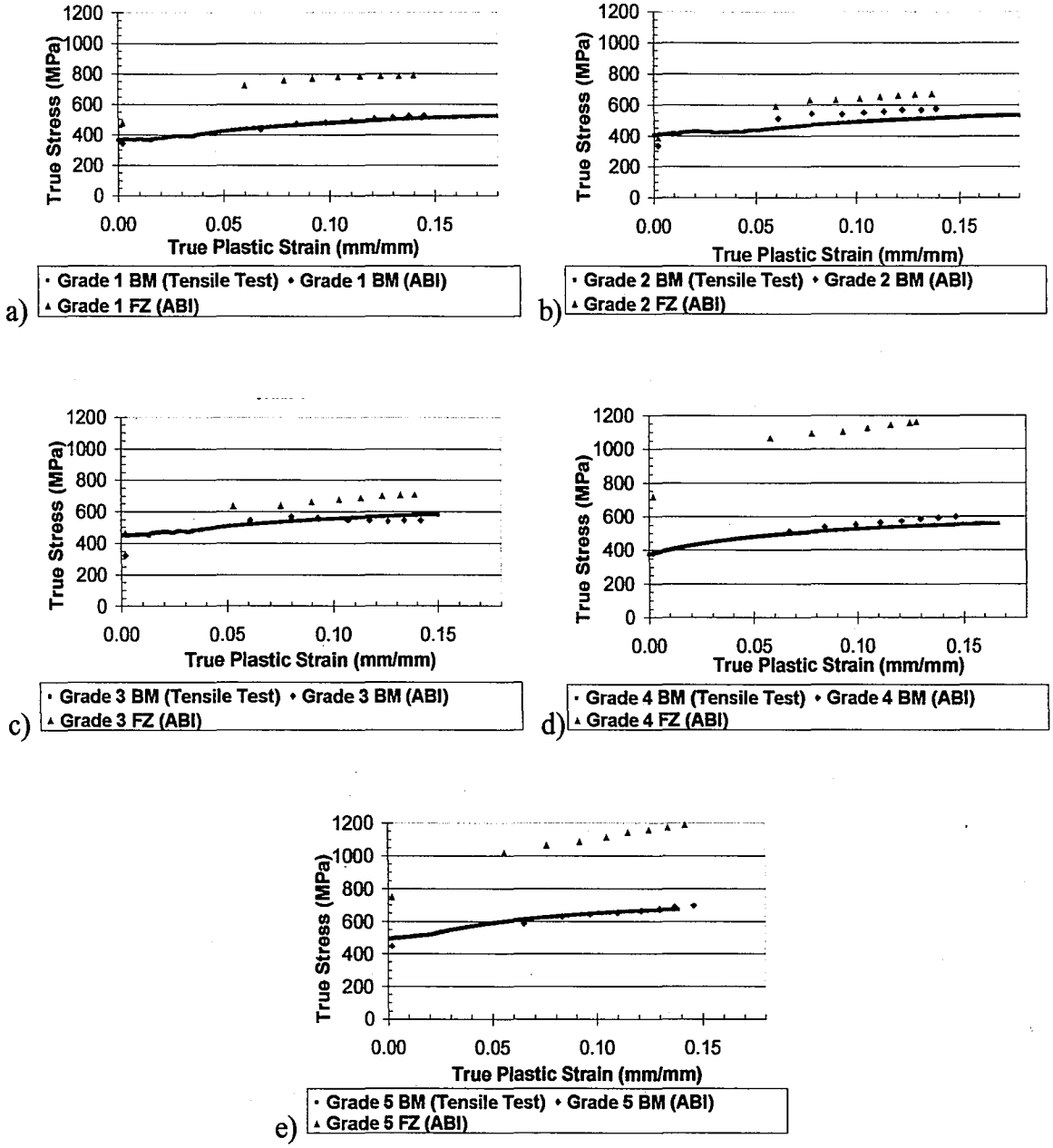

Figure 4-28. Comparison of ASTM tensile test data to base metal and FZCL ABI data for a) grade 1, b) grade 2, c) grade 3, d) grade 4, e) grade 5.

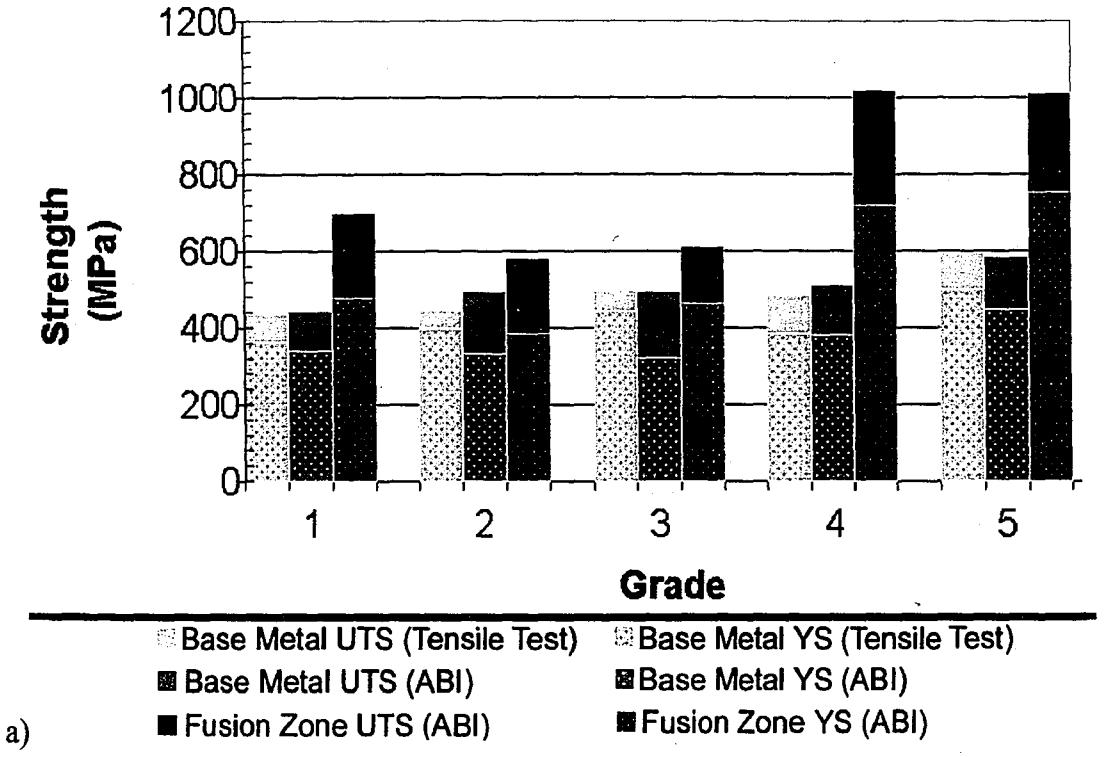

a)

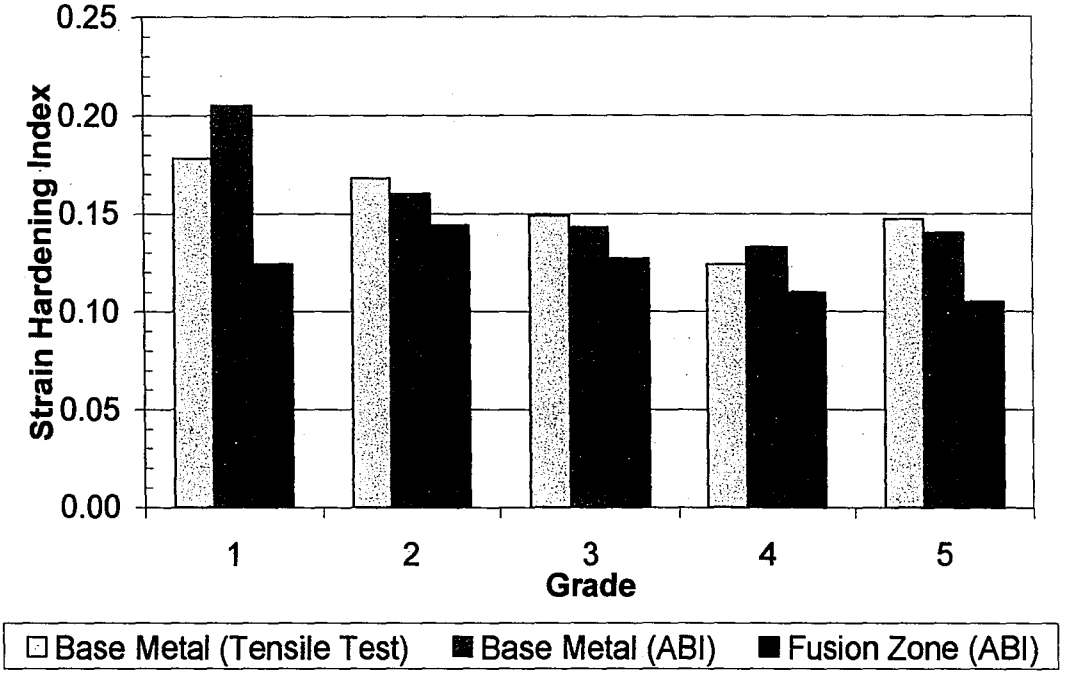

b)

Figure 4-29. Comparison of a) strength levels and b) strain hardening indexes, as determined by standardized tensile testing of the as-rolled plate, ABI testing in the base metal, and ABI testing in the fusion zone.

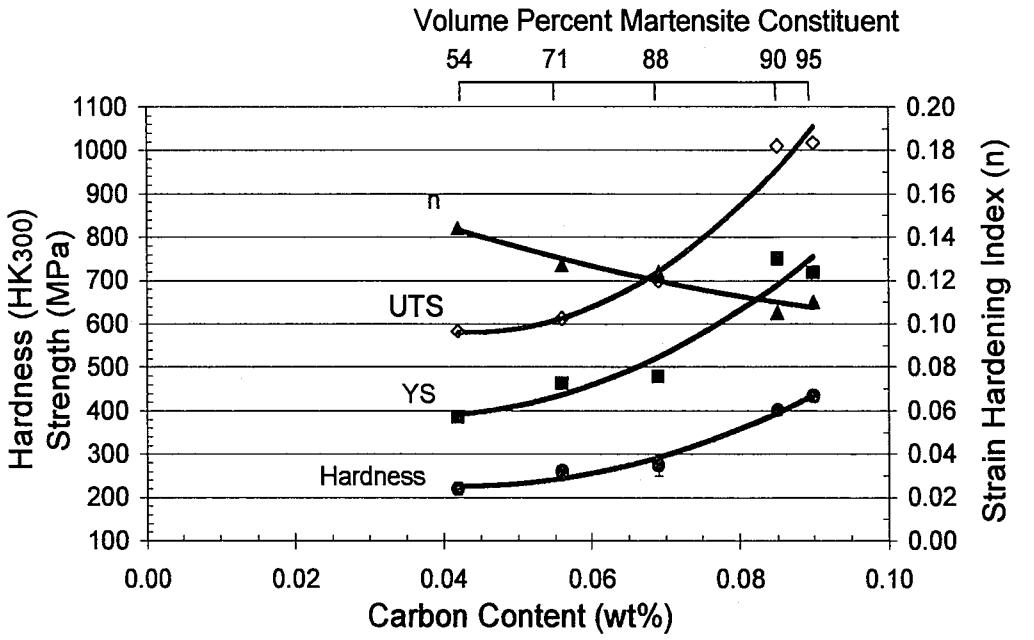

Figure 4-30. Summary of carbon content on fusion zone properties.

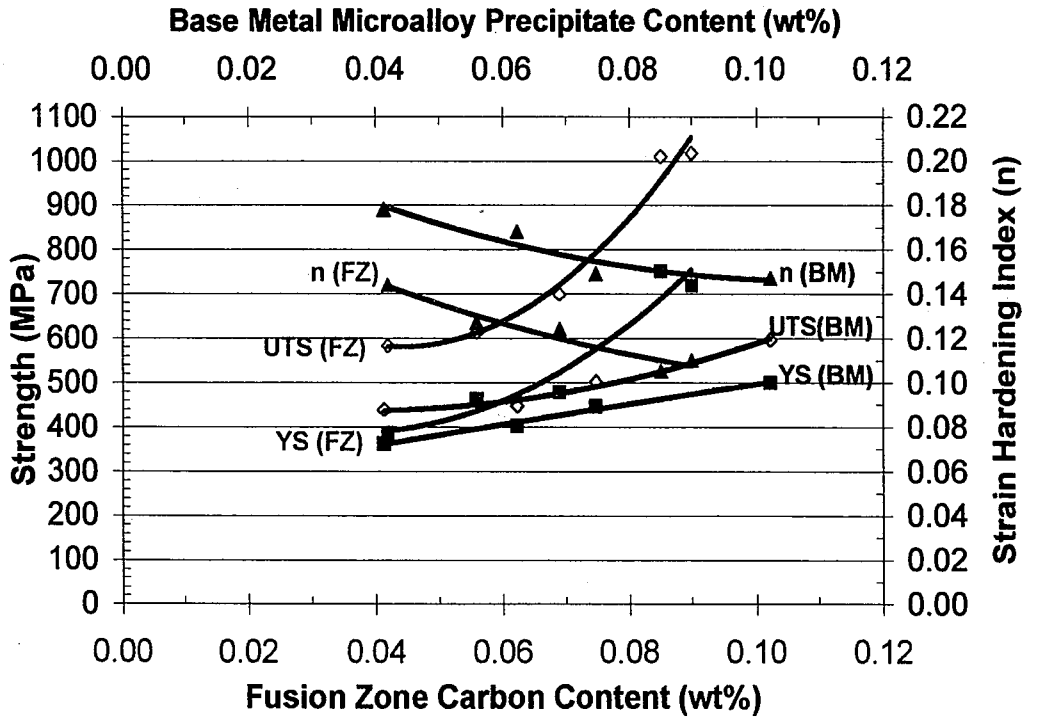

Figure 4-31. Summary of the effect of carbon content on fusion zone properties, and microalloy precipitate content on base metal properties.

5. Conclusions

The microstructures and mechanical properties of autogenous laser welds in five hot-rolled precipitation-strengthened steels have been characterized.

1. The mechanical properties of the base metal in ferrite-pearlite grades are most dependent upon microalloy precipitate content, which can be estimated using a basic thermodynamic technique. Increasing strength levels and decreasing strain hardening and ductility levels are associated with increases in microalloy content.
2. A simple two dimensional heat flow model was developed using SYSWELD. The model enabled the calculation of weld thermal cycles, which allowed for an understanding of the microstructural gradient that resulted from the laser welding process.
3. The hardness of the fusion zone and heat affected zone depends on the local microstructure. Hard regions are associated with martensitic and massive ferritic constituents, while ferrite-pearlite and ferrite-bainite microstructures are relatively soft. The peak hardness occurs near the fusion zone centerline, and the softest region is the base metal. Therefore the coarse grained heat affect zone was not of particular interest with regard to this study.
4. Martensitic microconstituents formed within all the fusion zones investigated, even in grades with carbon contents as low as 0.042 wt%.
5. Autotempering effects during laser welding and brine quenching were correlated with M_s temperature. Autotempering did not measurably affect the weld

mechanical properties in grades with calculated M_s temperatures below 450°C, but grades with M_s temperatures greater than 465°C exhibited significant autotempering.

6. The extent of martensite autotempering was insensitive to the range of cooling rates investigated in this study, i.e., brine quenched and fusion zone martensite of the same composition had the same microhardness.
7. Automatic ball indentation proved an effective method to determine weld mechanical properties. The fusion zones of all welds investigated were determined to be stronger and less ductile than the base metal.
8. Increases in fusion zone strength and decreases in fusion zone ductility were correlated with increasing carbon content. The high strain hardening values observed in dual phase (ferrite-martensite) steels were not achieved in the fusion zones in this study as a result of the high martensite content (greater than 50 vol%), which did not allow for the continuous ferrite matrix that is desirable in attaining high strain hardening values.
9. It is suggested that decreasing carbon content and increasing microalloy content may allow for high strength steels that are reasonably formable in the laser-welded state.

References Cited

1. F. I. Saunders and R. H. Wagoner, Forming of tailor-welded blanks. *Metall. Mater. Trans. A* **27A**, 2605-2616 (1996).

2. J. K. Baysore, M. S. Wiliamson, Y. Adonyi, and J. L. Miliam, Laser Beam Welding and Formability of Tailored Blanks. *Weld. J. (Miami)* **74**, 345-s-352-s (1995).

3. M. F. Shi, K. M. Pickett, and K. K. Bhatt, Formability Issues in the Application of Tailor Welded Blank Sheets. *SAE [Tech. Pap.]* **930278**, 345-353 (1993).

4. A. P. Lee, E. Feltham, and J. Van Deventer, Tailor welded blank technology for automotive applications. *Soc. Automot. Eng. , [Spec. Publ.] SP* **SP-1134**, 91-102 (1996).

5. H. Hayashi and T. Nakagawa, Recent trends in sheet metals and their formability in manufacturing automotive panels. *J Materials Processing Technology* **46**, 455-487 (1994).

6. H. Hayashi, Development of High Strength Steel Sheets and Practical Application to Autobody Parts. *SAE [Tech. Pap.]* **950699**, 560-570 (1995).

7. H. Hayashi. Development of New Types of High Strength Steel Sheets and their Application Trials to Autobodies in Japan. (1993).

8. US Steel, The Manufacture of Hot-Strip Mill Products. In *The Making, Shaping, and Treating of Steel*, 10 Edn, ed. by W. T. J. Lankford, N. L. Samways, R. F. Craven, and H. E. McGannon, pp 1069-1097. Herbick & Held, Pittsburgh, PA (1985).

9. I. V. Samarasekera, C. A. Muojekwu, D. Q. Jin, and J. K. Brimacombe, The state-of-the-art: hot rolling of thin slabs. *Mech. Work. Steel Process. Conf. Proc.* **35**, 861-873 (1998).

10. E. A. Donini, R. Borsi, and A. Carboni, Flexible Thin-Slab Rolling: Matching the Requirements of Integrate Producers. *Iron Steel Eng.* 39-44 (1997).

11. E. O. Hall, The deformation and aging of mild steel. III. Discussion of results. *Proc. Phys. Soc. B* **64**, 747-753 (1951).

12. N. J. Petch, Grain size relationships. *J Iron Steel Inst* **174**, 25-28 (1953).

13. J. D. Eshelby, F. C. Frank, and F. R. N. Nabarro, Hall-Petch relationships. *Philos. Mag.* **42**, (1951).

14. J. C. M. Li, *Trans Met Soc AIME* **227**, (1963).

15. N. J. Petch, Ductile-cleavage transition in .alpha.-iron. *Fracture, Proc. Intern. Conf. at. Mechanisms Fracture, Swampscott, Mass. (B. L. Averbach, D. K. Felbeck, G. T. Jahn, and D. A. Thomas, editors. Technology Press of Mass. Inst. of Technol. and John Wiley & Sons, Inc.)* 54-67 (1959).

16. B. Mintz, Importance of ky (Hall-Petch slope) in determining strength of steels. *Met. Technol. (London)* **11**, 265-272 (1984).

17. B. Mintz and J. Kolahi-Aval. Influence of cooling rate from the normalizing temperature on the Hall-Petch slopes for steels. 1. 1986. Strength Met. Alloys, Proc. Int. Conf., 7th.

18. B. Mintz, H. Ke, and G. D. W. Smith, Grain size strengthening in steel and its relationship to grain boundary segregation of carbon. *Mater. Sci. Technol.* **8**, 537-540 (1992).

19. D. V. Wilson, Grain-size dependence of discontinuous yielding in strain-aged steels. *Acta Met.* **16**, 743-753 (1968).

20. R. Kuziak, T. Bold, and Y.-W. Cheng, Microstructure Control of Ferrite-Pearlite High Strength Low Alloy Steels Utilizing Microalloying Additions. *J Materials Processing Technology* **53**, 255-262 (1995).

21. H. Imanari, M. Tsugeno, M. Hioka, S. W. Markward, and J. Lewis, New process control system in hot strip mill of North Star BHP steel. *Iron Steel Eng.* **76**, 32-37 (1999).

22. J. Majta, J. G. Lenard, and M. Pietrzyk, A study of the effect of the thermomechanical history on the mechanical properties of a high niobium steel. *Mat Sci Engr A* **208**, 249-259 (1996).

23. A. Kirihata, F. Siciliano, Jr., T. M. Maccagno, and J. J. Jonas, Mathematical modeling of mean flow stress during the hot strip rolling of multiply-alloyed medium carbon steels. *ISIJ Int.* **38**, 187-195 (1998).

24. P. D. Hodgson and R. K. Gibbs, Hodgson, P.D. and Gibbs, R.K.: Iron Steel Inst. Jpn. Int., 1992, vol. 32, pp. 1329-1338. *ISIJ Int.* **32**, 1329-1338 (1992).

25. P. D. Hodgson, D. L. Hazeldon, D. L. Matthews, and R. E. Gloss. P.D. Hodgson, L.O. Hazeldon, D.L. Matthews, and R.E. Gloss: in *Microalloying '95*, M. Korchynsky, A.J. DeArdo, P. Repas and G. Tither, ISS-AIME, Warrendale, PA 1996, pp. 585-590. 1996.

26. N. Maruyama, R. Uemori, and M. Sugiyama, The role of niobium in the retardation of the early stage of austenite recovery in hot-deformed steels. *Mater. Sci. Eng. , A* **250**, 2-7 (1998).

27. T. Tanaka, N. Tabata, T. Hatomura, and C. Shiga. T. Tanaka, N. Tabata, T. Hatomura ancd C. Shiga: in *Microalloying '75*, Proc. Int. Conf. on HSLA Steels, Union Carbide Corp., New York, 1977, p.107. 1977.

28. J. Majta, Complete model for niobium-microalloyed steels deformed under hot working conditions. *Rozpr. Monogr.* **89**, 1-122 (2000).

29. R. Colas. Computer simulation of hot rolling of steel. 1996. Hot Workability Steels Light Alloys-Compos., Proc. Int. Symp.

30. F. Siciliano, Jr. and J. J. Jonas, Mathematical modeling of the hot strip rolling of microalloyed Nb, multiply-alloyed Cr-Mo, and plain C-Mn steels. *Metall. Mater. Trans. A* **31A**, 511-530 (2000).

31. J. J. Jonas, The hot strip mill as an experimental tool. *ISIJ Int.* **40**, 731-738 (2000).

32. R. W. Hertzberg, Strengthening Mechanisms in Metals. In *Deformation and Fracture Mechanics in Engineering Materials*, 4 Edn,pp 123-156. John Wiley & Sons, Inc., New York (1996).

33. E. Orowan. Discussions in *Symposium on Internal Stresses in Metals and Alloys*, Institute of Metals, London, 451 (1948). 1948.

34. M. F. Ashby, Oxide Dispersion Strengthening. *Metallurgical Soc AIME* **143**, (1958).

35. J. Irvine and T. N. Baker, The influence of rolling variables on the strengthening mechanisms operating in niobium steels. *Mater. Sci. Eng.* **64**, 123-134 (1984).

36. D. T. Gawne and G. M. H. Lewis, Strengthening mechanisms in high-strength microalloyed steels. *Mater. Sci. Technol.* **1**, 183-191 (1985).

37. T. Gladman, *The Physical Metallurgy of Microalloyed Steels*, The University Press, Cambridge (1997).

38. N. Tsuchida and Y. Tomota, A micromechanic modeling for transformation induced plasticity in steels. *Mater. Sci. Eng. , A* **A285**, 345-352 (2000).

39. R. G. Davies, Influence of martensite composition and content on the properties of dual phase steels. *Metall. Trans. , A* **9A**, 671-679 (1978).

40. R. G. Davies, The mechanical properties of zero-carbon ferrite-plus-martensite structures. *Metall. Trans. , A* **9A**, 451-455 (1978).

41. S. Sangal, N. C. Goel, and K. Tangri, A theoretical model for the flow behavior of commercial dual-phase steels containing metastable retained austenite: part II. Calculation of flow curves. *Metall. Trans. A* **16A**, 2023-2029 (1985).

42. N. C. Goel, S. Sangal, and K. Tangri, A theoretical model for the flow behavior of commercial dual-phase steels containing metastable retained austenite: part I. Derivation of flow curve equations. *Metall. Trans. A* **16A**, 2013-2021 (1985).

43. J. Lian, Z. Jiang, and J. Liu, Theoretical model for the tensile work hardening behavior of dual-phase steel. *Mater. Sci. Eng. , A* **A147**, 55-65 (1991).

44. L. A. Norstrom, On the yield strength of quenched low-carbon lath martensite. *Scand. J. Metall.* **5**, 159-165 (1976).

45. Z. Jiang, J. Liu, and J. Lian, A new relationship between the flow stress and the microstructural parameters for dual-phase steel. *Acta Metall. Mater.* **40**, 1587-1597 (1992).

46. A. R. Marder. The structure-property relationships in chromium-bearing dual-phase steels. 1981. Fundam. Dual-Phase Steels, Proc. Symp.

47. N. K. Ballinger and T. Gladman, Work hardening of dual-phase steels. *Met Sci* **15**, 95-108 (1981).

48. C. A. N. Lanzillotto and F. B. Pickering, Structure-property relations in dual-phase steels. *Met Sci* **16**, 371-382 (1982).

49. D. A. Burford, D. K. Matlock, and G. Krauss, In *Strength of Metals and Alloys*, 1 Edn, ed. by H. J. McQueen, J. P. Bailon, J. I. Dickson, J. J. Jonas, and M. G. Akben, pp 189. Oxford (1985).

50. Z. Jiang, Z. Guan, and J. Lian, Effects of microstructural variables on the deformation behavior of dual-phase steel. *Mater. Sci. Eng. A* **A190**, 55-64 (1995).

51. P. H. Chang and A. G. Preban, The effect of ferrite grain size and martensite volume fraction on the tensile properties of dual-phase steel. *Acta Metall.* **33**, 897-903 (1985).

52. A. Bayram, A. Uguz, and M. Ula, Effects of Microstructure and Notches on the Mechanical Properties of Dual-Phase Steels. *Materials Characterization* **43**, 259-269 (1999).

53. J. H. Suh, T. H. Kim, B. K. Yu, and K. D. Lee, A study of tailored blank welding between mild steel sheet and Zn-coated steel sheet by CO2 laser beam. *Met. Mater. (Seoul)* **4**, 157-163 (1998).

54. B. G. Chung, S. Rhee, and C. H. Lee, The effect of shielding gas types on CO2 laser tailored blank weldability of low carbon automotive galvanized steel. *Mater. Sci. Eng. , A* **A272**, 357-362 (1999).

55. B. Bouaifi, Influence of joining techniques on the microstructure and formability of steel sheet. *Welding and Cutting* 37-40 (1994).

56. Rosenthal, D.: *Weld. J.*, **20:** 220s,(1941).

57. DSI. Simulation of Laser Wleding HAZ using Gleeble Systems. APN009, 1-7. 1997. Dynamic Systems Inc.

58. P. H. Steen, P. Ehrhard, and A. Schussler, Depth of Melt-Pool and Heat-Affected Zone in Laser Surface Treatments. *Metall. Mater. Trans. A* **25A**, 427-435 (1994).

59. S. Zajac, R. Lagneborg, and T. Siwecki. The role of nitrogen in microalloyed steels. 321-338. 1995. Microalloying '95 Conference Proceedings. 1995.

60. US Steel, Manufacture of Cold-Reduced Flat-Rolled Products. In *The Making, Shaping, and Treating of Steel*, 10 Edn, ed. by W. T. J. Lankford, N. L. Samways, R. F. Craven, and H. E. McGannon, pp 1099-1120. Herbick & Held, Pittsburgh, PA (1985).

61. C. Garcia-Mateo, B. Lopez, and J. M. Rodriguez-Ibabe, Influence of Vanadium on Static Recrystallization in Warm Worked Microalloyed Steels. *Scripta mater.* **42**, 137-143 (2000).

62. R. Lagneborg, T. Siwecki, S. Zajac, and B. Hutchinson, The role of vanadium in microalloyed steels. *Scand. J. Metall.* **28**, 186-241 (1999).

63. ASTM, *1996 Annual Book of ASTM Standards*, (1996).

64. J. H. Park and T. H. Kim, Tailored blank welding between low carbon steel sheet and STS 304 stainless steel sheet by CO2 laser beam. *Met. Mater. (Seoul)* **5**, 55-62 (1999).

65. M. Eisenmenger, K. K. Bhatt, and M. F. Shi, Influence of laser welding parameters on formability and robustness of blank manufacturing: an application to a body side frame. *Soc. Automot. Eng. , [Spec. Publ.] SP* **SP-1067**, 171-182 (1995).

66. F. M. Haggag. U.S. Patent. [4852397]. 1989.

67. F. M. Haggag, H. Wong, D. J. Alexander, and R. K. Nanstead. The Use of Field Indentation Microprobe in Measuring Mechanical Properties of Welds. *Recent Trends in Welding Science and Technology,* ASM International, 1990.

68. F. M. Haggag, In-situ measurements of mechanical properties using novel automated ball indentation system. *ASTM Spec. Tech. Publ.* **STP 1204**, 27-44 (1993).

69. F. M. Haggag, J. A. Wang, M. A. Sokolov, and K. L. Murty, Use of portable/in situ stress-strain microprobe system to measure stress-strain behavior and damage in metallic materials and structures. *ASTM Spec. Tech. Publ.* **STP 1318**, 85-98 (1997).

70. D. Tabor, *Hardness of Solids*, Oxford University Press, Oxford, (1951).

71. A. I. Nadai, *Theory of Flow and Fracture of Solids,* **2** McGraw-Hill, New York, (1963)

72. Y. Bora. Nonlinear thermal stress/fracture analysis of multilayer structures using enriched finite elements. 2000. Lehigh University.

73. P. W. Fuerschbach, Measurement and prediction of energy transfer efficiency in laser beam welding. *Weld. J. (Miami)* **75**, 24s-34s (1996).

74. S. M. Roberts, H. J. Stone, J. M. Robinson, P. J. Withers, R. C. Reed, D. R. Crooke, B. J. Glassey, and D. J. Horwood, Characterisation and modelling of the electron beam welding of waspaloy. In *Mathematical Modelling of Weld Phenomena 4* ed. by H. Cerjack, pp 631-648. IOM Communications Ltd, Cambridge (1998).

75. S. Murugan, P. V. Kumar, T. P. S. Gill, B. Raj, and M. S. C. Bose, Numerical modelling and experimental determination of temperature distribution during manual metal arc welding. *Sci. Technol. Weld. Joining* **4**, 357-364 (1999).

76. J. H. Argyris, J. Szimmat, and K. J. Willam, Computational aspects of welding stress analysis. In *Computational Methods in Applied Mechanics and Engineering* pp 635-666. (1982).

77. J. Goldak, A. Chakravarti, and M. Bibby, A new finite element model for welding heat sources. *Metall. Trans. B* **15B**, 299-305 (1984).

78. Irvine K J, F. B. Pickering, and T. Gladman, K.J. Irvine, F.B. Pickering, and T. Gladman: *J. Iron adn Steel Inst.,* 1967, **205**, p 161. *J Iron Steel Inst* (1967).

79. K. A. Taylor: *Scripta Met. et Mat.*, 1995, **32**, p.7. *Scripta Metallurgica et Materialia* 7 (1995).

80. K. Narita, Physical chemistry of the Groups IVB (titanium, zirconium), VB (vanadium, niobium, tantalum) and the rare earth elements in steel. *ISIJ Int.* **15**, 145-152 (1975).

81. H. Sekine, T. Inoue, and M. Ogasawara: *Trans. Iron Steel Inst. Japan,* 1968, **8**, p. 101. *Trans. Iron Steel Inst. Jpn.* (1968).

82. K. Bungardt, K. Kind and W. Oelsen: *Archiv. f.d. Eisenbuttenwes.* 1956, **27**, p. 6. *Arch. Eisenhuettenwes.* (1956).

83. R. C. Cochrane. IIW Doc. IXJ-102-85. *Weld.World* . 1985.

84. Commision IX of the IIW. Guide to the light microscope examination of ferritic steel weld metals. *Welding in the World* 29[7/8], 160-177. 1991.

85. O. Grong, *Metallurgical Modelling of Welding*, Institute of Materials, London (1997).

86. O. M. Akselsen, G. Roervik, M. I. Onsoeien, and O. Grong, Assessment and predictions of HAZ tensile properties of high-strength steels. *Weld. Res. (Miami)* 356s-362s (1989).

87. J. M. B. Losz, S. Saboury, and T. M. McNutt, Microstructural characterization of submerged-arc and gas-metal-arc weldments in HY-130 steel. *ISIJ Int.* **35**, 71-78 (1995).

88. J. R. Yang and S. H. Liou, Microstructural evolution of simulated heat affected zone in ASTM A533 type B steel plates. *Science and Technology of Welding and Joining* **2**, 119-127 (1997).

89. P. M. Kelly and J. Nutting, The martensite transformation in carbon steel. *Proc. Roy. Soc. (London)* **A259**, 45-58 (1960).

90. G. R. Speich and H. Warlimont, Yield strength and transformation substructure of low-carbon martensite. *JISI* **206**, 385-392 (1968).

91. R. H. Aborn, Low Carbon Martensites. *Trans. ASM* **48**, 51-85 (1956).

92. M. J. Bibby and J. G. Parr, The martensitic transformation in pure iron. *J Iron Steel Inst* **202**, 100-104 (1964).

93. G. R. Speich and P. R. Swann, *JISI* **203**, 480 (1965).

94. S. Suzuki, G. C. Weatherly, and D. C. Houghton, The response of carbonitride particles in HSLA steels to weld thermal cycles. *Acta Metall.* **35**, 341-352 (1987).

95. G. R. Wang, T. W. Lau, G. C. Weatherly, and T. H. North, Weld thermal cycles and precipitation effects in titanium-vanadium HSLA steels. *Metall. Trans. A* **20A**, 2093-2100 (1989).

96. S. Liu and F.-C. Liao, Precipitate stability in the heat affected zone of nitrogen-enhanced high strength low alloy steels. *Mater. Sci. Eng. A* **A244**, 273-283 (1998).

97. J. H. Hollomon, *Trans. AIME* **162**, 268 (1945).

98. K. Abdullah, P. M. Wild, J. J. Jeswiet, and A. Ghasempoor, Tensile testing for weld deformation properties in similar gage tailor welded blanks using the rule of mixtures. *J. Mater. Process. Technol* **112**, 91-97 (2001).

99. D. Dry, W. Waddell, and D. R. J. Owen, Determination of laser weld properties for finite element analysis of laser welded tailored blanks. *Science and Technology of Welding and Joining* **7**, 11-18 (2002).

100. B. Y. Ghoo, Y. T. Keum, and Y. S. Kim, Evaluation of the mechanical properties of welded metal in tailored steel sheet welded by CO2 laser. *J. Mater. Process. Technol* **113**, 692-698 (2001).

101. P. Payson and C. H. Savage, *Trans. ASM* **33**, 261-275 (1944).

102. L. A. Carapella, *Metal Progress* **46**, 108 (1944).

103. E. S. Rowland and S. R. Lyle, *Trans. ASM* **37**, 27-47 (1946).

104. R. A. Grange and H. M. Stewart, *Trans Met Soc AIME* **167**, 467-490 (1946).

105. A. E. Nehrenberg, T*rans AIME* **167**, 494-498 (1946).

106. W. Steven and A. G. Haynes, The temperature of formation of martensite and bainite in low-alloy steels. Some effects of chemical composition. *JISI* **183**, 349-359 (1956).

107. K. W. Andrews, Empirical formulas for the calculation of some transformation temperatures. *JISI* **203**, 721-727 (1965).

Appendix I: Calculation of M_s and M_f Temperatures

The M_s and M_f temperatures calculated in Table 4-4 were calculated based on empirical composition-related equations available in the literature. The work cited was performed in low alloy ferritic steels, and therefore are expected to be of direct relevance to the materials investigated in this study. Note that, because of the dependence of M_s and M_f on prior austenite microstructure and cooling rate, some deviation in calculated temperatures is expected within each grade.

All compositions in these relationships are expressed in wt%. The martensite temperatures are given either in (°C) or (°F) as listed.

Payson and Savage: $M_s(°F)=930-570C-60Mn-50Cr-30Ni-20Si-20Mo-20W$

Carapella: $M_s(°F)=925(1-0.620C)(1-0.092Mn)(1-0.033Si)(1-0.045Ni)\ (1-0.070Cr)(1-0.029Mo)(1-0.018W)(1+0.120Co)$

Rowland and Lyle: $M_s(°F)=930-600C-60Mn-50Cr-30Ni-20Si-20Mo-20W$

Grange and Stewart: $M_s(°F)=1000-650C-70Mn-70Cr-35Ni-50Mo$

Nehrenberg: $M_s(°F)=930-540C-60Mn-40Cr-30Ni-20Si-20Mo$

Steven and Hayes: $M_s(°C)=561-474C-33Mn-17Cr-17Ni-21Mo$

$M_f(°C)= 346-474C-33Mn-17Cr-17Ni-21Mo$

Andrews Linear: $M_s(°C)=539-423C-30.4Mn-12.1Cr-17.7Ni-7.5Mo$

Andrews Product: $M_s(°C)=512-453C-16.9Ni+15Cr-9.5Mo+217(C)^2-71.5(C)(Mn)-7.6(C)(Cr)$

Vita

Goodwin Phillip Anderson was born on June 28, 1978 in Bryn Mawr, Pennsylvania, to Robert and Kathy Anderson. He was raised in suburban Philadelphia with his older brother, Andrew, and his younger brother, James. He developed many interests as he grew, remaining active in athletics (football, swimming, and track and field), music (clarinet, tenor saxophone, and chorus), and student government during his high school years. In 1996, he graduated from Radnor High School and continued his education at Lehigh University, where he studied Materials Science, played varsity football, and was active in the Chi Psi Fraternity and Fellowship of Christian Athletes. He was awarded the Col. Earl H. Blaik Graduate Fellowship based on his achievement as a student athlete and graduated with honors from Lehigh with his Bachelors degree in the spring of 2000. In the summer of 2000, he began work on a Masters program in Materials Science and Engineering at Lehigh University while being funded in part by the New Jersey Zinc Fellowship. While a graduate student, he was recognized as a U.S. Steel Fellow and as a visiting researcher at the National Institute of Standards and Technology (NIST).

END OF TITLE